UNIVERSITY OF CALIFORNIA

SANTA BARBARA

Spectroscopic Analysis of Semiconductor Quantum Dot Surfaces

A dissertation submitted in partial satisfaction of

the requirements for the degree of

Doctor of Philosophy in Chemistry

by

Robert William Meulenberg

Committee in charge:

Professor Horia Metiu

Professor Bernard Kirtman

Professor Steven K. Buratto

Professor Geoffrey F. Strouse, Chair

December 2002

The dissertation of Robert W. Meulenberg is approved.

Horia Metiu

Bernard Kirtman

Steven K. Buratto

Geoffrey F. Strouse, Committee Chair

December 2002

Spectroscopic Analysis of Semiconductor Quantum Dot Surfaces

By

Robert William Meulenberg

ACKNOWLEDMENTS

I would like to thank Professor Geoffrey Strouse for his guidance and support during my tenure at UCSB. I would also like to thank his group for general support. Specifically, I would like to thank Steve Yun for being a good ear as well as a good sample preparer. Also, Artjay Javier for countless discussions and being a good office partner. Finally, Khalid Hanif, for being a good friend and colleague throughout my time here.

I would also like to thank my committee for their time. Specifically, thanks to Professor Bernie Kirtman for many hours of intriguing discussions. I would like to give a special thanks to Professor Henry Offen, who has been an excellent mentor these last few years.

I would like to thank my family, specifically my parents, sister, niece, and dogs for their love and support my whole life. Finally, thanks to my wife, Christa, who has been my love and support through all of this.

VITA OF ROBERT W. MEULENBERG

December 2002

BORN

December 7, 1976 – Abington, Pennsylvania

EDUCATION

Ph.D., Physical Chemistry, University of California, Santa Barbara, December 2002

B.S., Chemistry, Florida State University, May 1998

PROFESSIONAL EXPERIENCE

1999-2002: Research Assistant, University of California, Santa Barbara
2001-2002: Guest Researcher, Lawrence Livermore National Laboratory
1998-2000: Teaching Assistant, University of California, Santa Barbara
1997: Teaching Assistant, Florida State University

PUBLICATIONS

"Chain Packing Analysis of the Passivating Layer on Nanocrystalline Quantum Dot Surfaces." R.W. Meulenberg, G.F. Strouse, *J. Phys. Chem. B* **105**, 7438-7445 (2001).

"Low Pressure Band Tuning in Wurtzite CdSe Quantum Dots." R.W. Meulenberg, H.W. Offen, G.F. Strouse, *Mat. Res. Soc. Symp. Proc.,* **636**, D9.46, 1-7 (2001).

"Pressure Induced Electronic Coupling in CdSe Semiconductor Quantum Dots." R.W. Meulenberg, G.F. Strouse, *Phys. Rev. B* **66**, 035317 (2002).

“Effects of Alkylamine Chain Length on the Thermal Behavior of CdSe Quantum Dot Glassy Films.” R.W. Meulenberg, S. Bryan, C.S. Yun, G.F. Strouse, *J. Phys. Chem. B* **106**, 7774 (2002).

“Magnetic Ordering in Doped $Cd_{1-x}Co_xSe$ Diluted Magnetic Quantum Dots." K.M. Hanif, R.W. Meulenberg, G.F. Strouse, *J. Amer. Chem. Soc.*, **124**, 11495 (2002).

“Optical Absorption and Electrospray Ionization Analyses of Mixed Valent Cobalt Doped Cadmium Chalcogenide Molecular Clusters.” R.W. Meulenberg, K.M. Hanif, J.J. Gaumet, G.F. Strouse, in prep.

“Assemblies of Quantum Dots via Oligomeric Wires.” C.S. Yun, A. Javier, G.A. Khitrov, R.W. Meulenberg, G.F. Strouse, in prep.

“Size Dependent Lattice Ionicity in II-VI Semiconductor Quantum Dots.” R.W. Meulenberg, G.F. Strouse, in prep.

“Compressive and Tensile Stress in Colloidal CdSe Semiconductor Quantum Dots.” R.W. Meulenberg, T. Jennings, G.F. Strouse, in prep.

AWARDS

2001 Material Research Society Graduate Student Silver Award

FIELDS OF STUDY

Major interests: Condensed matter and materials physics

ABSTRACT

Spectroscopic Analysis of Semiconductor Quantum Dots Surfaces

by

Robert W. Meulenberg

An important field of research recently in nanoscience is to examine the effect of an impurity atom on the physics of quantum dots (QDs). An intriguing question to ask is how an unintentional dopant, such as a surface atom, can affect the optical and vibrational properties of the QD. In this dissertation these effects are analyzed by using resonance Raman and photoluminescence spectroscopies. The data indicates that changes in the nature of electron-phonon (el-ph) coupling in the strongly confined regime leads to changes in lattice ionicity for CdSe QDs. The changes in lattice ionicity is strictly evident in the vibrational properties of the QDs, as slight changes in the chemical preparation of the dots can induce various levels of surface strain on the QDs. More proof indicating that chemical preparation can alter the physics of these materials is evident in the positron annihilation data obtained in collaboration with Lawrence Livermore National Laboratory. The trends in the data suggest the positron localization is changed as the colloidal preparation is changed. Correlation of these experiments indicates that the surface chemistry and physics of QDs are very complex and cannot be ignored.

TABLE OF CONTENTS

Chapter 1: Dimensional Effects in Nanocrystal Quantum Dots

PART I: Analysis of the Thermal Behavior of Alkylamines on Semiconductor Quantum Dot Surfaces Using Attenuated Total Reflection Infrared Spectroscopy

Chapter 2: Thermodynamics and Packing Analysis of *n*-Hexadecylamine on CdSe Quantum Dot Surfaces

Chapter 3: Effects of Alkylamine Chain Length on the Thermal Behavior of CdSe Quantum Dots Glassy Films

PART II: Effect of Defects on the Optical and Vibrational Properties of Semiconductor Quantum Dots

Chapter 4: Polaronic Defects and Electron-Phonon Coupling in CdSe Quantum Dots under Hydrostatic Pressure

Chapter 5: Compressive and Tensile Stress in Colloidal CdSe Semiconductor Quantum Dots

PART III: Applications of Positron Spectroscopy to Analyze the Defect and Confinement Properties of Metal and Semiconductor Nanocrystals

Chapter 6: Electron Momentum Distributions in Nanocrystal Quantum Dots Using Positrons

List of Figures

Chapter 1: Dimensional Effects in Nanocrystal Quantum Dots

1.1. Introduction

The study of nanometer sized semiconductor crystallites (NCs), also known as quantum dots (QDs), has seen rapid advancements in recent years in scientific disciplines ranging from chemistry, physics, materials science, and engineering. [1] QD materials of CdSe, ZnSe, InP, Fe_2O_3, as well as many others, can be prepared in the size range of 10 –100 Å by lyothermal methods producing uniform, nearly monodisperse materials (~5% rms) that are typically coated with organic molecules. [2-5] The strength of confinement of the charge carriers, which dictates the size-dependent properties, in these QDs depends on the nature of the material and can be correlated to the Bohr radius for the system of interest. For instance, in CdSe the Bohr radius is ~50 Å, while in the more covalent structure of InP, the Bohr radius approaches >100 Å. The differences in the Bohr radii arise primarily from changes in the exciton binding energy (14.8 meV to 4.4 meV for CdSe and InP, respectively) that are directly connected to the changes in lattice ionicity (dielectric constant). Changes in lattice ionicity can modulate the surface state energies, character, and magnitude of perturbation of the core electronic levels in nanoscale materials through electron-phonon (el-ph) interactions.

From a chemical perspective, finding the delicate balances between thermodynamics and kinetics in the lyothermal growths of colloidal QDs has been advantageous in producing QDs with well-defined shapes, stoichiometries, and size dispersities. [6, 7] From a physics perceptive, size-dependent scaling laws have been realized in many of the physical properties including the optical band gaps, melting points, pressure induced phase transitions, excitonic exchange interaction, and optical and vibrational pressure coefficients which arise primarily from quantum size effects (QSE). [2, 8-11] These scaling laws are the fundamental laws that govern QD physics and can aid researchers in the fabrication of QD assemblies for potential uses in nano-optoelectronic materials.

The fact that QSE strongly modulate the properties of QDs is a direct result of the reduced dimensionality of the QD. In the most simplistic model, nanomaterials may be thought of fragments of a bulk lattice with spatial directions noted as L_x, L_y, and L_z (Figure 1.1). [12] When a bulk lattice becomes confined in one dimension (i.e. $L_x \sim L_y >> L_z$), a quantum well is formed which experiences electron confinement in only 1-dimension. When a bulk lattice becomes confined in two dimensions (i.e. $L_x >> L_y, L_z$), the y and z degrees of freedom are constrained, therefore allowing electronic degrees of freedom in the x-direction only. This 2-d confinement is typically known as a quantum wire. This takes us to the realm of 3-dimensional confinement, commonly called a "quasi-0d" quantum dot because the electronic degrees of freedom are frozen in all three dimensions. QSE lead to the quantization of the bulk band

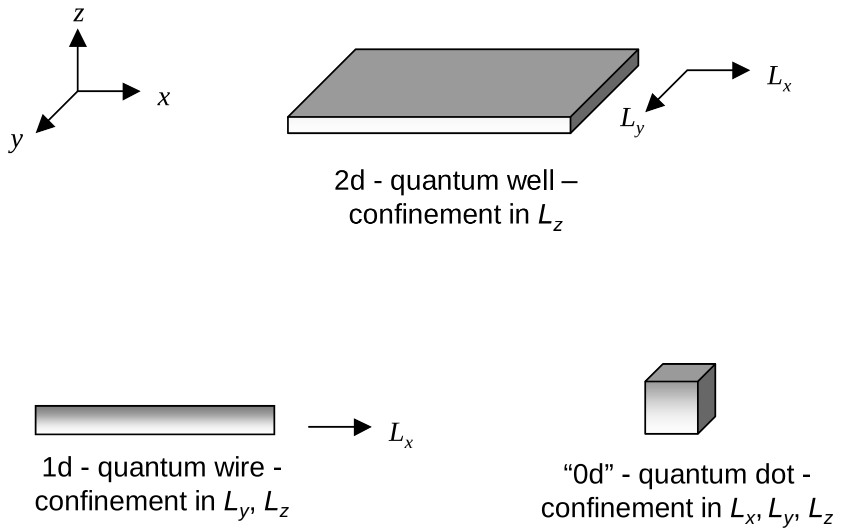

Figure 1.1. Schematic illustrations of 2d, 1d, and 0d confinement.

structure, enhanced particle-particle interactions (i.e. electron-electron, electron-phonon, exciton-exciton), and a blue shift of the optical band gap. The observed blue shift can be explained in terms of a particle-in-a-box model where the energy level spacing goes as $\Delta E \sim L^{-2}$. Brus [13] extended this model to incorporate Coulombic and dielectric surface effects,

$$E_g^{QD} = E_g^{bulk} + \frac{\hbar^2 \pi^2}{2R^2}\left[\frac{1}{m_e} + \frac{1}{m_h}\right] - \frac{1.8e^2}{\varepsilon_2 R} + \frac{e^2}{R}\overline{\sum_{n=1}^{\infty} \alpha_n \left(\frac{S}{R}\right)^{2n}} \qquad (1\text{-}1)$$

where e is the fundamental unit of charge, m_e (m_h) is the effective mass of the electron (hole), ε_1 (ε_2) is the dielectric constant of the surrounding matrix (particle), S is a point that defines the degree of dielectric stabilization of the particle, R is the particle radius, E_g^{bulk} is the bulk band gap, $\alpha_n = \frac{(\varepsilon - 1)(n+1)}{\varepsilon_2(\varepsilon n + n + 1)}$, and $\varepsilon = \frac{\varepsilon_2}{\varepsilon_1}$. Because the quantum particle is modeled as a sphere rather than a box, the energy spacing goes as R^{-2} as opposed to L^{-2}. Qualitatively, the second term in eq. 1-1 represents the quantum kinetic energy of localization of the electron and hole. This is a direct function of the electron and hole masses, and is highly dependent on the relative ionicity of the material. The third term is the Coulombic attraction between the negatively charged electron and the positively charged hole which goes as R^{-1} from simple electrostatic theory. The third term in eq. 1-1 is a polarization term that arises from a charged species in the QD and its interactions with a surrounding dielectric, ε_1. This term can be thought of as the solvent reorganization energy, and has been shown to be extremely sensitive to solvent polarity. For instance, a simple calculation shows that as $\varepsilon_1 \to 0$ (i.e. a vacuum), $\alpha_n \to \frac{n+1}{\varepsilon_2 n}$ and causes a positive polarization term. As $\varepsilon_1 \to \infty$ (i.e. a polar solvent), $\alpha_n \to \frac{-1}{\varepsilon_2}$ and causes a negative polarization term. This has been shown earlier by Brus.[13] Recent experimental work by Leatherdale and Bawendi has shown that solvatochromatic shifts in the linear absorption spectra of CdSe QDs are due to changes in the dielectric polarization term.[14] The above formalism is known as the effective mass approximation (EMA), as it only uses the electron and hole effective masses to calculate the QSE.

From a rudimentary viewpoint, the EMA formalism is quite sufficient in describing most of the optical properties of QDs. However, the EMA is not widely used for rigorous theoretical studies as it shows drastic deviations from experimental values at extremely small crystallite sizes. [15] These deviations physically occur from large changes in the kinetic energies of the electron and hole and well as an increase in the number of surface atoms in the crystallite. For example, for a 20 Å diameter nanocrystal, over 40% of the crystal is comprised of surface atoms (Figure 1.2). Although QDs are modeled as spherical particles, they are actually oblate particles with crystalline facets that experience large surface strains in the small crystal regime. [16] This increased

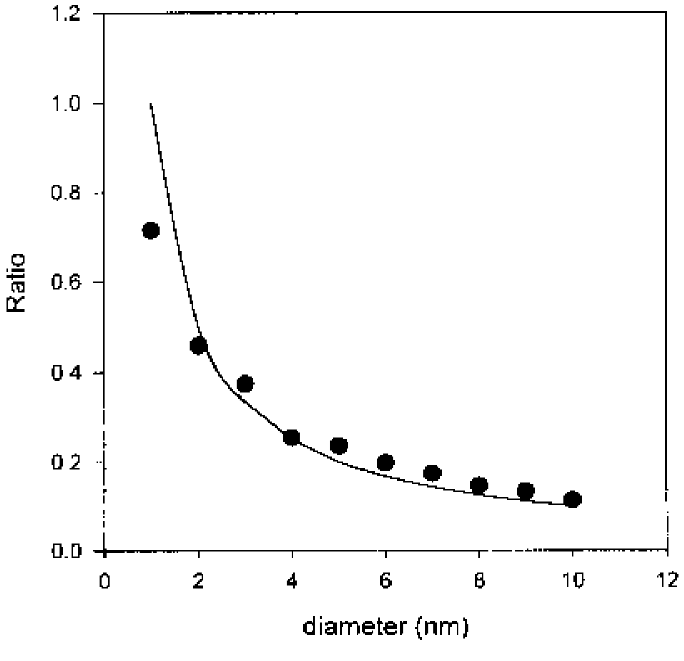

Figure 1.2. Calculation of the surface-to-volume ratio in a nanocrystal modeled as a truncated dodecahedron.

surface strain perturbs the energetics of the QD, therefore calculations that assume an infinite potential well at the QD surface do not adequately predict the QD properties. A rigorous theoretical treatment must take into account not only the properties of the electron and hole (i.e. core states), but also the properties of the surface atoms.

1.2. Electronic Structure Theory of Quantum Dots

1.2.1. Effective Mass Approximation

Efros and co-workers initially applied the EMA, briefly described above, to QDs. Most of the EMA work deals with parabolic valence and conduction bands at the top of the band (i.e. where $\partial^2 E_{v,c}/\partial^2 k = 0$). For this special behavior, the Luttinger-Kohn (LK) model is sufficient to describe the optical properties of spherical QDs. In the LK model, the hole levels are described by the parameters γ_1^L and γ^L, which determine the effective masses of the light and heavy holes. Using these methods, theorists have adequately modeled the experimental optical absorption, [17] hole burning, [18] and photoluminescence excitation spectra [19] for QDs. However, as noted above, the EMA does have shortcomings and other methods described next are needed to better describe the electronic structure of QDs.

1.2.2. Psuedopotential Calculations

Zunger's group at NREL has focused on modeling QD systems, employing density functional theory (DFT) local density approximation (LDA) calculations. In particular, Zunger uses psuedopotential calculations which represent the core atomic wavefunctions by using an empirical potential for the ionic cores. Pseudopotential wavefunctions make the assumption that only the valence electrons determine the physical properties of the system. [20] The advantages in using DFT over EMA in electronic structure calculations in QDs arises from the ability for DFT to accurately model the optical properties of strongly confined excitons. [21] DFT has been shown to be useful in evaluating the exact scaling laws for many QDs properties, which are not as simple as the scaling laws obtained from EMA.

For Zunger's calculations, the selected psuedopotential is chosen and summed over all atoms in the QD as well as the passivant,

$$H = -\frac{\hbar^2}{2\alpha m}\nabla^2 + \sum_{R_a} v_a(r - R_a) + \sum_{R_p} v_p^{(\eta)}(r - R_p) \tag{1-2}$$

where m is the electron mass, α is a fitting parameter, and v_a ($v_p^{(\eta)}$) is the atomic level empirical psuedopotentials for the core atoms (passivant). The parameter η is used to change the nature of the passivant to model different chemical environments of the QDs. Depending on the nature of the specific calculation, the Hamiltonian in eq 1-2 may contain a spin-orbit term. Employing these calculations, Zunger has shown that subtle changes in the electronegativity of the passivant may alter the symmetry of the valence band minimum (VBM). [22] The energy shift of this state ψ_n can be understood by first-order perturbation theory,

$$\Delta \in (n,\eta) = \left\langle \psi_n \middle| \sum_{R_p} \nu_p^{(\eta)}(r - R_p) \middle| \psi_n \right\rangle \qquad (1\text{-}3)$$

Equation 1-3 is essentially an overlap integral that is modulated by the electric potential of the passivant. The scaling law proposed by Zunger follows an r^{-1} dependence,

$$\Delta \in (n,\eta) \sim \alpha[n, E_p(\eta)] \frac{F[E_p(\eta)]}{r} \qquad (1\text{-}4)$$

with $F[E_p(\eta)]$ a term describing the interaction of the periodic Bloch wavefunction with the passivation potential, and $\alpha[n, E_p(\eta)]$ accounts for the extension of the envelope functions into the positions of the passivant. The most intriguing results obtained were that the recombination kinetics may be manipulated just be altering the passivation layer (i.e. surface chemistry) without changing the recombination energy. The explanation lies in the fact that more electronegative passivants tend to change the symmetry of the VBM, which causes the dark exciton state to no longer be the lowest exciton level (Fig. 1.3).

In addition, the above formalism is useful in determining the true scaling laws for many of the QD properties.[21] In particular, the exact scaling relationship between QD size and confinement energy is a necessary property

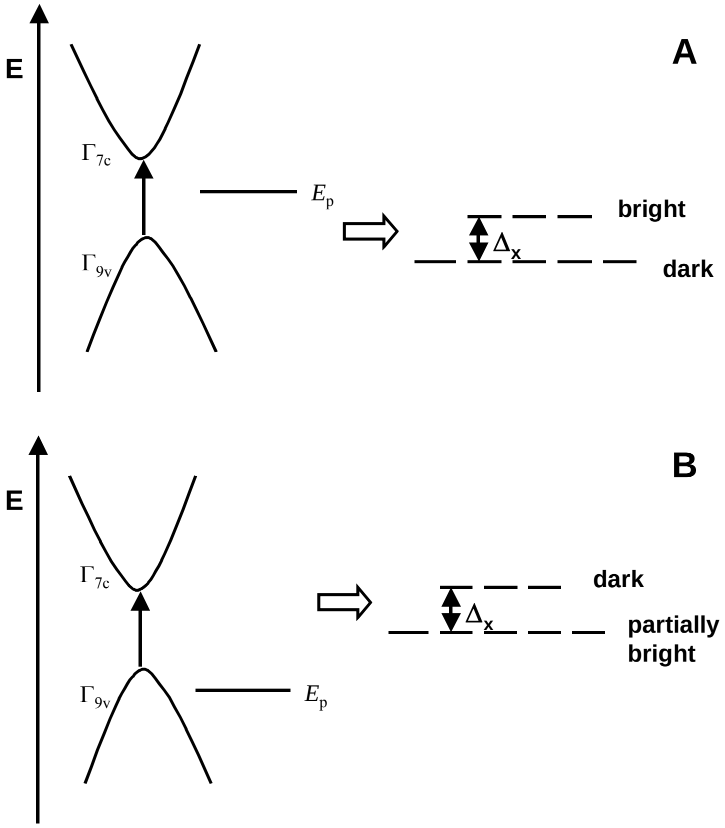

Figure 1.3. Band diagram illustration of the effect of passivant electronegativity (relative to valence band) on the excitonic levels of a quantum dot. (A) Shows the effect of an electropositive ligand binding to a QD. The exciton levels are comprised of a triply degenerate bright state and a fivefold degenerate dark ground state. The bright state has the highest contribution to the oscillator strength as the transition is symmetry allowed. (B) Shows the effect of an electronegative ligand binding to a QD. The exciton levels are comprised of a triply degenerate dark state and a fivefold degenerate partially bright ground state. The partially bright state is symmetry forbidden and results in an increase in the radiative lifetime.

to ascertain. The EMA formalism predicts the energy levels of the QD should shift as r^{-2} (both the valence and conduction bands), based upon the particle-in-a-sphere model. Psuedopotential calculations however imply that the shifts of the valence and conduction bands with particle radius are $r^{-1.21}$ and $r^{-0.95}$, respectively, while the band gap shifts as $r^{-1.01}$ which is nearly half the value expected from the EMA. [21] These results imply that an effective theoretical treatment must attempt to model not only the electronic structure of the atoms in the crystal, but also the electronic structure of the organic passivant.

1.2.3. Tight Binding Approach

The physics of the tight binding (TB) model are similar to methods used in molecular orbital theory to derive molecular wave functions. As a finite number of atoms, *n*, are brought close together, the atomic orbitals can interact (overlap) and form, as referenced in chemistry, bonding and anti-bonding orbitals. As $n \rightarrow \infty$, these bonding and anti-bonding orbital essentially become valence and conduction bands and form the basis for elementary band theory. In TB models, the total energy of the system is expressed as,

$$E = E_B + \sum_{LL'} \phi(|R_L - R_{L'}|) \tag{1-5}$$

where ϕ is a repulsive two-body potential including the ion-ion repulsion and the electron-electron interactions and R_L ($R_{L'}$) are the positions of the atoms at which the *L*th (*L'*th) basis functions are centered. The term, E_B, describes chemical bonding which and can be written as,

$$E_B = \sum_i f_i \varepsilon_i = \sum_i f_i \langle \psi_i | \hat{H}_{TB} | \psi_i \rangle$$

(1-6)

where $\hat{H}_{TB}$ is the TB Hamiltonian, ε_i and ψ_i are its eigenvalues and eigenstates, and f_i is their occupancy. The total number of valence electrons can be denoted as N and the total number of single particle states becomes $N/2$ if double occupancy, i.e., spin degeneracy for each state ($f_i = 2$) is assumed for each state. The off-diagonal elements of $\hat{H}_{TB}$ are described by invariant two-center matrix elements, $V_{ss\sigma}$, $V_{sp\sigma}$, $V_{pp\sigma}$, and $V_{pp\pi}$, between the set of orthonormal sp^3 atomic orbitals. By adjusting their values at the interatomic distance, r_o, in the equilibrium lattice structure, as well as diagonal elements E_s and E_p, a good fit to the position and dispersion of the occupied valence bands of the material can be obtained. [23]

Whaley's group at UC Berkeley has performed a lot of the work on QDs with TB methods. Her group has applied a time dependent approach, where the time dependent Schrödinger equation, $\psi(t) = \exp(-iHt)\,\psi(0)$, is used to solve the time evolution of the single particle wave function. This approach has been successful in modeling many QD properties including the single particle absorption spectra, the exciton fine structure, and permanent dipole moments. [24-26] The approach has been extended to incorporate a total energy minimization of the nanocrystal structure to incorporate surface reconstruction effects.[26] The shortcoming of the TB approach arises from the initial assumption in the model. The TB method describes the filled (valence) orbitals very well but does not model the conduction orbitals sufficiently. This is the reason why the TB approach has success in modeling the ground state properties of many QD systems, while the excited state properties have been more difficult to model.[27]

1.3. Structure and Function of Organic Passivants on Nanoparticle Surfaces

The organic passivant layer on the QD surface for a II-VI semiconductor material consists of a chemi- or physisorbed strong Lewis base typically exhibiting π-backbonding characteristics, such as organo-phosphine, -thiol, or –amine, that is believed to energetically relax defect states via ligation of partially coordinated surface atoms (dangling bonds) leading to thermodynamic stabilization of these materials at sizes smaller than their native Bohr radius.[2, 3, 28] Binding of a passivant layer also enhances confinement, and prevents aggregation in the growth process.[29, 30] The stability of the QD surfaces will therefore be dominated by the nature of the passivant surface interaction, which is dependent on the material type and the passivant headgroup, as well as the interactions between neighboring passivant moieties, as observed for self-assembled monolayers (SAM) on metal surfaces.

[31] The competition between van der Waals chain-chain (ch-ch) interactions and the amphiphilic headgroup-surface interactions can modulate the QD properties and thermodynamic stabilities in solution. In addition to enhancing particle stability, preferential binding of the passivant to specific faces of the inorganic nano-semiconductor may also influence the nature of the materials. In fact, by careful control of the chemical interactions, the shape of the materials have been systematically tuned from spherical to elliptical to elongated rods with a high aspect ratio. [6, 7] The thermodynamic stability and fundamental structural properties of these materials can be manipulated by control of the extent of coverage of the surface by the passivant layer, which is directly influenced by the ligand sterics, ligand basicity, NC type, size, and shape. Systematically, this requires an understanding of the extent to which the stability of a QD is influenced by the area available on a QD facet for surface passivation (domain) and the nature of ch-ch interactions between the passivants (dimensionality). [32-37]

1.3.1. Molecular Level Interactions – Thermodynamic Stability

To develop a more accurate picture of the passivant molecular surface interface, four distinct regions of the QDs (Fig. 1.4) can be delineated that influence the thermodynamics of the QD and the QD-passivant interaction. The passivation layer, region *A*, can be envisioned as a three dimensionally constrained monolayer of tightly packed organic amphiphiles that act to thermodynamically stabilize the surface through a headgroup-surface interaction. Region *B* consists of the molecular level interaction between the surface atoms and the head group of the passivant, which can be effectively treated as a metal-ligand bond. Region *C* encompasses the top layer of the nanomaterials that are prone to reconstruction driven by molecular interactions with the passivant layer and surface strain. Region *D* consists of the QD core and is predicted to be largely unchanged by molecular adsorption at the QD

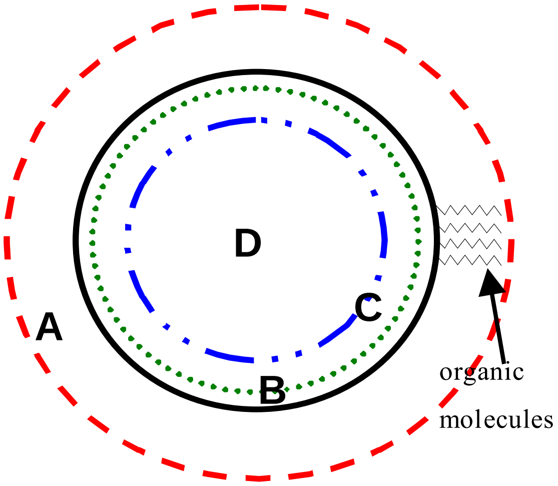

Figure 1.4. Illustration of four thermodynamic regimes of a nanoparticle. (A) Passivating layer, (B) Surface of particle, (C) Near-surface of particle, (D) Core of particle.

surface. Regions *A*-*C* are most dramatically affected by QSE and the particle crystallinity. Besides region *D*, region *A* is experimentally most trackable and can be modeled as a SAM.

While region *A* is addressable by vibrational spectroscopic techniques, regions *B* and *C* represent the most difficult to analyze, due to the low concentration of surface ions to core ions in large nanoscale materials. As the NC is reduced in size, the surface to volume ratio change leads to a condition where surface reconstruction may occur, as suggested by x-ray photoelectron (XPS), x-ray absorption (XAS), and NMR experiments. [32, 38, 39] Surface reconstruction effects have been directly observed in 17 and 28 Å InAs nanocrystals by extended x-ray absorption fine structure (EXAFS). [38] The authors found a relaxation of the outermost In layer by - 0.85 Å (inwards) and the As layer just beneath it by +0.39 Å (outwards) which effectively changes the bond lengths at the outermost surface layers. In recent NMR studies, similar surface reconstruction has been observed in Ti nanoparticles. [39] The interfacial region *A* is sensitive to the molecular level surface interaction and will be influenced by changes in the QD size, type, and shape, as well as choice of the organic passivating layer. Further experiments are required to fully understand the nature of the other interfacial regions (*B*, *C*).

In Region *A*, the organic passivant layer at the NC surface represents a 3-dimensionally constrained surface related to a 2-dimensionally confined self-assembled monolayer (SAM) on a flat metal or semiconductor surface. While the binding of organic passivants on the planar SAM surface is well established, the energetics of a molecule adsorbing to a dimensionally restricted or curved surface is more complicated than a large single crystal. Although QDs are often modeled using a “spherical” approximation, QDs are highly crystalline materials and faceted. The exposed atoms on the facets dictate the nature of the organic passivant interaction, and lead to three potential binding sites, a vertex site (V), an edge site (E), and a table site (T) (Figure 1.5). As the particle size increases or the shape changes by an increase in the particle aspect ratio, the packing densities of the organic passivant will be affected due to the change in the ratio of the available atoms at table, edge, and vertex sites. For a pseudo-spherical approximation of a faceted 40 Å QD,

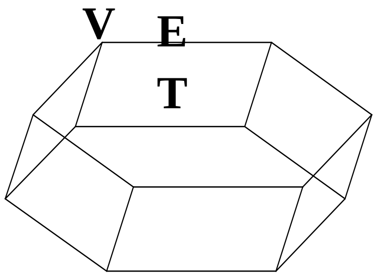

Figure 1.5. Illustration of (V) vertex, (E) edge, and (T) table sites on a nanocrystal facet.

the percentage of atoms at the surface available for interactions with a passivant layer is ~25% compared to less than 10% of the atoms on the surface of a 90 Å QD. On those surfaces, the ratio between table:edge:vertex sites is approximately 45:48:7 for the 40 Å QD compared to the ratio 80:19:1 for a 90 Å QD. It is evident that the large number of edge atoms will affect the passivant packing properties of alkyl chains, as well as potentially modulate the electronic properties of these dots. In a sense, the smaller the particle facet, the more the edge contributes to the total area of the particle thus causing an effective "surface curvature" of the particle. Surface curvature effects can lead to a number of problems including surface reconstruction, chain splaying, bundling, and interdigitation, and the competition between 2- and 3-dimensional chain packing (Fig. 1.6).

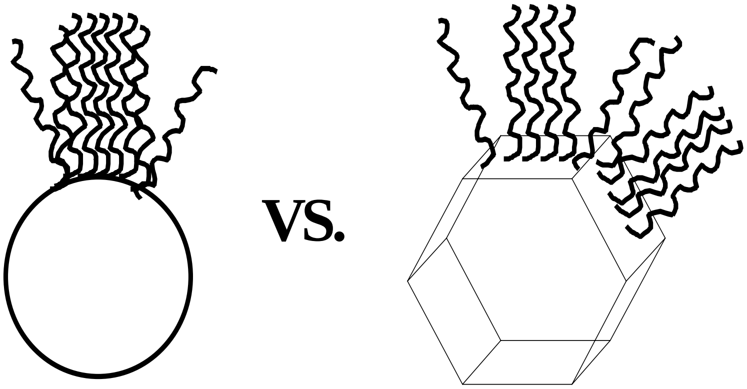

Figure 1.6. Illustration of packing on a perfect sphere and on a crystalline faceted particle. The domain model for packing is qualitatively illustrated in (B) which implies that the passivating chains have not reached a kinetically stable domain size. (A) assumes a stable domain size with chain splaying due to "surface curvature" occurring.

Recent theoretical studies by Luedtke and Landman using MD simulations have observed the effect of surface curvature on the passivant packing behavior on Au nanocrystals.[40, 41] In these studies, chain-bundling to minimize chain free volume at the surface of the nanoparticle was suggested as a result of dimensionality effects on size-constrained systems. The simulations included forces fields from all the core (Au-Au) and surfactant (R-Au) atoms. The conformational stability as well as the melting dynamics of the passivating layer was examined. Both chain length (L) and particle size (r) effects were considered. The first study involved the structure and dynamics of Au_{140} ($d \sim 17$ Å) passivated with dodecanethiol (DDT) and butanethiol (BT).[40] The authors found that chain-packing densities are nearly 50% higher on the nanocrystal than on a bulk Au surface. This occurs for Au_{140}-DDT or Au_{140}-

BT which both have a ligand length to particle radius ratio, <*L*>/*r*, greater than 1.0. Both systems have over 90% trans conformers, indicating that the low temperature gauche conformers most likely arise near the particle surface, which causes the large packing density. As the temperature of the systems is increased, increases in gauche conformers lead to a chain melt event. The authors found that the melt temperatures of the chains correlated with the free alkyl chain melt temperature, which contrasts what is seen on bulk Au surface where chain melt temperatures occur nearly 60 °C higher than the free alkyl chain. This indicates that the thermodynamics of passivant monolayers on nanocrystals are influenced greatly by the finite size of the crystallite.

In a subsequent study, Luedtke and Landman examined how the

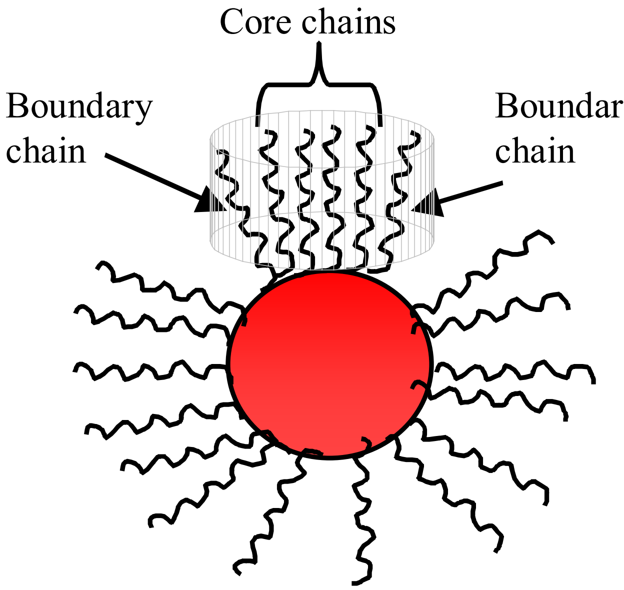

Figure 1.7. Illustration of organic molecules adsorbed on a nanocrystal. The cylindrical region represents a chain "bundle" (or chain domain) on a nanocrystal facet. The molecules at the surface (edge) of a bundle are referred to as boundary chains, while the internal molecules are referred to as core chains. The thermodynamics of the two chain regions can be different and are dependent on nanocrystal size.

particle size can influence the chain packing thermodynamics.[41] They studied the thermodynamic stability of boundary chains (BC) versus core chains (CC) (Fig. 1.7) in both Au_{140} (d ~ 17 Å) and Au_{1289} (d > 40 Å) NCs passivated with DDT. For the Au_{140}-DDT NC, $<L>/r$ ~ 1.8 while the Au_{1289}-DDT NC, $<L>/r$ <1.0. For both of these systems, two main features were evident:

(a) Before the onset of melting, BC posses more gauche defects than CC

(b) BC develop more gauche defects at a lower temperature than CC

Both have similar melting behavior, with BC gauche conformers preceding the core chain melting events. Although the Au_{1289} NC has $<L>/r < 1.0$, no difference is seen in the relative number of BC gauche conformers when compared to the Au_{140} NC. This would be expected since the Au_{1289} NC has much larger facet sizes than the Au_{140}, and can therefore stabilize a domain of chain bundles much more effectively. But upon further inspection, due to the small Au-Au spacing, the largest available facet on an Au_{1289} NC is ~22 Å, much less than the thermodynamically favored size for a stable chain bundle.

Using a 2-D SAM model as a basis point to begin the description of the molecular interaction on a QD surface in region *A* and *B*, the extent of stabilization can be treated as a competition between coordination to the surface and inter-chain interactions, which are influenced by packing densities, chain tilt angles, and surface structure. In SAMs the influence of chain length on chain crystallinity is well-established and explained using high gap impedance scanning tunneling microscopy which demonstrates that the alkanethiolate SAMs can exist in as many as six phases on the metal surface due to a direct competition between HG-HG and chain-chain (ch-ch) interactions. Knowing that the gold-sulfur binding energy (~1.66 eV) is much larger than the alkyl chain-chain interactions (~100 meV), the sulfur headgroups may exist in ordered lattices at the same time that the alkyl chains may be orientationally and conformationally disordered. The amount of order-disorder in the discrete segments of the alkyl chain will depend on the strength on the HG-surface binding strength. For instance, when long-chain organic (carboxylic, hydroxamic, phosphonic) acids form SAMs on metal oxides, the fatty acid monolayers are less stable occurring directly from the fatty acids being more physisorbed than chemisorbed. [42] In these cases, it may be necessary to have extremely long carbon chains so ch-ch interactions can compensate for the lack of HG-surface interactions. These investigations are fully described in Chapter 2 and suggest the specific properties of the passivating ligand, including chain length (CL) and head group (HG) functionality, have a direct impact on particle stability. When the ligand length, $\langle L \rangle > C_{16}$, the monolayer exists in a crystalline-like, all-trans state, whereas for $\langle L \rangle < C_8$, the local environment of the alkyl chains approaches that of the bulk disordered, liquid-like state.

The most significant differences between a 2-D SAM and a 3-D packing model for a QD are the thermodynamic free energy for the packing of the passivant layer, defined by the ch-ch interactions, will be *directly* influenced by the facet size (*dimensional* effects). Unlike the *infinite* available surface area for binding of the passivant layer to the SAM surface, a QD has a *finite* facet dimension, which will tend to give rise an effective increase in the area per headgroup of the passivant due to a propensity for splaying of the chains at the facet edge in order to minimize thermodynamic free energy by filling free volume. This will decrease packing densities of the passivant at the QD surface. Coupled to the dimensionality (size-dependent) effects for a QD compared to a 2-D SAM, the crystalline packing of the passivant moiety will also exhibit a thermodynamic minimum domain size (available facet dimension - *domain*) that allows a thermodynamically stable crystalline packing domain arising from strong ch-ch interactions for the passivant layer on the QD particle. The appearance of minimum domain structures of organic amphiphiles on bulk SAMs has been well documented and is seen to typically be between 40-50 Å. [31] This suggests that as the particle size decreases below a 50 Å facet, the thermodynamic energetics of chain packing may be disturbed and domain effects may be observed for passivant packing in QDs. These two competitive influences on a QD surface predicts both a QD size dependent and passivant type dependent behavior for the energetics of ch-ch interactions in these materials which can be described systematically as a dimensional and domain effects and are fully described in Chapter 3.

1.3.2. Molecular Level Interactions – Interfacial Effects

In addition to the effect of region *A* on the thermodynamic stability of a QD, it is quite evident that regions *B* and *C* can have tremendous influence on the particle stability and its core properties (region *D*). Two methods than can be used to probe the influence of the interfacial regions on the bulk properties are Raman and photoluminescence spectroscopies, both at ambient conditions and at high pressures and temperatures. These types of experiments will be described in detail in Chapters 4 and 5.

1.3.2.1. Raman Spectroscopy of Quantum Dots

For a dimensionally confined crystal, phonon confinement (PC) can have a drastic impact on the absolute energy of the optical phonons. [43] When the crystal exhibits PC effects, the optical phonon energies are shifted to the red. PC effects can be estimated quantitatively in terms of the phonon correlation length, *L*, which corresponds to a size of phonon confinement by a nanocrystal. As a result of PC, the phonon wave function becomes finite and therefore the $\mathbf{q} = 0$ selection rule relaxes, where $\mathbf{q}$ is the wave vector in reciprocal space.

Reciprocal space is related to three dimensional direct space by the relation, $\exp(i\boldsymbol{G}\cdot\boldsymbol{T}) = 1$, where $\boldsymbol{T}$ is the direct (space) translation vector and $\boldsymbol{G}$ is the reciprocal (space) translation vector. Therefore, if one defines the central Wigner –Seitz cell, or the cell defined by the three fundamental translational vectors, in terms of the reciprocal lattice vector rather than the direct lattice vector, one obtains the first Brillouin zone (BZ). The difference in constructing a BZ compared to a direct unit cell is that the reciprocal lattice vectors are used in constructing the BZ. The relationships between the direct lattice vectors, $\boldsymbol{x}$, $\boldsymbol{y}$, and $\boldsymbol{z}$, and the reciprocal lattice vectors, $\boldsymbol{q_x}$, $\boldsymbol{q_y}$, and $\boldsymbol{q_z}$, are $\boldsymbol{q_x} = 2\pi/\Omega\ (\boldsymbol{y} \times \boldsymbol{z})$, $\boldsymbol{q_y} = 2\pi/\Omega\ (\mathbf{z} \times \boldsymbol{x})$, and $\boldsymbol{q_z} = 2\pi/\Omega\ (\boldsymbol{x} \times \boldsymbol{y})$, where Ω is the volume of the primitive unit cell (Wigner-Seitz cell) of the direct lattice. [44]

Because of PC, phonon modes from a wider range in the BZ are allowed to contribute to the Raman spectrum. The allowed range is described by $\Delta\mathbf{q} \sim 1/L$, where L is called phonon correlation length. If the phonon wave function is described by $\Phi(\mathbf{q}_o,\mathbf{r}) = u(\mathbf{q}_o,\mathbf{r})e^{i\mathbf{qr}}$, where $u(\mathbf{q}_o,\mathbf{r})$ has the periodicity of the lattice, then PC will modify the phonon wave function to,

$$\Psi(\mathbf{q_o},\mathbf{r}) = W(\mathbf{r},L)\Phi(\mathbf{q_o},\mathbf{r}) = \Psi'(\mathbf{q_o},\mathbf{r})u(\mathbf{q_o},\mathbf{r}) \qquad (1\text{-}7)$$

where $W(\mathbf{r}, L)$ is a weighting function. If the perturbed wave function, Ψ', is expanded into a Fourier series,

$$\Psi'(\mathbf{q_o},\mathbf{r}) = \int_q C(\mathbf{q_o},\mathbf{q})e^{i\mathbf{qr}}d^3q \qquad (1\text{-}8)$$

the Fourier coefficient, $C(\mathbf{q_o},\mathbf{q})$, can be described as,

$$C(\mathbf{q_o},\mathbf{q}) = \frac{1}{(2\pi)^3}\int_r \Psi'(\mathbf{q_o},\mathbf{r})e^{i\mathbf{qr}}d^3r\,. \qquad (1\text{-}9)$$

If a Gaussian weighting function centered at $\mathbf{q_o}$ is considered, the Fourier coefficient becomes $|C(0,\mathbf{q})|^2 \sim \exp(-L^2q^2/2\alpha)$, where α is dependent on the crystal type. The one-phonon Raman spectra can then be calculated by,

$$I(\omega,L) = \frac{L^3}{2\pi^{3/2}}\int_0^1 \frac{|C(\mathbf{0},\mathbf{q})|^2}{[\omega-\omega(\mathbf{q})]^2+\left(\Gamma/2\right)^2}dq \qquad (1\text{-}10)$$

where $\omega(\mathbf{q})$ is the bulk phonon dispersion relation and Γ is the natural linewidth.

For CdSe, the system discussed in this dissertation, the lowest energy optical phonon, called the longitudinal optical phonon, occurs at 213.1 cm^{-1} in the bulk crystal. [43] CdSe has two atoms in its primitive Wigner-Seitz cell, therefore, CdSe should have 3 acoustical branches and 3 optical branches: one longitudinal acoustic (LA), one longitudinal optical (LO), two transverse acoustic (TA) and two transverse optical (TO) modes. [44] Due to the zone center selection rule for the inelastic scattering of visible light, acoustic modes are not generally seen in a Raman experiment due to their positive dispersion relation. For bulk CdSe, a TO phonon has been observed at ~169 cm^{-1}, however this is not seen in the QD analogue possibly due to symmetry considerations. Possible evidence for the CdSe QD TO mode has been suggested from far infrared experiments. [45] PC effects can shift the CdSe LO phonon energy from ~213 cm^{-1} to <200 cm^{-1}. [43] There are, however, many other intriguing effects that can modify the Raman spectra of dimensionally restricted materials.

One effect that can occur is the appearance of interface (IF) modes. [46] These IF modes are a direct result of the physics of regions *A* and *B* and a common formalism to discuss IF modes in are the dielectric continuum approach (DCA). [47] In the DCA, a single dot with dielectric function, $\varepsilon_1(\omega)$, embedded in a second material with dielectric function, $\varepsilon_2(\omega)$, is considered (Fig. 1.9). Each dielectric surface is characterized by dispersionless LO and TO modes, and the dielectric functions are,

$$\varepsilon_i(\omega) = \varepsilon_{\infty,i} \frac{\omega_{\mathrm{LO}.i}^2 - \omega^2}{\omega_{\mathrm{TO}.i}^2 - \omega^2}, \quad i = 1, 2 \qquad (1\text{-}11)$$

Because no net charge is assumed to reside in either material, Maxwell's equations can describe the electromagnetic field, in particular, $\varepsilon_i(\omega)\nabla\bullet\mathrm{E} = 0$.

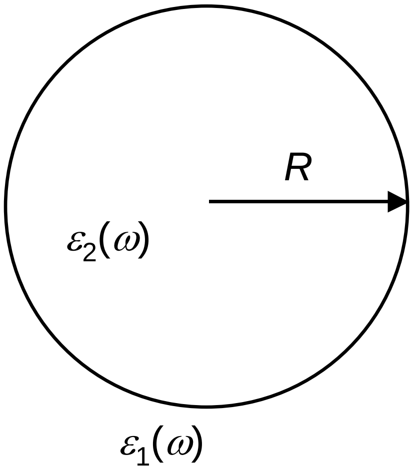

Figure 1.8. Model used for calculation of interface modes using a dielectric continuum approach. The model assumes a sphere of radius, *R*, embedded in an infinite dielectric matrix. The values ε_1 and ε_2 represent the surrounding and QD dielectric functions, respectively.

The electrostatic potential, Φ, can be expressed for a sphere of radius, *R*, as

$$\Phi(r,\theta,\phi) = \exp(im\phi)P_l^m(\cos\theta)\times\begin{cases}(r/R)^l, r \le R \\ (R/r)^{l+1}, r \ge R\end{cases} \qquad \text{(1-12)}$$

where the integers *l* and *m* are interface mode quantum numbers and P_l^m are associated Legendre polynomials. The only discontinuity in ∇Φ occurs at $r = R$, therefore the suitable boundary condition requires that,

$$\frac{\varepsilon_1(\omega_{lm})}{\varepsilon_2(\omega_{lm})} = -1 - \frac{1}{l}. \qquad \text{(1-13)}$$

By substituting Eq. 1-11 into Eq. 1-13, the IF mode frequencies can be obtained. The expected values for IF modes in CdSe are seen in Table 1.1.

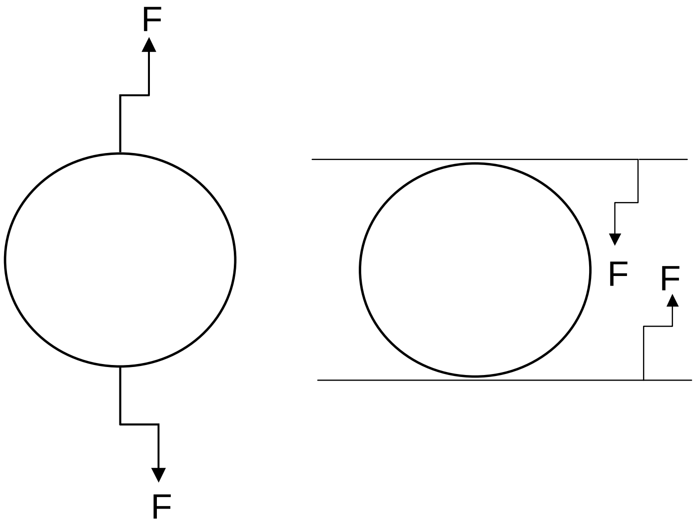

Figure 1.9. Effect of stress on a sphere. (A) represents tensile stress, where the kinked arrow designates an applied force away from the center of the sphere. (B) represents compressive stress, where the kinked arrow designates an applied force towards the center of the sphere.

Another effect that can perturb the Raman spectra of a quantum dot involves the presence of strain in the nanomaterial. Strain can arise in two forms, either tensile or compressive strain (Fig. 1.10). Tensile strain tends to lower (red shift) the frequency of the phonon modes of a crystal while compressive strain tends to raise (blue shift) the frequency of the phonon modes. [46] Strain is a by-product of an applied stress, such as pressure. For instance, it is well known that the application of hydrostatic pressures to a semiconductor crystal causes a blue shift in the LO phonon modes, [48] which as described above is due to compressive strain in the lattice. In finite crystals, the increase in the number of surface to core atoms can impose a static stress on the crystal, most likely arising from surface tension effects. Using models developed for micelles, [49] the internal stress, P, arising from surface tension can be described by,

Table 1.1. Calculated interface modes for various semiconductors coated on CdSe.

	ω_{LO} (cm^{-1})	ω_{TO} (cm^{-1})	ε_∞	ω_{LM} (cm^{-1})
CdO	569	326	2.1	181, 451
CdS	305	243	5.2	179, 289
CdSe	213.1	169	5.8	n/a
ZnS	351	279	5.7	179, 332
ZnSe	250	205	5.7	179, 242

$$P = \frac{2\gamma(R)}{R} \qquad (1\text{-}14)$$

where $\gamma(R) = A + B\,R^{-2}$ and represents the size dependent surface tension and R is the particle radius. The constants A and B are related to the surface tensions of some low-index flat surface and the increase in surface tension to bend that flat surface in a sphere, respectively. Tolbert and Alivisatos [9] first used the size dependent surface tension model to describe the size dependent solid-solid phase transition in CdSe QDs. Using the expression for $\gamma(R)$ and eq. 1-14, the internal stress from surface tension in a QD is described as,

$$P = 2\left(\frac{A}{R} + \frac{B}{R^3}\right) \qquad \text{(1-15)}$$

Fig. 1.11 shows the graphical representation of eq. 1-14 using the values obtained in Ref. 9 for A (0.34 N m^{-1}) and B (84 N Å^2 m^{-1}). From fig. 1.11, we see the internal pressure of a QD varies from ~2.5 GPa at a particle radius of ~10 Å to <500 bar (0.05 GPa) for a particle radius of ~40 Å. Fig. 1.11 does not explicitly determine whether a QD will experience compressive or tensile

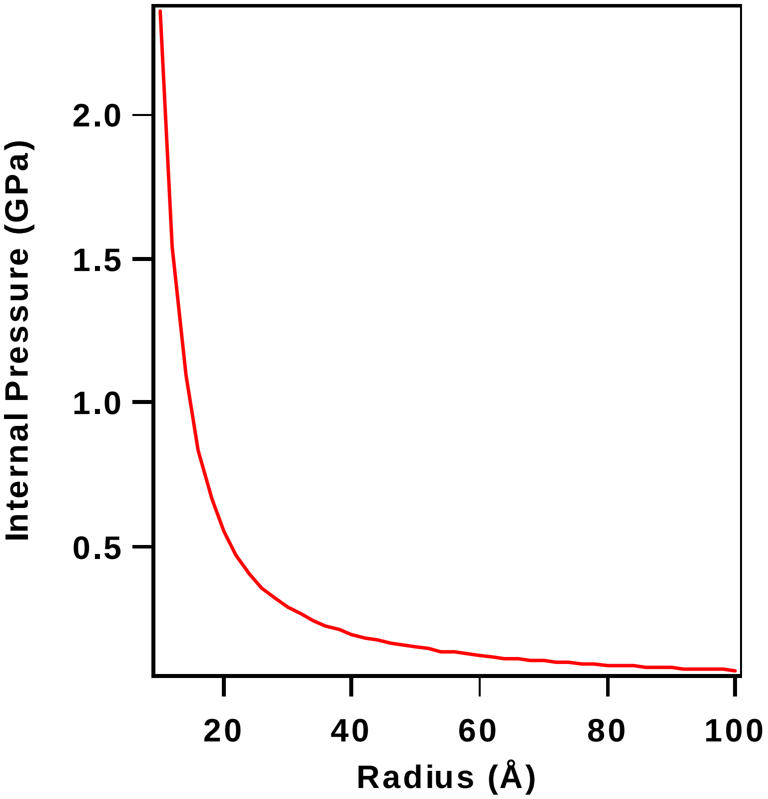

Figure 1.10. Effect of surface tension (plotted as internal pressure) as a function of QD radius.

stress, but it does confirm the existence of an effective static pressure on the QD, exhibited in the form of the surface tension. Analysis of the phonon spectra as a function of size and material can be useful in determining the contribution of surface tension to the properties of the QD. This will be described in Chapter 5.

1.3.2.2. Effect of Pressure on the Photophysics of Quantum Dots

Conventional high-pressure techniques utilize a diamond anvil cell (DAC) to generate the extreme conditions. [50] DACs consist of brilliant cut diamonds flattened at the tip. Between the two flattened tips, a metal gasket (traditionally stainless steel or Be-Cu) encloses a sample embedded in a 25 μm hole drilled into the gasket. For hydrostatic conditions, a pressure-transmitting medium (such as methanol/ethanol) is added to the gasket hole. DACs are used in nearly all high-pressure applications except for ultraviolet and soft x-ray regions (because diamond is opaque between 5 eV and 5 keV) and the far infrared region (because the gasket hole dimension can diffract the IR radiation).

Studies of the effect of pressure on the photoluminescence (PL) spectra can be useful in many regards. Changes in the linewidths and peak positions can give important information on how the excited state is coupled to the lattice. Impurity ions that reside in the lattice can cause intriguing pressure effects, and give information on size and impurity effects on electron-phonon coupling and lattice ionicity. [51]

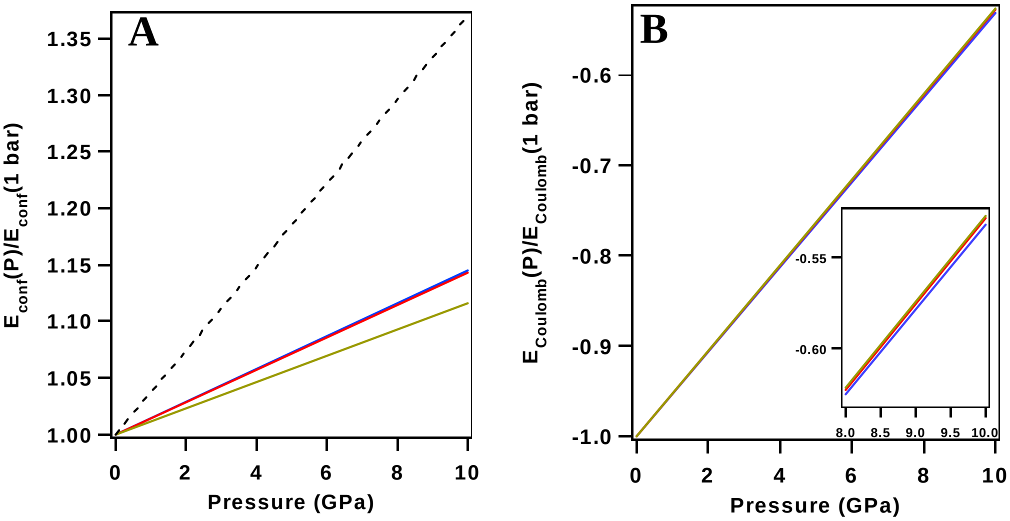

Figure 1.11. The effect of pressure on the (A) confinement energy and (B) Coulomb energy as a function of particle size. The particles sizes are 30 A (blue), 55 A (red), and 70 A (brown). In (A) the bulk pressure dependence is shown in black. In (B), the inset shows the region from 8-10 GPa where a noticeable change in the Coulomb energy occurs.

Using eq. 1-1, some simple models to describe PL pressure tuning in QDs can be generated. The pressure dependence of the QD PL is a function of all four terms in eq. 1-1. The first term, E_g^{bulk}, is the pressure dependence of the PL energy of bulk CdSe. The functional form of this relationship is expressed as, $E(\mathrm{P}) = E_{1\ \mathrm{bar}} + \alpha \mathrm{P}$, where α is called the PL pressure coefficient. Mei and Lemos [52] found $\alpha = 58$ meV GPa^{-1} for bulk wurtzite CdSe.

The more important term for a QD, however, is how the second term in eq. 1-1, the confinement term, varies with pressure. A way to quantify the pressure dependence of this term is through the Murnaghan equation of state, $V/V_o = \left[1 + \left(B_o^{'}/B_o\right)P\right]^{1/B_o^{'}}$. Due to the cubic relationship between volume and radius ($\propto R^3$) the Murnaghan equation of state can be re-written in terms of R as,

$R/R_o = \left\{\left[1 + \left(B_o^{'}/B_o\right)P\right]^{1/B_o^{'}}\right\}^{1/3}$. This equation states that the fractional compression of the lattice with pressure can be described as a fractional compression of the QD radius (i.e. an increase in confinement). The fractional change in QD radius can be related to energy ($\propto R^{-2}$) and this relation as a function of size is seen in Fig. 1.12a. From fig. 1.12a, it is evident that confinement energy for the 30 and 55 Å diameter QDs are most affected by pressure, while the 70 Å diameter QD is significantly less affected by pressure, as expected for a particle whose radius is beginning to approach the Bohr radius of the system.

The third and fourth terms in eq. 1-1 are expected to increase with pressure. This is more an empirical assumption, based upon the densification of the QD and the organic coating leading to an increase in the dielectric constants of the materials. [53] The functional relationship can be described as

$$E_{Coulomb}^{QD}(P) = -\frac{1.8e^2}{\varepsilon_2(P)R} + \frac{e^2}{R}\overline{\sum_{n=1}^{\infty}\alpha_n(P)\left(\frac{S}{R}\right)^{2n}} \quad . \qquad (1\text{-}16)$$

For instance, the Coulomb energy term arising from the QD electron-hole pair has an attraction energy of ca. –109 meV for a 50 Å diameter CdSe QD. Increasing the pressure from 1 bar to 5 GPa leads to ~4% decrease in particle radius and as an assumption, we assume the particle dielectric constant increases by 1.5. Using these numbers, the Coulomb energy at 5 GPa is ca. –74.7 meV, an increase in ~34 meV. This is graphically represented is Fig 1.12b, where the pressure dependence of the Coulomb energy term is plotted as a function of size. It is evident that it takes relatively high pressures to discern a noticeable difference in the pressure dependence of the Coulomb energy; therefore, it is more likely a small perturbation that can be neglected in most experimental conditions. Similar calculations can be performed for the fourth term in eq. 1-1, the solvent dielectric term.

The information in this section shows that the main contributions to the high-pressure photophysics of QDs arise from the pressure dependence of the bulk and confinement energy terms, while the Coulomb energy terms can be neglected as a small perturbation. This shall be useful knowledge in Chapter 4, where the analysis of CdSe PL and Raman spectra under small hydrostatic pressures is examined.

1.4. Summary of Dissertation

The underlying scientific concepts discussed in this dissertation are probing the surfaces of nano-scale materials and how those surfaces can influence the physics of these materials. In Chapter 2, I describe the thermodynamic analysis of *n*-hexadecylamine, a long chain surfactant, passivated on the surface of a CdSe QD. I will detail the existence of a free energy minimum for chain stabilization that depends on the interplay between the particle radius and chain length of the surfactant. In Chapter 3, I will discuss a mean field statistical mechanical approach to describe the experimental observation of the free energy minimum in Chapter 2. In addition, Chapter 3 discusses the observation of domain sizes on CdSe QDs, and the impact that has on nanoparticle stability. In Chapter 4, the influence of these surface states on the photoluminescent properties of CdSe QDs is examined. I will detail the existence of donor states in CdSe QDs that can cause deviations to the optical properties of these materials. Chapter 5 builds on the concepts laid out in Chapter 4 by using vibrational spectroscopy to probe the influence of surface strain on various colloidal preparations of CdSe QDs. The strain may be related to the donor states observed in Chapter 4. Finally, in Chapter 6, I will detail the first analysis of the electronic and defect structures of QDs using positron spectroscopy. The trends in the data suggest that the colloidal preparation used to prepare CdSe QDs changes the physics of the dot, as suggested in Chapter 5.

1.5. References

1 A. P. Alivisatos, Journal of Physical Chemistry **100**, 13226 (1996).

2 C. B. Murray, D. J. Norris, and M. G. Bawendi, Journal of the American Chemical Society **115**, 8706 (1993).

3 M. A. Hines and P. GuyotSionnest, Journal of Physical Chemistry B **102**, 3655 (1998).

4 O. I. Micic, C. J. Curtis, K. M. Jones, J. R. Sprague, and A. J. Nozik, Journal of Physical Chemistry **98**, 4966 (1994).

5 Y. W. Jun, Y. Y. Jung, and J. Cheon, Journal of the American Chemical Society **124**, 615 (2002).

6 X. G. Peng, J. Wickham, and A. P. Alivisatos, Journal of the American Chemical Society **120**, 5343 (1998).

7 X. G. Peng, L. Manna, W. D. Yang, J. Wickham, E. Scher, A. Kadavanich, and A. P. Alivisatos, Nature **404**, 59 (2000).

8 A. N. Goldstein, C. M. Echer, and A. P. Alivisatos, Science **256**, 1425 (1992).

9 S. H. Tolbert and A. P. Alivisatos, Journal of Chemical Physics **102**, 4642 (1995).

10 M. Nirmal, D. J. Norris, M. Kuno, M. G. Bawendi, A. L. Efros, and M. Rosen, Physical Review Letters **75**, 3728 (1995).

11 R. W. Meulenberg and G. F. Strouse, Physical Review B-Condensed Matter **66**, 035317 (2002).

12 N. F. Johnson, Journal of Physics-Condensed Matter **7**, 965 (1995).

13 L. E. Brus, Journal of Chemical Physics **80**, 4403 (1984).

14 C. A. Leatherdale and M. G. Bawendi, Physical Review B **6316**, 5315 (2001).

15 C. B. Murray, MIT, PhD Thesis (1995).

16 J. J. Shiang, A. V. Kadavanich, R. K. Grubbs, and A. P. Alivisatos, Journal of Physical Chemistry **99**, 17417 (1995).

17 A. I. Ekimov, F. Hache, M. C. Schanneklein, D. Ricard, C. Flytzanis, I. A. Kudryavtsev, T. V. Yazeva, A. V. Rodina, and A. L. Efros, Journal of the Optical Society of America B-Optical Physics **10**, 100 (1993).

18 D. J. Norris, A. Sacra, C. B. Murray, and M. G. Bawendi, Physical Review Letters **72**, 2612 (1994).

19 D. J. Norris and M. G. Bawendi, Physical Review B-Condensed Matter **53**, 16338 (1996).

20 http://www.tcm.phy.cam.ac.uk/~mds21/report/node10.html#SECTION 00540000000000000000 .

21 A. J. Williamson and A. Zunger, Physical Review B **61**, 1978 (2000).

22 F. A. Reboredo and A. Zunger, Physical Review B **6323**, 5314 (2001).

23 http://monet.physik.unibas.ch/~abdu/ontb/node3.html .

24 N. A. Hill and B. Whaley, Journal of Chemical Physics **99**, 3707 (1993).

25 K. Leung, S. Pokrant, and K. B. Whaley, Physical Review B-Condensed Matter **57**, 12291 (1998).

26 K. Leung and K. B. Whaley, Journal of Chemical Physics **110**, 11012 (1999).

27 N. A. Hill and K. B. Whaley, Physical Review Letters **75**, 1130 (1995).

28 S. L. Cumberland, K. M. Hanif, A. Javier, G. A. Khitrov, G. F. Strouse, S. M. Woessner, and C. S. Yun, Chemistry of Materials **14**, 1576 (2002).

29 M. G. Bawendi, P. J. Carroll, W. L. Wilson, and L. E. Brus, Journal of Chemical Physics **96**, 946 (1992).

30 L. R. Becerra, C. B. Murray, R. G. Griffin, and M. G. Bawendi, Journal of Chemical Physics **100**, 3297 (1994).

31 L. H. Dubois and R. G. Nuzzo, Annual Review of Physical Chemistry **43**, 437 (1992).

32 J. E. B. Katari, V. L. Colvin, and A. P. Alivisatos, Journal of Physical Chemistry **98**, 4109 (1994).

33 T. Prozorov and A. Gedanken, Advanced Materials **10**, 532 (1998).

34 S. R. Cordero, P. J. Carson, R. A. Estabrook, G. F. Strouse, and S. K. Buratto, Journal of Physical Chemistry B **104**, 12137 (2000).

35 B. S. Kim, L. Avila, L. E. Brus, and I. P. Herman, Applied Physics Letters **76**, 3715 (2000).

36 R. W. Meulenberg and G. F. Strouse, Journal of Physical Chemistry B **105**, 7438 (2001).

37 R. W. Meulenberg, S. Bryan, C. S. Yun, and G. F. Strouse, Journal of Physical Chemistry B **106**, 7774 (2002).

38 K. S. Hamad, R. Roth, J. Rockenberger, T. van Buuren, and A. P. Alivisatos, Physical Review Letters **83**, 3474 (1999).

39 E. Scolan, C. Magnenet, D. Massiot, and C. Sanchez, Journal of Materials Chemistry **9**, 2467 (1999).

40 W. D. Luedtke and U. Landman, Journal of Physical Chemistry **100**, 13323 (1996).

41 W. D. Luedtke and U. Landman, Journal of Physical Chemistry B **102**, 6566 (1998).

42 A. Badia, R. B. Lennox, and L. Reven, Accounts of Chemical Research **33**, 475 (2000).

43 C. TralleroGiner, A. Debernardi, M. Cardona, E. MenendezProupin, and A. I. Ekimov, Physical Review B-Condensed Matter **57**, 4664 (1998).

44 C. Kittel, *Introduction to solid state physics* (Wiley, New York, 1996).

45 M. I. Vasilevskiy, A. G. Rolo, M. V. Artemyev, S. A. Filonovich, M. J. M. Gomes, and Y. P. Rakovich, Physica Status Solidi B-Basic Research **224**, 599 (2001).

46 H. Rho, H. E. Jackson, S. Lee, M. Dobrowolska, and J. K. Furdyna, Physical Review B **61**, 15641 (2000).

47 P. A. Knipp and T. L. Reinecke, Physical Review B-Condensed Matter **46**, 10310 (1992).

48 F. Cerdeira, C. J. Buchenauer, F. H. Pollak, and M. Cardona, Physical Review B **5**, 580 (1972).

49 I. Szleifer, D. Kramer, A. Ben-Shaul, W. M. Gelbart, and S. A. Safran, Journal of Chemical Physics **92**, 6800 (1990).

50 A. Jayaraman, Review of Scientific Instruments **57**, 1013 (1986).

51 L. D. Merkle, I. L. Spain, and R. C. Powell, Journal of Physics C: Solid State Physics **14**, 2027 (1981).

52 J. R. Mei and V. Lemos, Solid State Communications **52**, 785 (1984).

53 B. S. Kim, M. A. Islam, L. E. Brus, and I. P. Herman, Journal of Applied Physics **89**, 8127 (2001).

PART I: Analysis of the Thermal Behavior of Alkylamines on Semiconductor Quantum Dot Surfaces Using Attenuated Total Reflection Infrared Spectroscopy

Chapter 2: Thermodynamics and Packing Analysis of *n*-Hexadecylamine on CdSe Quantum Dot Surfaces

Most of this chapter has appeared in print: Meulenberg, R.W.; Strouse, G.F. *J. Phys. Chem. B* **105**, 7438-7445 (2001)

2.1. Introduction

Nanoscale materials in the size regime 1 – 100 nm (10 – 1000 Å) have long held promise for applications ranging from electronics, to catalysis, to non-linear opto-electronic materials.[1] Materials (metals, semiconductors, or insulators) at the nanoscale exhibit bulk like crystallographic properties yet have physical properties governed by the particle size arising from the strong confinement of the charge carriers.[2] This class of semiconductor quantum dot (QD) materials can be readily prepared using lyothermal techniques producing narrow size distributions (5-8%) of materials that are surface passivated by amphiphillic molecules and fully dispersible in organic solvents.[3, 4] The unique physical properties and ease of processing these materials has resulted in a drive to harness the core-dependent properties, while the surface passivation layer has been largely ignored.

Typically, the surface layer consists of strong Lewis bases that act to thermodynamically stabilize the surface through a headgroup-surface interaction via coordination to the QD surface. The monolayer consists of organic moieties with long chain functionalized alkanes, where the functionalities can be phosphines,[3] thiols,[5] or amines,[4] similar to a self-assembled monolayer (SAM), Langmuir-Blodgett (L-B) film, micelle, or liquid crystal. While SAMs represent surfaces with appended amphiphiles constrained in 2-dimensions, the passivation on a quantum dot is constrained 3-dimensionally. The constrained surfaces of these materials should exhibit a varied order/ disorder behavior for the surface passivated layer which correlates with passivant chain length, chain packing, and QD size. Recent efforts to understand the molecular level interactions and reactivity in nanoscale materials include small molecule surface binding effects on photoluminescence,[6, 7] NMR of the organic passivating layer,[8, 9] varying of the capping layer moiety,[10-12] influence of the quantum dot shape,[13] and vibrational and thermotropic analysis of materials[14-18]. These studies indicate that the primary function of the capping moiety for the QD is minimization of particle agglomeration arising from Ostwald ripening, as well as passivation of the surface electronic states via surface reconstruction of dangling bonds at the solution/ nanoparticle interface. Due to the large surface-to-volume ratios in these materials, the molecular level interactions of the passivant layer may also dominate particle-particle interactions in self-assembled 3-dimensional structures. Furthermore, surface curvature effects may modulate the thermodynamics of chain packing at these surfaces.

Surface curvature effects play a substantial role in the importance of the passivant layer on a nanocrystal surface since the interdot interactions in 3-dimensional assemblies are affected by the density of packing of the passivant layer at the surface of the nanocrystal. As the surface curvature increases, the packing density decreases due to an increase in free volume for the passivant chains. In SAM structures and metalo-mesogenic structures, where the surface is nominally flat, a 2-step melting curve is observed for the organic phase,[19, 20] due to limitation of both rotational and translational degrees of freedom for the tightly packed monolayer structures. Nuzzo, et al demonstrated a thermotropic transition in SAMs that has not been observed on nanomaterial surfaces arising from thermotropic activation of rotational degrees of freedom.[19] This low temperature transition in crystalline gold SAM structures results in the ordering of the alkanethiol chains transform from orthorhombic to a modified hexagonal "rotator" phase coupled to a significant increase in gauche defect population of the polymethylene chains.[21] Such rotational transitions may also arise in nanomaterials where surface curvature effects may effect rotational, as well as translational degrees of freedom. In evaporatively assembled nanocrystals, surface curvature and the ratio of particle radius to chain length will influence the passivant layer packing and therefore its thermotropic behavior. Depending on this ratio a 3-d assembly may be observed, in which dot-dot interactions exhibit inter-dot, single-chain and chain-bundle interdigitation to minimize chain free volume at the surface of the nanomaterial.[14, 16, 18] MD calculations[22] confirmed the importance of inter-material interactions and surface curvature effects in these materials.

To clearly separate the influence of surface curvature effects on surface packing in QDs, as well the as forces governing chain packing (i.e. chain interdigitation), correlation of thermodynamic data and local chain structure on the QD surface is required. In order to gain insight into the nature of chain packing and melting phenomena in QDs, we have performed correlated temperature-dependent FTIR and DSC measurements on QD glassy thin films. By comparing this data with temperature-dependent pXRD and TEM measurements, we show that chain packing in CdSe nanoparticles is comprised of three limits when deposited as a film, with 2- and 3-dimensional effects being the extremes. This behavior is also reflected in QD solutions, suggesting that the packing behavior arises largely from single dot effects, rather than dot-dot interactions. We present thermodynamic data that illustrates the three regimes are governed by the ratio of passivant chain length to nanoparticle radius and give rise to changes in packing densities and chain conformations at the QD surface.

2.2. Experimental

2.2.1. Materials. CdSe QDs were synthesized by a modification of standard lyothermal methods using either tri-octylphospine/ oxide (TOP/O) or *n*-hexadecylamine (HDA) as the growth solvent.[3, 23] Recapping of the CdSe was accomplished by ligand exchange techniques and verified by FT-IR spectroscopy. Crystallinity and size dispersity of the materials are monitored by absorption, pXRD, and TEM analysis. Typical size dispersites are 5-8% depending on growth method.

2.2.2. Thermotropic measurements. All thermal measurements unless noted were performed on thin glassy films in order to allow direct comparison of the thermotropic behavior.

2.2.2.1. ATR-FTIR Spectroscopy. QD samples were dispersed in hexane, deposited on a 4 X 80 mm ZnSe 45º HATR plate (Pike Technologies), and allowed to slowly evaporate. Temperature dependent ATR-FTIR data were collected on a Perkin-Elmer Spectrum GX system from 650-4000 cm^{-1} with a resolution of 2 cm^{-1}. Temperature control between 25-120 ºC (± 1 ºC) was achieved using a manual temperature control (Pike Technologies) coupled to the HATR plate.

2.2.2.2. DSC measurements. QD samples were dispersed in hexane, deposited on an Al crucible, and allowed to slowly evaporate. The weight was recorded within ± 0.2 mg. DSC data was performed on a Perkin Elmer (DSC-7) under N_2 between 25 and 120 °C (298 - 393 K) at a heating rate of 5 °C min^{-1}. Calorimetric data was recorded by fitting the area under the endotherm transitions. The DSC measurements are not background subtracted in order to eliminate contributions from baseline filtering. Thermodynamic quantities are the average of multiple runs from several samples to minimize batch-to-batch anomalies. All the DSC traces exhibit an exothermic return consistent with reversible transitions. TGA/ DTA measurements indicate no mass loss in the temperature range studied and indicate that ~20% of the QD mass arises from the surface passivating layer (depending on chain length).

2.2.2.3. Small Angle Powder X-Ray Diffraction (SAXS). SAXS data was taken on a Philips X'PERT MPD diffractometer using Cu Kα radiation (λ = 1.5418 Å). Temperature measurements were performed between 25 – 80 ºC (± 1 ºC).

2.2.2.4. Transmission Electron Microscopy (TEM). TEM analysis was obtained on a JEOL 2010 microscope operated at 200 kV in bright field mode using Ni-backed holey carbon TEM grids (SPI) with the *formvar* removed.

Size and size distribution measurements were obtained on a statistical subset of QDs by manual calculation of the QD images obtained by digitizing the micrograph negatives.

2.3. Results

2.3.1. Room Temperature Infrared Absorption. Complete assignments of the infrared transitions for various particle sizes, chain lengths, and head groups in analogy to modes observed in crystalline *n*-alkanes and SAMs are exhaustively listed in Tables 2.1 – 2.6.[15,15, 24, 25] Comparison of IR data for CdSe between 26 Å and 90 Å capped with HDA is presented in Tables 2.1 and 2.4. FT-IR comparisons of alkylamine chain lengths of 8 and 16 carbon units are given in Tables 2.3 and 2.5. Comparison of different CdSe capping ligands, HDA, HDT (hexadecylthiol), and TOP/O, are given in Tables 2.2 and 2.6. For clarity, only the 41 Å CdSe passivated with HDA is fully described in detail in the following sections.

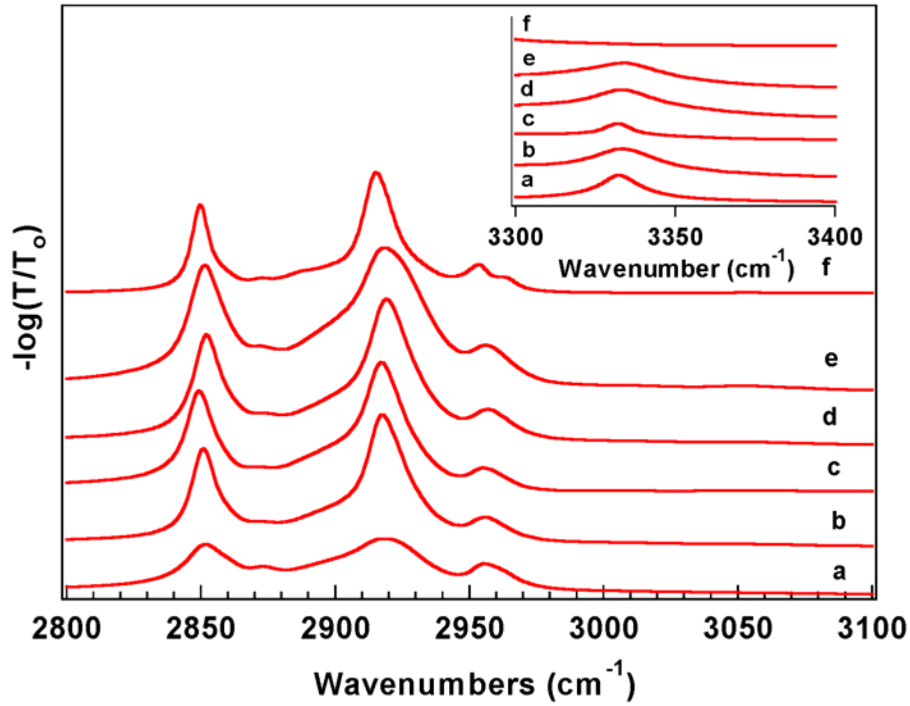

Figure 2.1. ATR-IR absorbance from 2800-3100 cm^{-1} of a) *n*-HDA b) 26 c) 41 d) 45 e) 65 and f) 90 Å CdSe-HDA QD films at room temperature. Inset: Region from 3300-3400 cm^{-1} showing size dependence of the N-H stretch.

2.3.1.1. High-Frequency Region (2800-3350 cm^{-1}). Infrared absorption data between 2800 – 3100 cm^{-1} at 298K is presented in Figure 2.1 and Table 2.1 for nano-crystalline CdSe-HDA between 26 Å and 90 Å (HDA is *n*-hexadecylamine ($NH_2(CH_2)_{15}CH_3$)). The infrared peaks between 2800 and 3100 cm^{-1} in Figure 2.1 are assigned to contributions form the ν_{CH} stretching modes (d^+, d^-) for $-CH_2$ along the polymethylene alkylamine chains and to the end-methyl groups ($-CH_3$) (r^+, r^-). Complete assignments can be made for all the QD sizes, chain lengths, and chain head-group as indicated in Tables 2.1, 2.2, and 2.5. Close inspection of the 41 Å CdSe-HDA infrared data allows assignment of the asymmetric CH stretching mode (r^- mode), at 2955 cm^{-1}.

Table 2.1: Identification and Assignment of C-H and N-H Stretching Modes (cm^{-1}) as a Function of CdSe Quantum Dot Size (Å) at 298 K

vibrational modes[a]	*n*-HDA	26	41	55	65	90
asym NH_2 str	3332.1	3333.3	3331.9	3333.0	3333.6	-
asym CH_3 str (op); r_a^-	2961.7	2962.0 (w, sh)	2960.9 (sh)	-	2962.8 (vw, sh)	2960.3
asym CH_3 str (ip); r_b^-	2954.5	2955.2	2954.6	2955.7	2955.5	2955.5
antisym CH_2 str; d_α^-	2922.6	2924.0 (w, sh)	2930.2 (sh)	2924.5 (sh)	2931.3	2922.6
antisym CH_2 str; d^-	2914.9	2915.2	2916.0	2915.5	2914.0	2916.0
sym CH_3 str; r^+	2873.6	2872.9	2871.5	2873.5	2872.9	2873.8
sym CH2 str; d_α^+	2860.9	2861.8	2857.3	2861.0	2859.6	-
sym CH_2 str; d^+	2851.1	2850.2	2848.8	2850.2	2848.2	2851.0

[a] str, stretching; sym, symmetric; ip, in-plane; op, out-of-plane; w, weak; vw, very weak; sh, shoulder.

Table 2.2: Identification and Assignment of C-H and N-H Stretching Modes (cm^{-1}) as a Function of Alkylamine ($NH_2(CH_2)_nCH_3$) Chain Length at 298 K

vibrational modes[a]	*n* = 15 (41 Å)	*n* = 7 (55 Å)
asym NH_2 str	3331.9	3333.0
asym CH_3 str (op); r_a^-	2960.9 (sh)	2963.0 (w, sh)
asym CH_3 str (ip); r_b^-	2954.6	2956.2
antisym CH_2 str; d_α^-	2930.2 (sh)	-
antisym CH_2 str; d^-	2916.0	2923.8
sym CH_3 str; r^+	2871.5	2872.8
sym CH2 str; d_α^+	2857.3	-
sym CH_2 str; d^+	2848.8	2854.0

[a] str, stretching; sym, symmetric; ip, in-plane; op, out-of-plane; w, weak; sh, shoulder. [b] CdSe QD size.

Table 2.3: Identification and Assignment of C-H and N-H Stretching Modes (cm^{-1}) as a Function of Chain Head-Group at 298 K

vibrational modes[a]	HDA[b] (41 Å)[e]	HDT[c] (45 Å)	TOP/O[d] (45 Å)
asym NH_2 str	3331.9	-	-
asym CH_3 str (op); r_a^-	2960.9 (sh)	-	2963.4
asym CH_3 str (ip); r_b^-	2954.6	2956.1	2955.3
antisym CH_2 str; d_α^-	2930.2 (sh)	2930.6	-
antisym CH_2 str; d^-	2916.0	2918.8	2922.1
sym CH_3 str; r^+	2871.5	2873.3	2873.2
sym CH2 str; d_α^+	2857.3	2861.3	-
sym CH_2 str; d^+	2848.8	2850.6	2852.0

[a] str, stretching; sym, symmetric; ip, in-plane; op, out-of-plane; sh, shoulder. [b] HDA = hexadecylamine. [c] HDT = hexadecanethiol. [d] TOP/O = trioctylphosphine / oxide. [e] CdSe QD size

Using second derivatives, the r^- can be deconvoluted into contributions from the r_b^- and r_a^- modes at 2955 and 2960 cm^{-1}, respectively. The splitting of the asymmetric peak arises from the loss of C_3 symmetry of the alkylamine chain when it is covalently bonded to the QD surface, in analogy to what is seen in SAMs.[25] The small degree of splitting for the r^- modes suggests hindered chain rotations about the long axis of the alkylamine ligand. The symmetric CH stretching mode (r^+) for 41 Å CdSe-HDA can be assigned at 2872 cm^{-1}. It is interesting to note that there is no evidence for the Fermi resonance band, which is observed for SAMs. This may possibly arise from symmetry breaking along the chain due to chain tilt angles on the surface. Assignment of the -CH_2 ν_{CH} symmetric (d^+) and antisymmetric (d^-) stretching modes in the infrared absorption spectrum for the 41 Å CdSe-HDA, occurs at 2848 and

2916 cm^{-1}, respectively. Second derivative spectra reveal two additional peaks occurring at 2930 and 2857 cm^{-1} which can be assigned to the symmetric and antisymmetric CH stretching modes of the CH_2 group closest to the head group (i.e. α-CH_2).[26] In the inset in Figure 2.1, the band at ~3331 cm^{-1} most likely arises from the N-H asymmetric stretch. The shift in the N-H mode from ~3370 cm^{-1}, typically observed in primary amines, is consistent with the weakening of the N-H bond upon covalent bonding to the QD surface. Shifts up to 60 cm^{-1} for the N-H mode have been observed when complexed to inorganic coordination compounds.[27] It is interesting to note in Figure 2.1 that at the largest QD sizes, there is a loss of ν_{NH}, possibly due to alkylamine/ surface interactions, implying that, in this size regime, the Cd-N molecular interaction changes.

2.3.1.2. Low-Frequency Region (600-1800 cm^{-1}). Figures 2.2a and 2.2b show infrared absorbance spectra in the low-frequency region for CdSe-HDA. The spectra are presented as a function of QD size, ranging from 26 Å to 90 Å, with *n*-HDA as a reference. The assignments are listed in Table 2.4. Complete assignments for all QD sizes, chain lengths, and chain head-group are presented in Tables 2.4, 2.5, and 2.6.

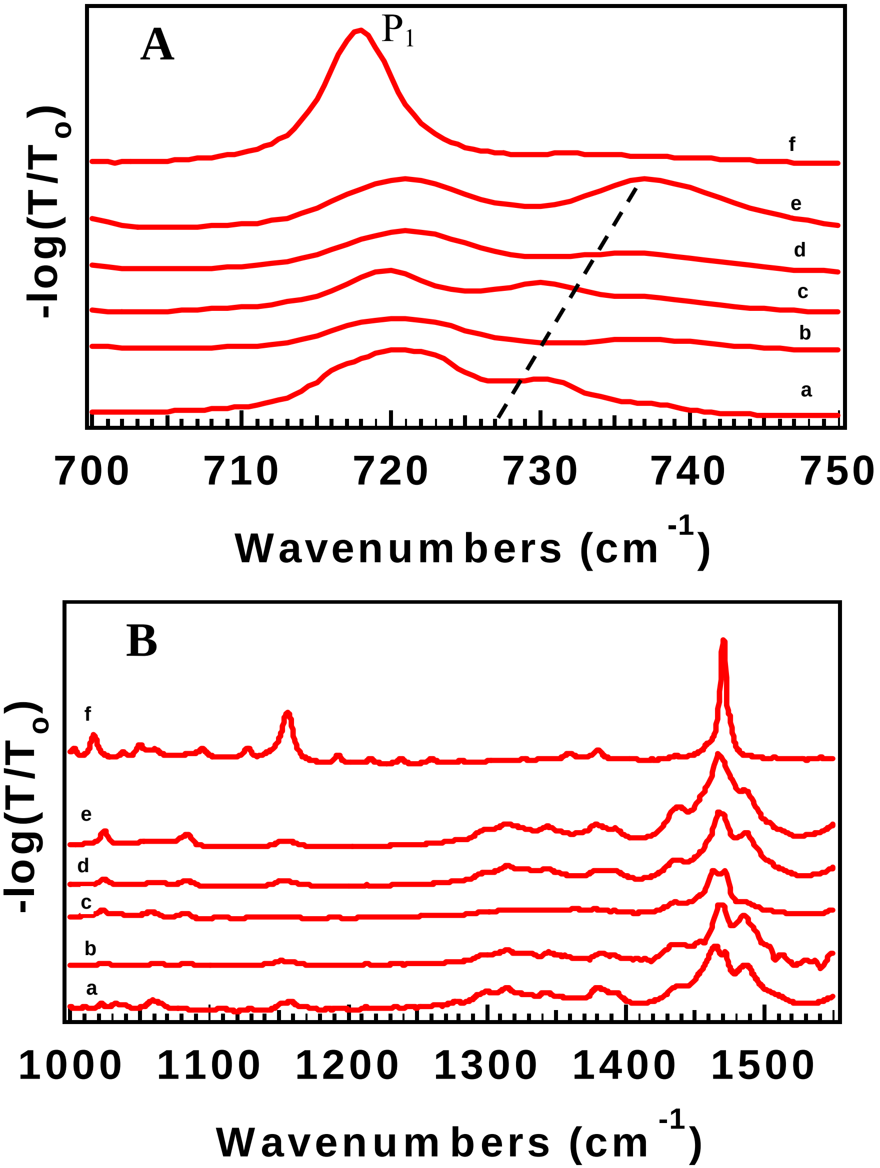

Figure 2.2. ATR-IR absorbance from (A) 700-750 cm^{-1} and (B) 1000-1550 cm^{-1} of a) *n*-HDA b) 26 c) 41 d) 45 e) 65 and f) 90 Å CdSe-HDA QD films at 298K.

The characteristic modes between 1450-1475 cm^{-1} are related to the –

CH_2 and $-CH_3$ deformation modes. For a 41 Å CdSe QD, there are two contributions to these peaks. The strong band at ~1463 cm^{-1} is from the in plane $-CH_3$ asymmetric deformation (α_{ip}) and the peak at ~1471 cm^{-1} is due to the CH_2 deformation (δ). The peak at ~1378 cm^{-1} is assigned to the $-CH_3$ symmetric deformation (U). It is followed by a series of peaks between 1170-1350 cm^{-1} which are assigned to the progression series originating from the wagging (W_x) and twisting (T_x) vibrations of the methylene groups (see Fig. 2.3). The lack of the characteristic infrared signature for the end-gauche defect (~1341 cm^{-1}) in QDs suggests an all-trans conformation in the alkylamine chains on the QD surface. The progression of C-C-C skeletal vibrational (S_x)

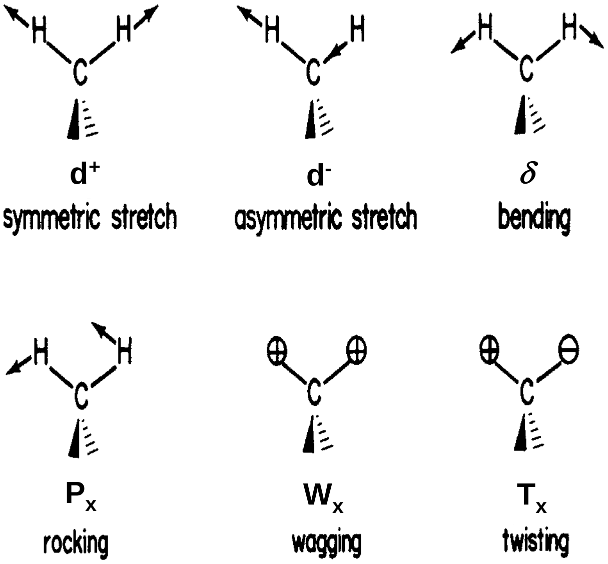

Figure 2.3. Illustration of the methylene stretches observed on a long chain alkane. Adapted from Harris and Bertolucci, *Symmetry and Spectroscopy*, Dover: New York (1978).

modes is observed between 1020-1150 cm^{-1}, followed by a set of bands between 710-1000 cm^{-1} arising from the CH_2 rocking modes (P_x). No N-H wagging is evident in this region due to the small cross section with respect to the C-H skeletal modes in this region. The peak at ~720 cm^{-1} is attributed to the head-band (P_1) of the $–CH_2$ asymmetric rocking mode progression series. This mode is sensitive to the packing of the chains on the surface of the QD and is modulated by the QD size as indicated in Table 2.4. The 41 Å QD splits into two peaks, indicative of orthorhombic packing, while the other size QDs exhibit a single 720 cm^{-1} peak consistent with monoclinic or triclinic packing. The set of peaks from 650-700 cm^{-1} occurs in all spectra and is assigned to N-H wagging modes.

2.3.2. Temperature Dependent Infrared Data

2.3.2.1. High-Frequency Region (2800-3350 cm^{-1}). Temperature dependent ATR-IR spectra between 2700-3100 cm^{-1} on 41 Å CdSe-HDA QDis shown in Figure 2.4a. The d^+ and d^- modes shift to higher energy with increasing temperature indicating an increase in gauche defect population arising from the onset of chain melting. Such behavior is observed in crystalline alkanes and self-assembled monolayer structures.[19, 28,19, 28] Upon cycling the temperature, the modes do not completely recover (Figure 2.5); however, the original position is observed for the modes after several days at

Table 2.4. Identification and Assignment of Low-Frequency Modes (720-1800 cm^{-1}) as a Function of CdSe Quantum Dot Size (Å) at 298K.

vibrational modes[a]	*n*-HDA	26	41	55	65	90
CH_2 rock; P_1	722	722	719	723	721	722
P_3	731	736	731	736	738	737
P_7	772	770	770	770	769	765
P_9	794	794	796	794	794	785
P_{11}	816	816	816	818	816	820
P_{13}	859	862	859	862	862	859
P_{CH3}	893	889	893	896	900	892
P_x	927	940	927	929	939	935
P_x	973	966	966	969	964	967
P_x	995	-	995	995	998	1001
C-C-C skeletal; S_x	1024	1024	1022	1024	1024	1024
S_x	1061	1063	1059	1063	1066	1069
S_x	1083	1084	1082	1083	1083	1083
S_x	1129	1128	1131	1127	1121	1123
S_x	1153	1151	1153	1153	1155	1155
CH_2 Wag; W_x	1174	1173	-	1185	1173	1171
CH_2 Twist; T_x	1192	1194	1190	1192	1194	1194
W_x	1213	1212	1213	1213	1215	1217
T_x	1236	1235	1235	1237	1233	1230
W_x	1255	1255	-	1255	1255	1251
T_x	1264	1264	1264	1264	1265	1266
W_x	1279	1277	1276	1278	1280	1278
T_x	1301	1301	1301	1300	1300	1302
W_x	1315	1315	1315	1315	1315	1316
T_x	1330	1327	-	1327	1324	1329
W_x	1344	1344	1346	1344	1344	1346
CH_3 sym def, bend	1382	1381	1378	1381	1379	1381
P_1, ovt[b]	1439	1439	1437	1437	1439	1443

CH_2 def, scissor, δ	1471	1468	1463 1471	1468	1467	1468

[a] def, deformation; ovt, overtone; sym, symmetric; ip, in-plane [b] first overtone of the fundamental P_1 should occur ~ 1440 cm-1

Table 2.5. Identification and Assignment of Low-Frequency Modes (720-1800 cm^{-1}) as a Function of Alkylamine ($NH_2(CH_2)_nCH_3$) Chain Length at 298 K

vibrational modes[a]	$n = 15$ (41 Å)[b]	$n = 7$ (55 Å)
CH_2 rock; P_1	719	723
P_3	731	738
P_7	770	764
P_9	796	-
P_{11}	816	804
P_{13}	859	836
P_{CH3}	893	889
P_x	927	945
P_x	966	970
P_x	995	-
C-C-C skeletal; S_x	1022	1024
S_x	1059	1055
S_x	1082	1083
S_x	1131	-
S_x	1153	1148
CH_2 Wag; W_x	-	-
CH_2 Twist; T_x	1190	1183
W_x	1213	1216
T_x	1235	1233
W_x	-	1256
T_x	1264	1268
W_x	1276	-
T_x	1301	1302
W_x	1315	-
T_x	-	1325
W_x	1346	1344
CH_3 sym def, bend	1378	1378
P_1 ovt[c]	1437	1438
CH_2 def, scissor, δ	1463 1471	1475

[a] def, deformation; ovt, overtone; sym, symmetric; ip, in-plane. [b] CdSe QD size [c] first overtone of the fundamental P_1 should occur ~ 1440 cm-1

Table 2.6. Identification and Assignment of Low-Frequency Modes (720-1800 cm^{-1}) as a Function of Chain Head-Group at 298 K

vibrational modes[a]	HDA[b] (41 Å)[e]	HDT[c] (45 Å)	TOP/O[d] (45 Å)
$(C\text{-}S)_G$ str	-	635	-
CH_2 rock; P_1	719	721	722
P_3	731	736	737
P_7	770	763	765
P_9	796	802	808
P_{11}	816	823	-
P_{13}	859	851	844
P_{CH3}	893	889	898
P_x	927	931	932
P_x	966	963	958
P_x	995	985	977
C-C-C skeletal; S_x	1022	1024	1025
S_x	1059	1067	1062
S_x	1082	1084	1083
S_x	1131	1125	-
S_x	1153	1154	-
P=O str	-	-	1155
CH_2 Twist; T_x	1190	1187	1197
CH_2 Wag; W_x	1213	1207	-
T_x	1235	1226	1223
W_x	-	1247	1240
T_x	1264	1266	1264
W_x	1276	1281	1275
T_x	1301	1300	1302
W_x	1315	1315	1322
T_x	-	-	-
W_x	1346	1343	1342
CH_3 sym def, bend	1378	1377	1378
P_1 ovt?	1437	1436	-
CH_2 def, scissor	1463	1467	1466
	1471	-	-

[a] def, deformation; ovt, overtone; G, gauche; sym, symmetric; ip, in-plane. [b] HDA = hexadecylamine. [c] HDT = hexadecanethiol. [d] TOP/O = trioctylphosphine/ oxide. [e] CdSe QD size

RT, suggesting a slow kinetic recovery. Similar data is obtained for other sized QDs.

2.3.2.2. Low-Frequency Region (600-1800 cm^{-1}). Temperature dependent

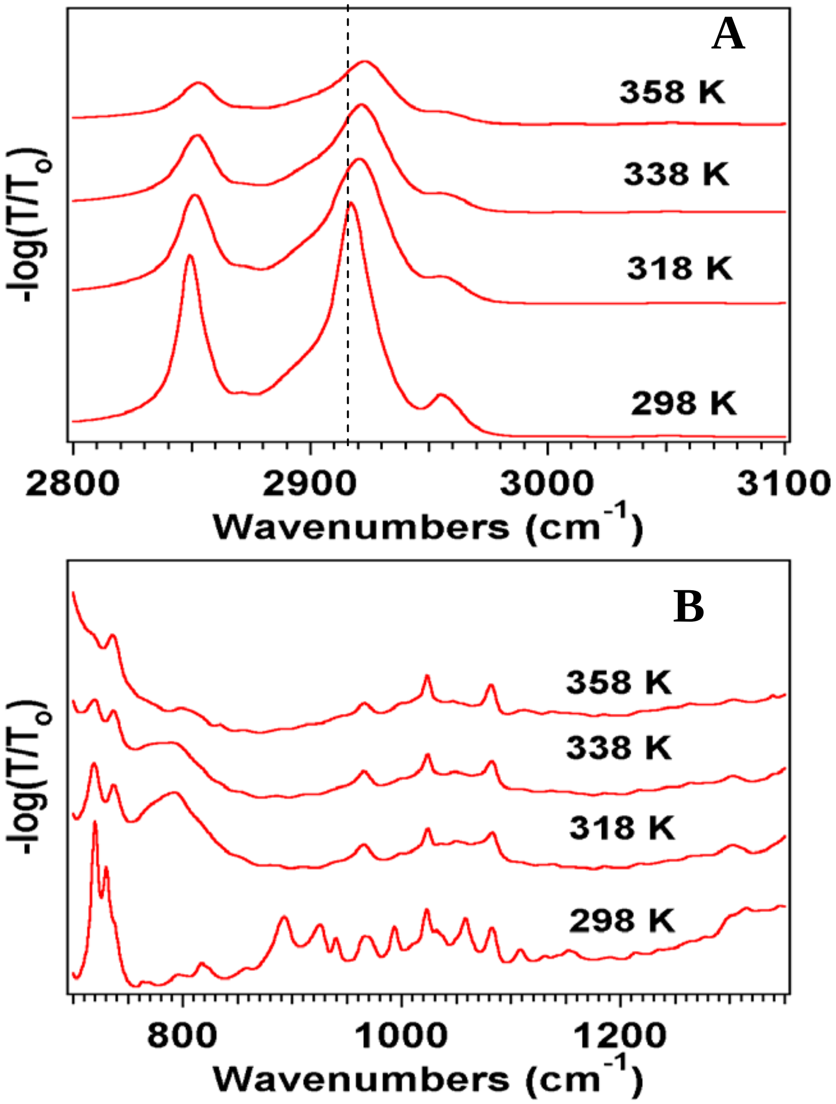

Figure 2.4. ATR-IR absorbance from (A) 2800-3100 cm^{-1} and (B) 700-1350 cm^{-1} as a function of temperature for 41 Å CdSe-HDA QD films.

ATR-IR spectra between 700-1350 cm^{-1} on a 41 Å CdSe-HDA QD is shown in Figure 2.4b. Upon heating, the P_1 (~ 720 cm^{-1}) peak loses intensity. The progression modes (P_x, S_x, W_x, T_x) lose intensity with increased temperature indicative of increased conformational disorder. At the highest temperatures (~368 K), the appearance of the 1341 cm^{-1} mode indicates the presence of gauche defects in the chains consistent with the observation of an increase in gauche conformer population for the higher frequency IR data in section 2.3.2.1.

2.3.3. Differential Scanning Calorimetry. All DSC traces show reversible endothermic transitions for the various CdSe-HDA QD materials (Figure 2.6). The enthalpic data represent average values for multiple runs on several samples and is presented in Table 2.7. [29] The low temperature (T_m)

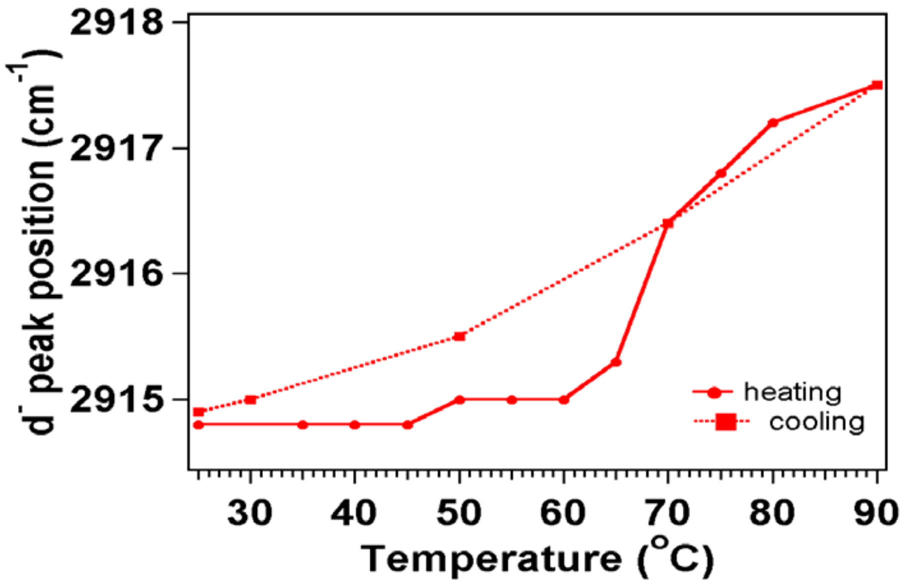

Figure 2.5. Thermotropic behavior of the d^- mode for a 90 Å CdSe-HDA QD film.

endothermic peak at 315 K, assigned to the melting (ΔH_m) of the alkylamine chain, is observed for all QD sizes and the free chain. For the larger QDs a second endothermic transition (T_c) is observed between 343 – 363 K which is attributed to a chain collapse transition (*vide infra*), ΔH_c. There may be evidence in the 80 Å QD that the second high energy transition undergoes differing phase behavior resulting in an apparent peak splitting in the endotherm. For a self-consistent data analysis, however, this peak was modeled as only one transition. Further experiments are needed to clarify this apparent anomaly. Similar data was seen for QDs passivated with

Table 2.7. Chain melt (ΔH_m) and chain collapse (ΔH_c) enthalpies as a function of CdSe QD size (Å)

CdSe-HDA[a]		
Size (Å)	ΔH_m[b] (kJ mol^{-1})	ΔH_c (kJ mol^{-1})
0 (*n*-HDA)	8.6 ± 0.5	-
26	8.0	-
40	5.7	-
45	2.6	21.3
80	4.2	4.1
90	5.4	12.3

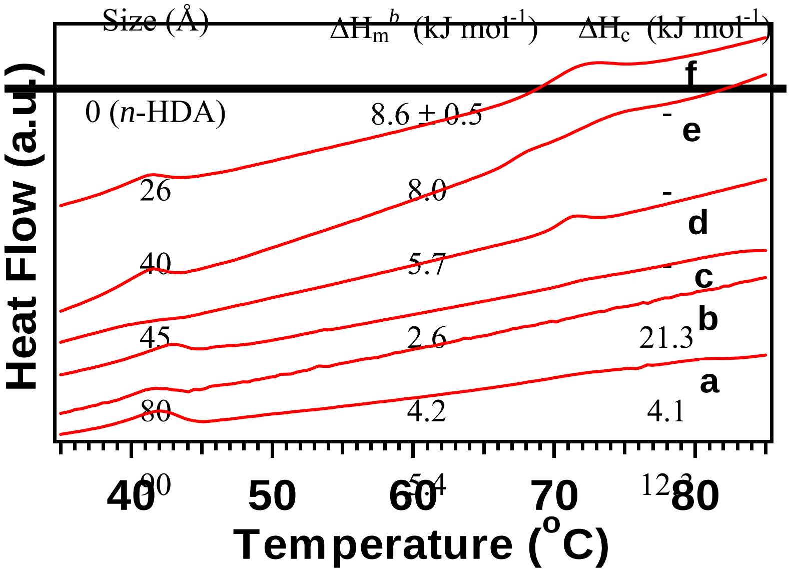

Figure 2.6. DSC endotherms for a) *n*-HDA and b) 28 c) 40 d) 45 e) 80 f) 90 Å CdSe-HDA QD films.

shorter alkylamine (i.e. OA – octylamine) substituents. A thermodynamic trend between ΔH_m and QD size is observed and represented in Figure 2.7.

2.3.4. Structural Analysis. Temperature dependent SAXS data is presented in Figure 2.8. The small angle peaks, due to the superlattice of the QDs, lose

^{a}hexadecylamine ^{b} ΔH values reported per alkyl chain

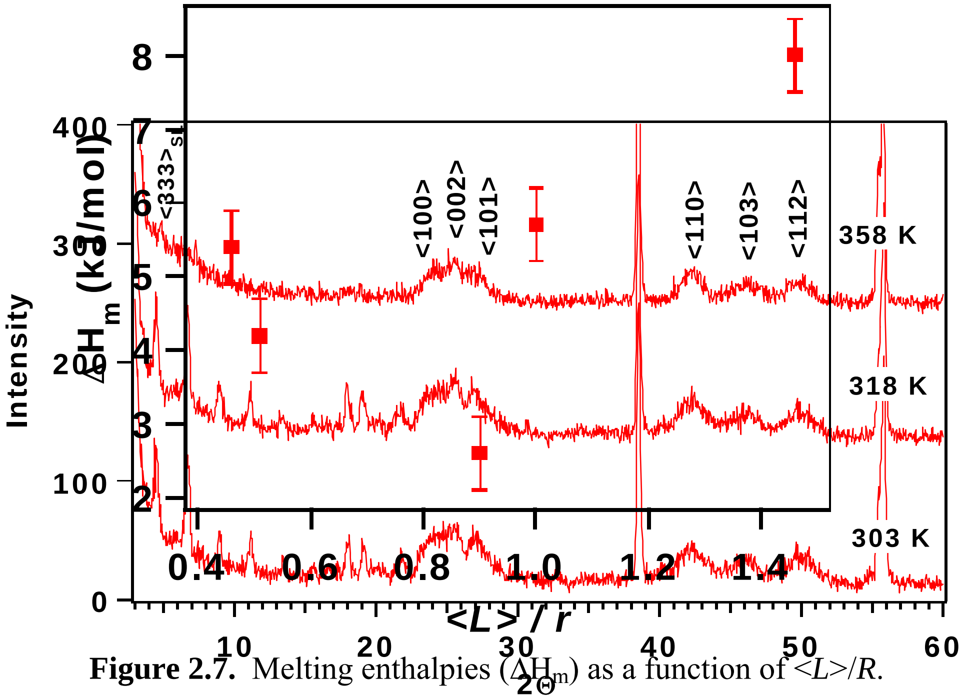

Figure 2.7. Melting enthalpies (ΔH_m) as a function of <*L*>/*R*.

Figure 2.8. Temperature dependent powder XRD for a 62 Å CdSe-HDA QD solid.

all intensity between 318 – 358 K. The crystallographic reflections of the CdSe QD are not affected by temperature, showing no structural transformation in the temperature range studied.

Room temperature TEM analysis of evaporated films shown in Figure 2.9. Statistical analysis of the TEM pattern indicates hexagonally packed structures with separation distances of ~30 Å. This is consistent with intimate contact between the QDs and potentially interdigitation of bundles or singles chains.

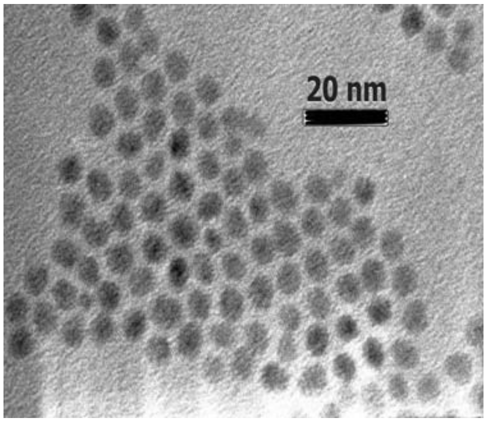

Figure 2.9. TEM image of ~55 Å CdSe-HDA self-assembled QDs.

2.4. Discussion

2.4.1. Molecular Orientation. Thermodynamic stabilization of the organic passivating layer on QDs arises from the molecular level interactions of the chain packing at the organic/inorganic interface. Molecular packing can be described in terms of either chain-chain interactions providing crystallinity in the conformation, or in terms of the surface packing density, which describes the packing lattice for the chains on the surface. Molecular packing is governed by a competition between the head group interactions (σ_{thiol} and A_{hs}, A_{tr}, A_{hh}), and the chain-chain packing interactions (δ_{SAM} and A_{att}, A_{conf}) (Figure 2.10). Such a model is analogous to micelle stabilization, self-assembled monolayers (SAMs), and Langmuir-Blodgett (L-B) structures, where a competition between entropic terms and enthalpic terms dictate the ratio of gauche conformers to all-trans conformers observed for the individual chains. In SAMs, a constrained all-trans geometry for the amphiphilic surface molecule is observed with increasing chain length, which is in the regime where enthalpic contributions dominate chain-packing thermodynamics.[30-33, 41] As the density of packing decreases, there is an increase in entropic contributions to chain ordering at the molecular interface arising from an increase in rotational degrees of freedom. On a QD surface, surface curvature effects on packing densities complicate the competition between enthalpic and entropic terms. An all-trans conformation for the chains should be observed in cases where the enthalpic terms dominate packing, particularly in the regime where chain length can compensate for surface curvature. In other words, larger nanoparticles would exhibit an effective lower passivation density based on surface de-stabilization resulting from the decrease of thermodynamic contribution from the headgroup-binding event. Smaller nanoparticles would have competing contributions from headgroup and chain-chain interactions as well as contributions from gauche (defect) conformers to maximize packing densities. Such effects have

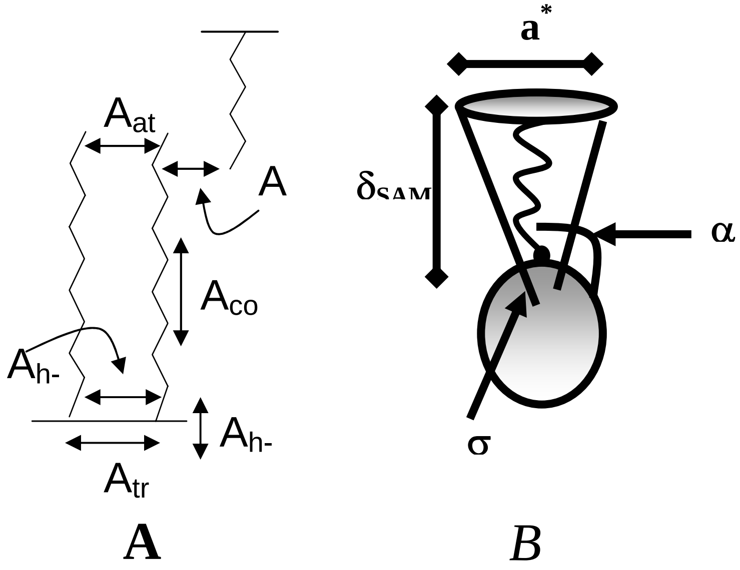

Figure 2.10. Schematic illustration of factors directing chain packing thermodynamics: (A) Free energy contributions to intra-, inter-, and neighboring van der Waals forces where A_{tr} is the translational entropy of the chains, A_{conf} is the conformational free energy of the chains, A_{att} is the attractive interaction between the chains, $A_{h\text{-}h}$ is the headgroup-headgroup interactions, $A_{h\text{-}s}$ is the headgroup-surface interactions, A_n is a term that arises from any van der Waals interactions between chains of different dots (i.e. interdigitated chains). (B) Factors arising from the reduced dimensionality of QD surfaces where σ is the area-per-headgroup, a^* is the effective area-per-headgroup, α is the chain tilt, and δ_{SAM} is the passivant molecular density.

been observed for Au nanoparticles where the contribution of surface curvature leads to enhanced contributions of stabilization arising from head-group interaction with the surface (A_{hs}) as the enthalpic stabilization from chain – chain interactions (A_{conf}) decrease with a decreases in Au particle radii.[34, 35]

In an evaporatively assembled film of QDs, there are two limiting regimes for stabilization of the passivant layer:

a) single dot effects where the chain interactions are governed by A_{hs} and A_{att},

b) dot-dot interactions where chain interactions arising from interdigitation and bundling contribute to the thermodynamic packing stability.

Within these limiting cases, the interaction of the chains and the surface will be modulated by the ratio of the passivant chain length and the QD radius. Analysis of ATR-IR data in CdSe-HDA QD samples for the d^+, d^- and r^+, r^- modes (~3000 cm^{-1}) and the gauche defect region (1300-1400 cm^{-1}) provides insight into the packing conformation of the alkylamine chains assembled at the QD/ solution interface. For the ATR-IR data in Table 2.1 the d^+ and d^- modes are observed between 2848-2850 and 2914-2916 cm^{-1} consistent with an assignment of a predominately all-trans packing arrangement at the surface of the CdSe QDs. As the QD size increases, a shift in the 2850 cm^{-1} mode to lower frequency and the 2915 cm^{-1} mode indicates an enhanced degree of crystallinity in the packing conformation. This is further supported by the increased contribution of T_x and W_x progressions for the 90 Å CdSe-HDA sample. For the HDA passivated materials, the degree of crystallinity is higher than in the octylamine or solvated samples as seen in the shift of the d^+ and d^- modes and loss of the twist and wag progressions, due to an increase in gauche conformer population in the 1300 cm^{-1} region.[25] Comparison of the vibrational data for solutions and films of QDs suggests these nano-assemblies can be readily described in terms of single dot interactions for the chain-chain packing and governed largely by the surface curvature and length of the passivating layer. The interdigitation or bundling of the chains may exist in these systems with evidence from TEM and SAXS data (Fig. 2.8 and 2.9), but may not contribute significantly to the phase behavior of the quantum dots based upon single particle interactions.

The influence of surface curvature is apparent in the lattice packing of the individual amphiphilic molecules. As the surface curvature increases, the density of packing appears to decrease, resulting in an increase in the degrees of rotational freedom. Freedom of rotation in the chain gives rise to two observable packing motifs in the CdSe lattice: hexagonal, and orthorhombic (commonly referred to as herringbone). The 1467 and 720 cm^{-1} chain packing modes (P_1 and δ) provide direct insight into the packing motiff on the surface of the QDs. A single peak at ~1470 cm^{-1} and 720 cm^{-1} occurs for all QD sizes except for the 41 Å QD and *n*-HDA implying that the unit cell is a hexagonal cell arising from rotational freedom in the chains. This packing motif is observed in SAMs and has been postulated in Au nanoparticles. The orthorhombic packing of the *n*-HDA is similar to the low-temperature phases seen in crystalline *n*-alkanes.[36] Surprisingly, for the 41 Å QD, two peaks (~1463 and 1471 cm^{-1} and ~ 719 and ~ 730 cm^{-1}) *of comparable intensity* are observed which indicate the chains are in an orthorhombic arrangement. The observation of orthorhombic packing on the highly constrained 41 Å CdSe may arise from enhanced head-group surface interactions, or surface reconstruction leading to tighter chain packing on the surface of the small QD.

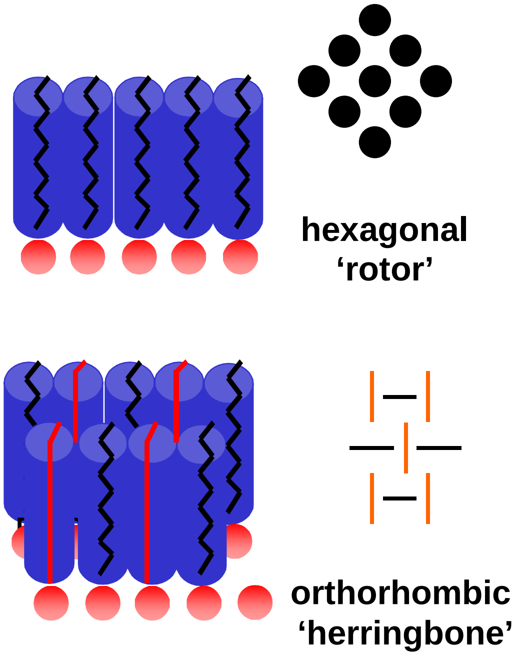

Figure 2.11. Illustration of orthorhombic and hexagonal packing of alkane chains.

The assigned packing motifs are further supported by the thermal data predictions for the orthorhombic and hexagonal lattice (see Fig. 2.11).[37] For hexagonal packing a low-energy melting transition is observed, while QDs with an orthorhombic arrangement undergo two phase transitions:

a) an orthorhombic to hexagonal transition

b) a chain melt transition.

Figure 2.4b shows temperature dependent ATR-IR data that indicates that for the 41 Å QD loss of the 720 and 1470 cm^{-1} mode splitting occurs immediately upon heating due to a first order phase transition from orthorhombic to hexagonal. The lack of an observable transition in the DSC probably arises from the fact that the orthorhombic to hexagonal transitions occur at temperatures only a few degrees less than the melt transitions.[36, 38] The differences in the packing geometries can be understood in terms of packing densities. The two-step constrained melting in the larger QDs suggests a greater packing density of the chains on the QD surface. This suggests the headgroup/ surface interactions become negligible when the particle radius exceeds the chain length.

2.4.2. Molecular Tilt. As the surface curvature on a QD increases, the packing density decrease can be compensated by the tilt angle of the amphiphilic molecule. As observed in SAMs, an increase in tilt angle allows enthalpic stabilization of the surface as the entropic contributions are decreased for the total packing motif. For CdSe QDs with a C_{16} chain, all QD sizes below 90 Å show a stretch at ~ 3330 cm^{-1} (inset Figure 2.1) which is assigned to the asymmetric NH_2 stretch. The integrated intensity for ν_{NH} decreases with increasing size until the particle reaches 90 Å and the mode loses complete intensity. This can be attributed to a chain tilt on the surface of the QD as illustrated in Figure 2.12. As the chain takes a configuration resembling that in figure 2.12a, surface selection rules dictate a screening of vibrational modes parallel to the surface. This implies μ_{NH2} is beginning to approach zero, hence the loss in intensity of the mode. Nuzzo and co-workers have made similar arguments with alkanethiols absorbed on ZnSe semiconductor surfaces.[39] Coupled with this decrease, a loss in the integrated intensity of ~20% is seen for the asymmetric CH_2 stretch (d^-) going from 26 to 90 Å, which is consistent with an increase in chain tilt for the largest QD implying that $\mu_{CH2} \rightarrow 0$. It is important to note that the cross section for methylene absorption is much higher than N-H absorption, explaining the difference in spectral behavior. Corroborating this assignment, the splitting of the r^- mode into the in- and out-of-plane stretches shows a breaking of symmetry that can arise from tilting on the QD surface. It has also been shown that alkyl chains tilt to decrease their separation and increase their intermolecular van der Waals forces.[14, 16] This behavior would result in better amphiphillic packing and increased crystallinity in the chains.

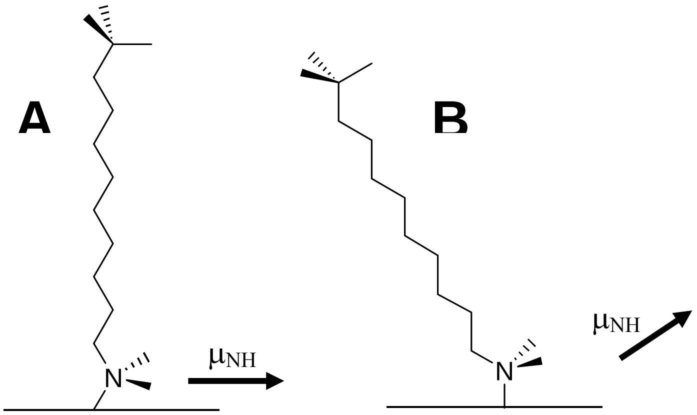

Figure 2.12. Schematic illustrations showing (A) chain tilt to maximize van der Waals forces and (B) possible chain orientation on small particles where packing density and constraints are less. Note the direction of the transition dipole moments.

2.4.3. Thermodynamic Regimes. In the analysis of Au nanoparticles, it was demonstrated that strong surface/ headgroup dependence was observed for nanocrystals in which the passivant length (<*L*>) was smaller than the radius of the particle (R).[14, 16] This suggests that there exists some thermodynamic minimum where the passivant free energy is minimized, and can be modeled in terms of three limiting cases:

a) Case 1: $<L>/R < 1$ (2-d model – SAM model) QD surface appears flat with respect to the passivant.

b) Case 2: $<L>/R > 1$ (3-d model) QD surface curvature perturbs the molecular structure of the passivant.

c) Case 3: $<L>/R \sim 1$ (special case – a very stable packing motif is predicted).

The three cases have different thermodynamic terms dominating packing which in turn dominates chain tilt, chain melt, chain collapse and chain surface interactions. For $<L>/R < 1$ and $<L>/R > 1$, either chain energy or chain entropy dictates the conformational free energy.[14, 40,14, 40] It is predicted that when $<L>/R \sim 1$, the conformational free energy of the chains will be minimized. Murray, et al, has suggested similar models for Au nanocrystals.[14] Thermal data coupled to IR analysis allow direct observation of these regimes. Thermodynamic melting transitions for $<L>/R > 1$ is predicted[22] to melt at the same temperature as the free amphiphilic molecule, while melting in the $<L>/R < 1$ regime is predicted to exhibit a 2-step constrained melting curve, in which initial terminal gauche densities increase due to $–CH_3$ group rotational freedom occurring at the melt transition of the alkane, followed by an increase in intra-chain gauche population which can occur as high as 60 ºC above that of the free amphiphillic molecule.[20]

In case 1, where <*L*>/*r* < 1 (*r* > 41 Å), the chain packing at room temperature is similar to SAMs, with minimal surface curvature effects for these materials. The chain packing motif is hexagonal and highly crystalline with clearly resolved ($T_x + W_x$) progressions for the 90 Å CdSe material. Furthermore, chain tilting appears in the 90 Å consistent with packing at a pseudo-planar surface relative to the chain length. The chain melting on the surface exhibits two reversible phase transitions in the thermal and IR data. For the larger QD (Figure 2.11a), the r^+ mode is shifted to higher frequency upon heating, but the d^+ mode exhibits a delayed frequency shift, implying that the end-gauche and internal gauche conformers are not thermodynamically equivalent. This is reflected in large sized QD (i.e. radius is larger than chain length) *normalized* DSC endotherms where two transitions are seen, due to end-gauche conformers followed by complete chain collapse (Figure 2.13a). The first endothermic transition (T_m) occurs at ~ 315 K, with latent heats (ΔH_m) ranging between 3 (45 Å) and 5 (90 Å) kJ mol^{-1}, which substantially deviates from the free alkylamine melting transitions. A second transition (T_c) not witnessed in the free chain or <*L*>/*r* > 1 regime occurs at higher temperatures, ranging between 70 – 75 ºC (343 – 348 K), with latent heats (ΔH_c) that are highly size dependent. The trend for this size dependence may be due to packing constraints arising from chain tilt. Onset of the intra-chain gauche defects is accompanied by increased conformational disorder as evidenced by the loss of intensity from the twist and wag (T_x and W_x) progression series modes as a function of temperature. The melting progression and the small change in ΔH suggests that that the thermodynamic stabilization in these materials arises from chain-chain enthalpic contributions predominately.

For case 2, where $<L>/r > 1$ ($<L> = 20.5$ nm, QD < 41 Å) surface curvature effects give rise to hexagonal packing and a lower crystallinity for the chains on the surface of the QD, as evidenced in the IR data. The loss of packing density is compensated in these materials by a minimization of chain tilt at the surface of the QD. *Normalized* thermal data comparison between *n*-HDA and CdSe-HDA support the packing motif described above for the $l > r$ regime. For an *n*-HDA chain, there is one reversible solid-liquid phase transition corresponding to the melting of the alkyl chain. The melt is a correlated movement of all-trans chains to defect gauche states with latent heats of 8.6 kJ mol^{-1}. Upon ligation to a small CdSe particle, there still exists one reversible melting transition where the latent heats (ΔH_m) decrease, possibly due to the free energy gain from coordination of a dangling bond. The 26 and 40 Å CdSe show enthalpies of 8.0 and 5.7 kJ mol^{-1}, respectively, at ~ 42 ºC (~ 315 K). The 1-step melt represents a continuous melt of the chains above T_m due to lack of constraint arising from lattice packing. This implies a thermodynamic equivalence of the melting of the r^+ and d^- modes which is seen in the one DSC endotherm in Figure 2.13b. For $<L>/r > 1$, chain tilting decreases to accommodate the lower packing density arising from surface curvature effects which decreases the methylene packing density by an increases in the effective area-per-headgroup, allowing greater rotational degrees of freedom.[14]

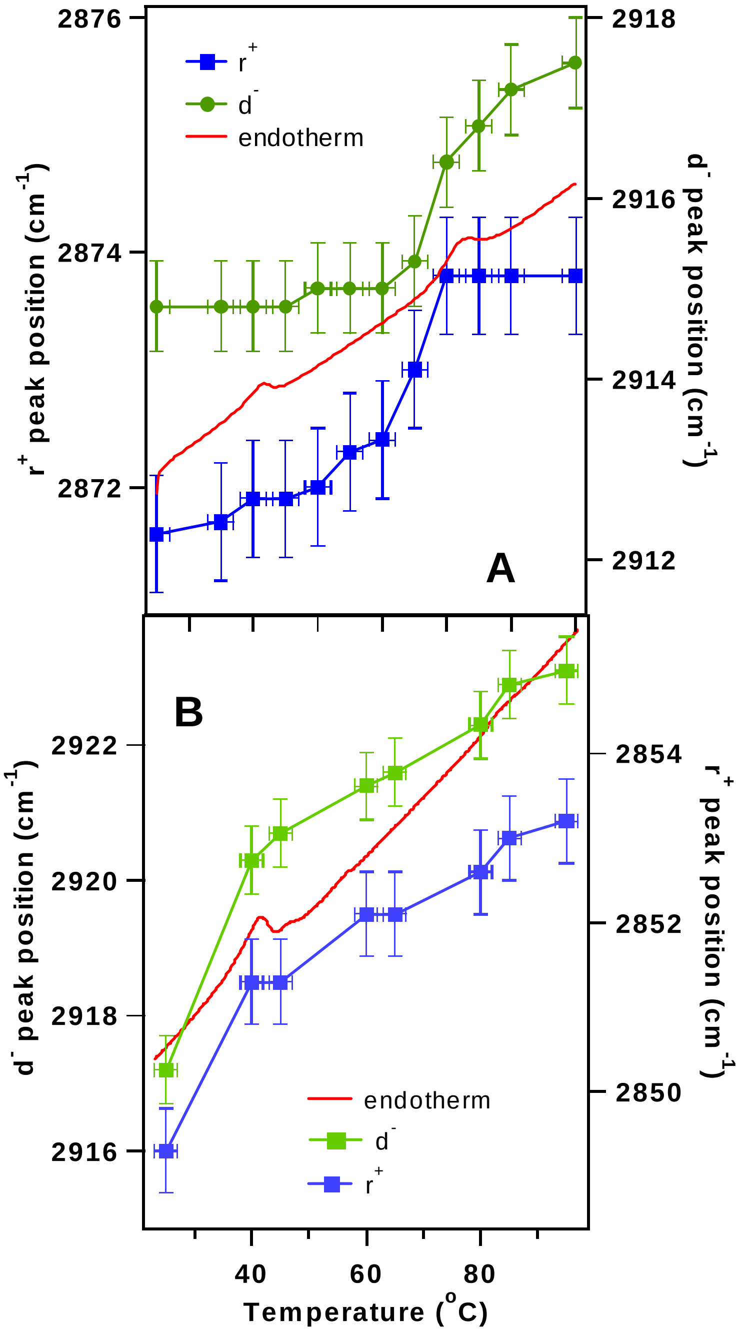

Figure 2.13. Thermotropic behavior of the d^-/ r^+ modes for (A) 90 Å and (B) 40 Å CdSe-HDA QD film. Note the strong correlation between the thermal behavior of the modes and the DSC endotherms.

For case 3, (<*L*>/*R* ~ 1) chain interactions and packing density constraints should exhibit the largest competition for control of the packing geometry at the inorganic/organic interface. In this regime, a C_{16} ligand (<*L*> ~ 20.5 Å) should produce the most stable packing for a ~ 41 Å QD. The IR data illustrates the room temperature structure is crystalline with a herringbone (orthorhombic) packing motif. This packing motif gives rise to a highly constrained surface in which the packing density is maximized, by minimization of chain tilt, consistent with a case 2 thermodynamic regime for the room temperature materials. Temperature dependent IR data on the 41 Å CdSe (Figure 2.14), illustrates a linear shift in the d^- and r^+ modes to higher frequency, implying that both end-gauche and internal gauche conformers occur simultaneously upon heating, which is reminiscent of case 2 behavior. The thermal data suggests, however, that case 3 is closely related to case 1 behavior, as evidenced from the inflection point in the melting enthalpies in Figure 2.7. This suggests changes in packing with temperature may result in a change in the appropriate thermodynamic regime as the headgroup/ surface interaction competes with the chain-chain interactions in the CdSe QD materials.

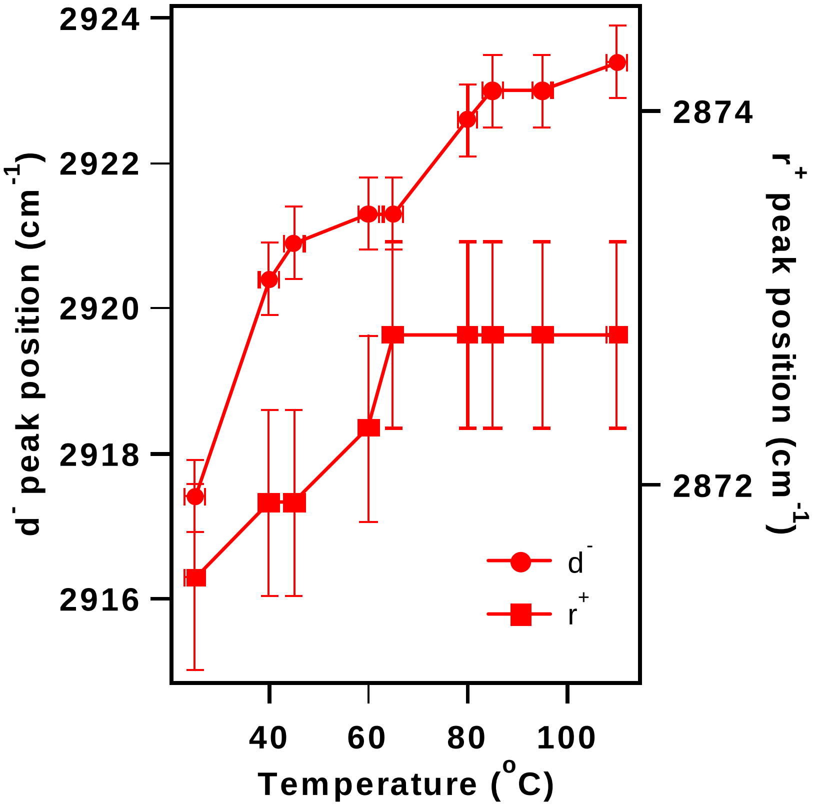

Figure 2.14. Thermotropic behavior of the d^-/ r^+ modes for a 41 Å CdSe-HDA QD film.

2.5. Conclusions. The packing of the alkylamine passivants on the surface of QD films is controlled by the competition of the free energy terms, A_{att}, A_{conf}, and A_{hs}. The dominance of these terms is influenced by surface curvature and the ratio of chain length to particle radius, giving rise to three distinct thermodynamic regimes. In the limiting cases packing is controlled by A_{hs} (surface liagtion, with independent organic moieties) or dominated by A_{att}

(chain-chain interactions). Competition between these two forces are intimately linked to the strength of the headgroup/ surface interaction (Lewis basicity of the passivant), A_{conf} (chain-length) and QD radius (surface constraints). Stabilization of the QD surface is therefore fundamentally linked to the thermodynamics of stabilization of the passivant layer. This behavior arises from the size dependent nature of the 3-dimensional constraint of the passivating layer on the QD surface.

2.6. References and Notes

1 M. L. Steigerwald and L. E. Brus, Accounts of Chemical Research **23**, 183 (1990).

2 A. P. Alivisatos, Journal of Physical Chemistry **100**, 13226 (1996).

3 C. B. Murray, D. J. Norris, and M. G. Bawendi, Journal of the American Chemical Society **115**, 8706 (1993).

4 M. A. Hines and P. GuyotSionnest, Journal of Physical Chemistry B **102**, 3655 (1998).

5 M. Kundu, A. A. Khosravi, S. K. Kulkarni, and P. Singh, Journal of Materials Science **32**, 245 (1997).

6 S. R. Cordero, P. J. Carson, R. A. Estabrook, G. F. Strouse, and S. K. Buratto, Journal of Physical Chemistry B **104**, 12137 (2000).

7 N. C. Greenham, X. G. Peng, and A. P. Alivisatos, Physical Review B-Condensed Matter **54**, 17628 (1996).

8 J. R. Sachleben, E. W. Wooten, L. Emsley, A. Pines, V. L. Colvin, and A. P. Alivisatos, Chemical Physics Letters **198**, 431 (1992).

9 J. R. Sachleben, V. Colvin, L. Emsley, E. W. Wooten, and A. P. Alivisatos, Journal of Physical Chemistry B **102**, 10117 (1998).

10 H. Noglik and W. J. Pietro, Chemistry of Materials **7**, 1333 (1995).

11 J. G. C. Veinot, M. Ginzburg, and W. J. Pietro, Chemistry of Materials **9**, 2117 (1997).

12 J. G. C. Veinot, J. Galloro, L. Pugliese, V. Bell, R. Pestrin, and W. J. Pietro, Canadian Journal of Chemistry-Revue Canadienne De Chimie **76**, 1530 (1998).

13 X. G. Peng, L. Manna, W. D. Yang, J. Wickham, E. Scher, A. Kadavanich, and A. P. Alivisatos, Nature **404**, 59 (2000).

14 M. J. Hostetler, J. J. Stokes, and R. W. Murray, Langmuir **12**, 3604 (1996).

15 M. J. Hostetler, J. E. Wingate, C. J. Zhong, J. E. Harris, R. W. Vachet, M. R. Clark, J. D. Londono, S. J. Green, J. J. Stokes, G. D. Wignall, G. L. Glish, M. D. Porter, N. D. Evans, and R. W. Murray, Langmuir **14**, 17 (1998).

16 A. Badia, L. Cuccia, L. Demers, F. Morin, and R. B. Lennox, Journal of the American Chemical Society **119**, 2682 (1997).

17 B. S. Kim, L. Avila, L. E. Brus, and I. P. Herman, Applied Physics Letters **76**, 3715 (2000).

18 T. Prozorov and A. Gedanken, Advanced Materials **10**, 532 (1998).

19 R. G. Nuzzo, E. M. Korenic, and L. H. Dubois, Journal of Chemical Physics **93**, 767 (1990).

20 J. F. Bardeau, A. N. Parikh, J. D. Beers, and B. I. Swanson, Journal of Physical Chemistry B **104**, 627 (2000).

21 G. Ungar, Journal of Physical Chemistry **87**, 689 (1983).

22 W. D. Luedtke and U. Landman, Journal of Physical Chemistry **100**, 13323 (1996).

23 S. L. Cumberland, K. M. Hanif, A. Javier, G. A. Khitrov, G. F. Strouse, S. M. Woessner, and C. S. Yun, Chemistry of Materials **14**, 1576 (2002).

24 R. G. Snyder and J. H. Schachtschneider, Spectrochimica Acta **19**, 85 (1963).

25 A. N. Parikh, S. D. Gillmor, J. D. Beers, K. M. Beardmore, R. W. Cutts, and B. I. Swanson, Journal of Physical Chemistry B **103**, 2850 (1999).

26 R. A. MacPhail, H. L. Strauss, R. G. Snyder, and C. A. Elliger, Journal of Physical Chemistry **86**, 5145 (1982).

27 J. E. B. Katari, V. L. Colvin, and A. P. Alivisatos, Journal of Physical Chemistry **98**, 4109 (1994).

28 M. Maroncelli, H. L. Strauss, and R. G. Snyder, Journal of Chemical Physics **82**, 2811 (1985).

29 The *experimental* ΔHs per gram are calculated using standard protocols. Briefly, they are obtained by extrapolating a linear baseline to the trace, and then fitting the area under the curve using this equation, $\Delta H(J/g) = \frac{-A}{Gkm}$, where G and k are constants related to the DSC instrument, A is the peak area, and m is the sample mass. The *reported* ΔHs per mole are found using the following equation, $\Delta H_{reported} = \frac{\Delta H_{\exp}}{0.22} * MW$, where $\Delta H_{\exp}$ is the raw experimental enthalpy which includes the total quantum dot mass, and MW is the molecular weight of the passivant.

30 P. E. Laibinis, G. M. Whitesides, D. L. Allara, Y. T. Tao, A. N. Parikh, and R. G. Nuzzo, Journal of the American Chemical Society **113**, 7152 (1991).

31 A. N. Parikh and D. L. Allara, Journal of Chemical Physics **96**, 927 (1992).

32 A. N. Parikh, D. L. Allara, I. B. Azouz, and F. Rondelez, Journal of Physical Chemistry **98**, 7577 (1994).

33 A. Ulman, Chemical Reviews **96**, 1533 (1996).

34 J. P. Wilcoxon, J. E. Martin, and P. Provencio, Langmuir **16**, 9912 (2000).

35 J. P. Wilcoxon, private communication .

36 J. R. Nielsen and C. E. Hathaway, Journal of Molecular Spectroscopy **10**, 366 (1963).

37 Y. S. Kim, H. L. Strauss, and R. G. Snyder, Journal of Physical Chemistry **93**, 7520 (1989).

38 H. Yoshida, Journal of Thermal Analysis and Calorimetry **57**, 679 (1999).

39 A. R. Noble-Luginbuhl and R. G. Nuzzo, Langmuir **17**, 3937 (2001).

40 S. E. Chaney and G.F. Strouse, unpublished results.

Chapter 3: Effects of Alkylamine Chain Length on the Thermal Behavior of CdSe Quantum Dot Glassy Films

This chapter has appeared in print: Meulenberg, R.W.; Bryan, S.; Yun, C.S.; Strouse, G.F. *J. Phys. Chem B* **106**, 7774-7780 (2002)

3.1. Introduction

The extent to which the stability of a semiconductor quantum dot (QD) is influenced by the area available on a QD facet for surface passivation (domain) and the nature of chain-chain (ch-ch) interactions between the passivants (dimensionality) is an important, but not well understood concept. [1-5] The organic passivant, which typically consists of an organo-phosphine, -thiol, or -amine, is believed to energetically relax defect states via coordination to partially coordinated surface atoms (dangling bonds). [6] The extent of coverage of the surface by the passivant layer, which is nanomaterial type and size dependent, increases the stability of the QD, and is believed to raise the energy of the surface trap states above the band gap, E_g. [7-9] A complete understanding of how the passivant is molecularly oriented on the surface and contributes to the thermodynamic stability of the QD can be useful in understanding the properties of these unique systems.

While the binding of organic passivants on planar self assembled monolyaer (SAM) surfaces has been well established, the energetics of a molecule adsorbing to a dimensionally restricted or curved surface is more complicated than a large single crystal. Most notably the energetics for dimensional packing of ch-ch interactions are influenced by the ability of the alkyl chains to form a stable crystalline domain on the dimensionally restricted surface. Dimensional effects occur when chain packing on a particle surface experiences an effective increase in its area per headgroup due to changes in packing density at the particle surface, i.e. splaying of the chains at the facet edge, in effect, decreasing packing densities. In nanoscale materials, observations of dimensional effects have been observed in nanocrystals passivated with alkylthiols and amines which show a strong size dependence on the melting enthalpies. [5,10] Domain effects, on the other hand, occur when the surface of a particle is too small to accommodate the kinetically favored domain size of the adsorbing molecules. The appearance of minimum domain structures of organic amphiphiles on bulk SAMs has been well documented. [11] This suggests that as the particle size decreases below a 50 Å facet, the thermodynamic energetics of chain packing may be disturbed and domain effects may be observed for passivant packing in QDs.

In this study, we analyze dimensional and domain effects in CdSe QDs capped with varying alkylamine chain lengths. Using temperature dependent vibrational spectroscopy coupled to a mean field statistical mechanical calculation, we find that passivant packing on a CdSe QD can be described in terms of both dimensional and domain models. For very small particle sizes (*r* < 22 Å), the available domain size for chain packing is too small for thermodynamic stabilization, resulting in energetically unfavorable packing. At particle sizes above 45 Å, the chain packing thermodynamics is highly dependent on the ratio of the chain length (<*L*>) to the particle radius, *r*. We find a thermodynamic minimum for chain packing when <*L*>/*r* ~ 1.0 when *r* > 44 Å.

3.2. Experimental

3.2.1. Materials. CdSe QDs were synthesized by a modification of standard lyothermal methods using *n*-hexadecylamine (HDA) as the growth solvent.[12] Crystallinity and size dispersity (~5-6 %) of the materials are monitored by UV-Vis absorption, pXRD, and TEM analysis. $C_{20}H_{43}N$ ligand was synthesized from the corresponding bromide via the Gabriel synthesis. Briefly, the C_{20} alkylamine is synthesized via a nucleophillic attack of potassium phthalimide on the corresponding alkylbromide to obtain the N-alkyl phthalimide then subsequently deprotected with hydrazine to afford the desired product.

3.2.2. Attenuated Total Reflection (ATR) FTIR Spectroscopy. QD samples were dispersed in hexane, deposited on a 4 X 80 mm ZnSe 45º HATR plate (Pike Technologies), and allowed to slowly evaporate. Temperature dependent ATR-FTIR data were collected on a Perkin-Elmer Spectrum GX system from 650-4000 cm^{-1} with a resolution of 2 cm^{-1}. Temperature control between 25-100 ºC (± 1 ºC) was achieved using a manual temperature control (Pike Technologies) coupled to the HATR plate.

3.3. Theory. The nature of packing for organic amphiphilic molecules on a surface is dependent on the interplay of the chain-chain (ch-ch) and the headgroup-surface interactions. Calculations of the free energy of the amphiphilic passivant layer on the surfaces of QDs provides insight into molecular structure, as well as potentially the chemical stability of the passivating layer on the QD surface. The thermodynamic energy for QD passivation by a long chain organic molecule can be described theoretically by adapting a micellar model based on a mean field statistical mechanical approach first developed by Szleifer, Ben-Shaul, and Gelbart.[13-15] The configurational free energy per chain on a QD surface can be described as,

$$f_c = \sum_{\alpha} P(\alpha)\varepsilon(\alpha) + kT\sum_{\alpha} P(\alpha)\ln P(\alpha) \qquad (3\text{-}1)$$

where $P(\alpha)$ is the probability distribution of chain conformations and $\varepsilon(\alpha) = n_g(\alpha)e_g$, where $n_g(\alpha)$ is the number of gauche bonds in chain configuration α, and e_g is the energy of a gauche conformer (~ 500 cal mol^{-1}).

The nanoparticle shape is best approximated by assuming a faceted particle shaped as a hexagon, however, when performing the free energy calculations, we "roll-out" the facet to form a sphere with a radius, *r*. This allows us to calculate the *average* free energy per chain without accounting for difference arising form edge or vertex sites, which will have a higher free energy contribution than the table chains. This assumption produces an average value for the free energy which for larger dots (> 40 Å) provides and adequate representation of the surface. The calculation was performed by assuming closest packing of the chains and fixing the chain footprint (fixed by

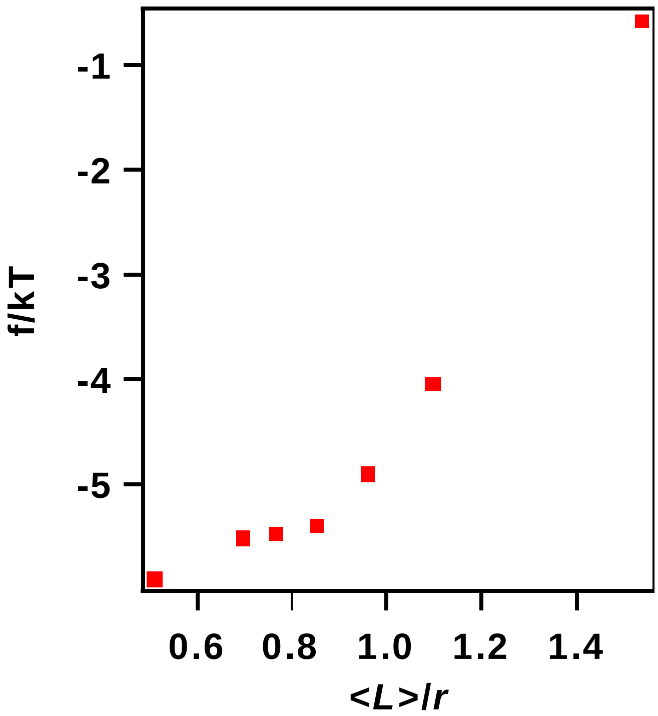

Figure 3.1. The calculated free energy, f_c, with the phenomenological headgroup free energy, f_h, added to give the total free energy f_t.

the area-per-headgroup, ~20 Å^2) causing the number of chains to scale as r^2. In general, the approximate unit cell lattice parameter of a crystal of alkane chains is ~ 5.0 Å, [16] which is close to the Cd-Cd spacing in the wurtzite lattice (~ 4.3 Å). [17] The differences in site occupation influences the chain tilt which is accounted for by allowing the chains to expand or compress to minimize their free energy. The similarity of the chain and lattice unit cells allows the assumption that the alkyl chains are arranged in a near (1×1)-overlayer adsorption configuration on the CdSe(0001) surface. Using the model of Luedtke and Landman [18], the differences between edge and table lattice sites are modeled of as the difference between boundary and core chains. Luedtke and Landman found that the thermodynamics of boundary and core chains are quite different and dependent on nanocrystal size, however by averaging over all chains in the nanocrystal and summing over *all* possible chain configurations, we are able to neglect the difference between the two sites.

Assuming the headgroup-surface binding energy remains constant with chain type and dot size, the effects of headgroup-surface free energy contributions to the total free energy is minimal. The headgroup free energy is size dependent and follows the relation, $f_h = \gamma[a(r)-a(r)(1+\mathrm{D}/r)]$, where γ is the surface tension and D is the effective separation of the headgroup from the surface of the particle. Using the values $\gamma = 0.1k\mathrm{T}$ and D = 2.5 Å, the corrected free energy can be obtained. Note that the introduction of a strong headgroup surface interaction no longer leads to a “favored size”, therefore substantiating our claim of minimal headgroup surface interactions. This allows $P(\alpha)$ to be calculated by minimizing the free energy subject to the following constraints,

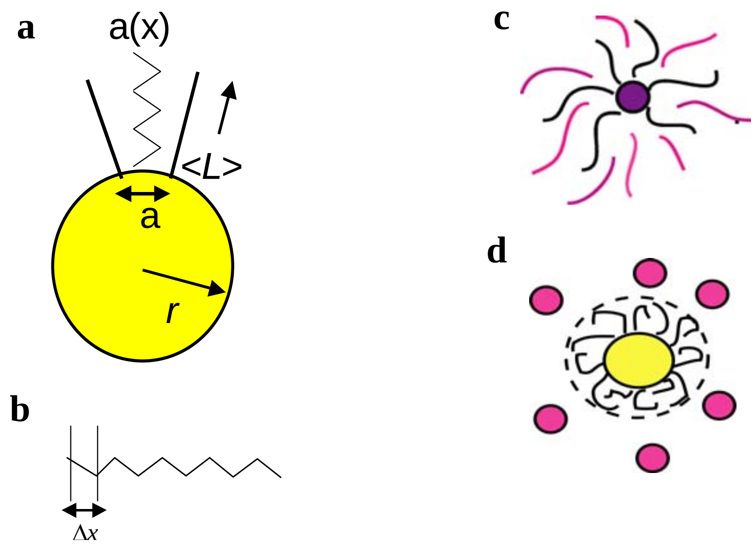

Figure 3.2. (a) Illustration of the effect of surface curvature or chain splaying on a QD facet where *a* is the area-per-headgroup, *a*(x) is the effective area-per-headgroup, <*L*> is the chain length, and *r* is the particle radius. (b) Illustration of the discrete segments, □x, to define the long axis of the chain. (c and d) Illustration of the effects of a (c) good and (d) bad solvent.

$$\sum P(\alpha)=1 \tag{3-2a}$$

$$\langle\phi(x)\rangle=\sum_{\alpha} P(\alpha)\phi(\alpha,x)=a(x) \tag{3-2b}$$

where

$$a(x)=\frac{a}{r^{2}}(x+r)^{2} \tag{3-3}$$

$\phi(x)$ is the average density or number of $-CH_2$ groups at a distance x from the surface of the nanoparticle and $a(x)$is the effective area per headgroup due to surface curvature (Fig. 3.2a). This yields an expression for $P(\alpha)$ containing the partition function, z.

$$P(\alpha) = \frac{1}{z} e^{-\frac{\varepsilon(\alpha)}{kT} - \frac{1}{kT}\int \pi(x)\phi(\alpha,x)dx} \quad (3\text{-}4)$$

where

$$z = \sum_{\alpha} e^{-\frac{\varepsilon(\alpha)}{kT} - \frac{1}{kT}\int \pi(x)\phi(\alpha,x)dx} \quad (3\text{-}5)$$

In order to carry out these computations along the *x*-axis, the axis extending along the radius has been divided into discrete segments, Δx, allowing the above integral to be transformed into a sum of discrete steps, which are effectively related to the number of -CH_2 segments (Fig. 3.2b). The terms $\pi(x)$ represent Lagrange multipliers associated with the packing constraints and represent the 1-d pressure applied to the chain. The free energy of the ligand layer can be calculated under various conditions (good vs. bad solvents) using the Flory parameter, χ,

$$\chi = \frac{1}{kT}[w_{cs} - (w_{cc} + w_{ss})/2] \quad (3\text{-}6)$$

with w_{cs}, w_{cc}, *and* w_{ss} equal to the chain-solvent, chain-chain, and solvent-solvent interaction potentials, respectively (Fig. 3.2c and d). Systems where chain-chain and chain-solvent interactions are identical are said to be in a "good" or "athermal" solvent with $\chi << 1$ and systems where $\chi >> 1$ are labeled "bad" solvents. [19]

Figure 3.3 shows the free energy calculation of a C_{12} chain on a QD surface in “good” and “bad” solvents. Based on the mean field calculations, in a “good” solvent, such as hexane, the free energy decreases with decreasing radius (Fig. 3.3a). This result states that for a QD in a “good” solvent condition, the ligand layer is never in a thermodynamically stable conformation. This implies that chain packing will adopt an increasingly crystalline structure with increasing chain length as observed in SAMs, indicative of a passivating layer model that exhibits a *frozen kinetic* structure strongly dictated by the headgroup-surface interaction and not dimensional effects. In our earlier thermal and IR analysis of QD films, this behavior was not experimentally observed, suggesting thin film structures are in a “bad” solvent condition.[5]

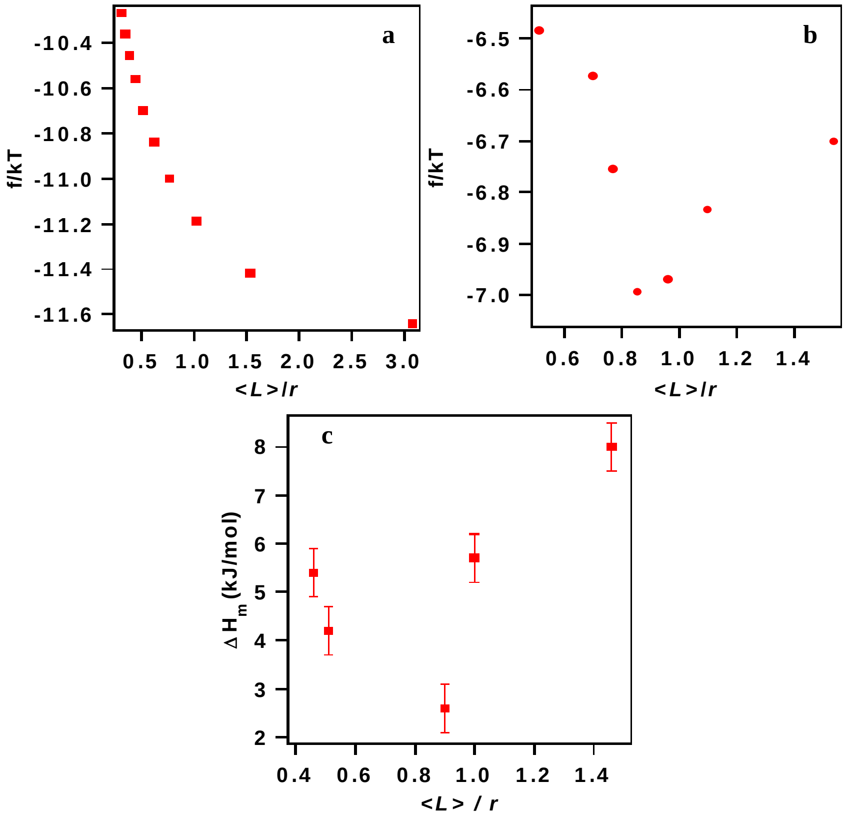

Figure 3.3 (a, b, and c). Free energy calculation of a C_{12} chain on a QD surface in (a) good and (b) bad solvents and (c) experimental latent heats of melting, ΔH_m, as a function of <*L*>/*r*.

In a "bad" solvent condition, a minimum in the conformational free energy of the ligand is observed at a "favored size" of <*L*>/*r* ~ 0.9 (Fig. 3.3b). The passivant layer can be envisioned as existing in a thermodynamically favored configuration dominated by ch-ch packing interactions. This means that the passivant layer will experience dimensional effects as the ratio of chain length and particle size varies. These predictions correspond with our earlier findings for chain packing on CdSe QD thin films, allowing our glassy QD film structures self-assembled by solution evaporation to be envisioned as a “bad” solvent condition.[5] Even more interesting, the calculated “favored” size observed in Fig. 3.3b is in quantitative agreement with the observed maximum in enthalpies of melting of dodecanthiolate coated Au nanocrystals reported in reference 10. The theoretically predicted “favored” size $<L>/r$ can be thought of as a balance between forces of energy and entropy. At large particle sizes, energy dominates, but at small particle sizes entropy dominates.

A measure of the predicted chain conformation on a QD surface can be achieved by plotting $\phi(x)$ for a given chain length as a function of various QD sizes. Figure 3.4 shows the calculated values of $\phi(x)$ vs the distance from the QD surface for a C_{12} alkyl chain passivating CdSe. Since $\phi(x)$ represents the average number of $-CH_2$ groups at a distance x from the surface of the QD in a "bad" solvent condition, a value of $\phi(x) = 1.0$ states that an all-trans conformation is achieved by the chain, while a value of $\phi(x) > 1.0$ shows increasing gauche conformational defects on the chain. This produces

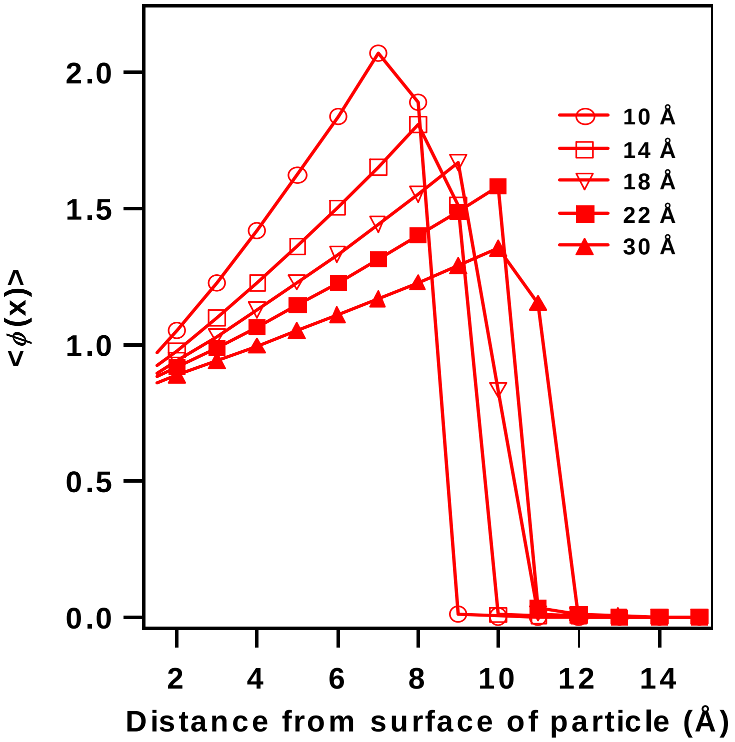

Figure 3.4. Calculated values of the average density, $\phi(x)$, as a function of distance from the surface of the quantum dot for various QD sizes.

effective chain compression, and a lower <*L*> value. Coupled to the compression, inclusion of gauche conformer defects tends to lower packing densities of the passivant layer on the QD surface. Inspection of Figure 3.4 indicates that a predominately crystalline all-trans conformation for the C_{12} alkyl chain passivating layer is predicted for QD sizes in excess of 20 Å. At particles sizes below 14 Å, the $–CH_2$ density is high, extending only 8 Å from the particle surface when a C_{12} all-trans conformer can extend nearly 15 Å. This means that nearly half of the chain is "curled up" or contains a large amount of gauche defects. From Fig. 3.4, we see that between 18 and 22 Å, the average chain density decreases (i.e. less defects) and the distance from the particle surface increases, reaching a value of nearly 12 Å, showing that the chains are nearing an all-trans, highly crystalline conformation. This gives rise to dimensionality effects arising at the CdSe-passivant $\langle L \rangle / r > 1.0$, for a C_{12} ligand.

Using eq. 3-3, the increase of the area per headgroup, $a(x)$, scales as r^{-2} implying that an increase of $a(x)$ occurs at small particle sizes and most likely leads to the increase in gauche conformers. This leads to an expected increase in chain splaying on the surface to maximize area at the expense of chain packing. As the particle radius increases, the "effective" area per headgroup, $a(x)$, tends towards the "normal" area per headgroup, a, inducing restricted movements of the surface bound ligands. The restricted movements results in strong ch-ch van der Waals interactions and all-trans packing motifs as predicted from the large $\phi(x)$ values (Fig. 3.4) and the increase in $\pi(x)$ (Fig. 3.5).

Experimental verification of the dimensional predictions can be generated by comparison of the theoretical calculations for the passivant layer and the experimental melting passivant layer behavior on a QD surface measured by differential scanning calorimetry (DSC). From the DSC measurements, the energy required to melt the chains via gauche conformer

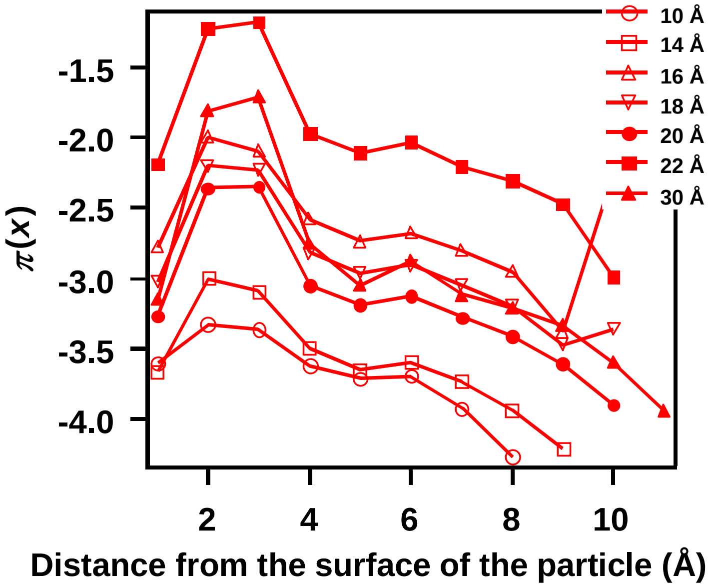

Figure 3.5. Calculated values of π(x) with the negative values of π(x) indicating that the chains are being "pushed on" in order to conform to the packing constraints required by a bad solvent. The values of π(x) increase and then decrease as the radius is increased, indicating that the minimum structure obtained in the free energy is a result of a balance between "pushing" and "pulling" on the chain. When $<L>/r > 1$, the volume available to the chains increases significantly as the distance from the surface increases. This suggests that in a bad solvent the chains must be "pushed on" quite a bit in order to pack as close to the surface as possible. However, when $<L>/r < 1$, the volume effectively does not change and the chains must be "pulled on" in order to meet the packing constraints.

formation can be directly measured. This provides a comparable value of the configurational free energy for chain melting at given $<L>/r$ values. Using the calculated free energy seen in figure 3.3b and the experimental latent heats of melting, ΔH_m, measured by DSC, a correlation is observed between 0.9 <

$<L>/r < 1.0$ in the free energy and latent heats of melting (Figure 3.3c). The experimental validation of the theoretical predictions suggest after the free energy minimum is reached packing constraints lead to an increase in configurational free energy for the passivant layer. In Fig. 3.4, where the value for $\phi(x)$ decreases as $<L>/r > 1.0$, an increase of gauche conformers of the chain on the surface of the QD is predicted, arising from changes in packing density on the QD surface. As the energy for a gauche conformer is only ~22 meV, it is expected that for systems where there is sufficient volume and/or greater rotational degrees of freedom, an increase in gauche conformers would be expected.

3.4. Dimensional vs. Domain Effects. In a previous study on chain packing and chain dynamics on a QD surfaces, the influence of QD size was investigated by a correlation of the thermal melting behavior and temperature dependent IR properties for a series of QDs. [5] In this study, it was observed that changes in chain tilting and conformational integrity were experienced for QDs below a radius of 25 Å. These changes were ascribed to dimensionality effects on QD surfaces arising from changes in the enthalpic ch-ch stabilization, as well as enhanced headgroup-surface interactions. These results are analogous to the observation of reduced dimensionality effects on Au nanoparticles. [20,21,10]

The statistical mechanical model above predicts a <*L*>/*r* dependence. This dimensional model predicts the stability of alkyl chains on the surface of size restricted particles will be directly related to the ratio of chain length to QD size needed to minimize the conformational free energy of the chains. If a particle is very small, the surface area becomes much smaller resulting in increased chain splaying and therefore fewer chains effectively pack on the surface. This will tend to decrease the thermodynamic stability of the particle. In light of the earlier studies, this predicts analysis of the DSC and temperature dependent IR will provide direct insight in to the validity of the theoretical model.

By analysis of conformationally sensitive IR modes, the theoretical model can be experimentally verified. A measure of the crystallinity for an alkyl chain can be attained by inspection of the frequency and linewidth of the spectral region between 2800 – 3100 cm^{-1}. This region can be assigned to contributions from the ν_{CH} stretching modes (d^+, d^-) for $-CH_2$ along the polymethylene alkylamine chains and to the end-methyl groups ($-CH_3$) (r^+, r^-). These modes are highly dependent on the chain crystallinity and packing conformation of the alkylamine chains assembled on the QD surface. [5,22-24] Observation of the d^+ and d^- modes between 2848-2850 and 2914-2916 cm^{-1} are consistent with an assignment of a predominately all-trans packing arrangement at the surface of a QD, with a shift of these mode frequencies

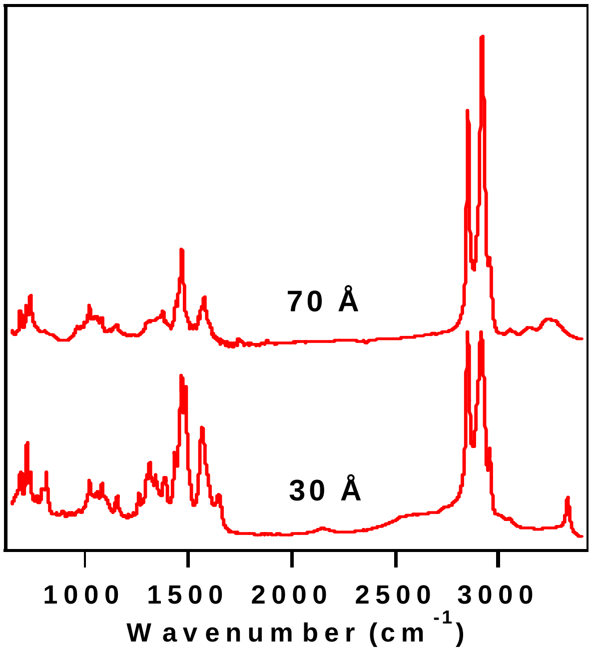

Figure 3.6. Room temperature infrared absorption between 700-3100 cm^{-1} of 70 and 30 Å CdSe QDs coated with HDA.

occurring with the onset of gauche conformers. The band observed at ~3331 cm^{-1} arises from the N-H asymmetric stretch which loses intensity with increasing size and can be attributed to changes in chain tilt on the surface of the QD. As the chain tilts, the intensity of the NH mode increases, due to loss of surface selection rules. Coupled to the loss of the NH modes, splitting of the r^+/r^- modes can be observed due to symmetry breaking. Coupled to these IR signatures, "twist and wag" (T_x and W_x) progressions between 1150-1350 cm^{-1} can be observed indicative of high packing densities for all trans-conformations. Furthermore signature modes for hexagonal packing on the

QD surface are observed at 720 (P_1) and 1470 (δ) cm^{-1} in CdSe passivated with alkyl amines.

The purely dimensional model is clearly observed for $<L>/r < 1.0$, for example a 70 Å CdSe particle passivated with HDA, where the chain packing motif is hexagonal and highly crystalline with clearly resolved "twist and wag" (T_x and W_x) progressions (Fig. 3.6). For the 70 Å CdSe QD, loss of intensity for the NH mode and a splitting of the methyl modes is indicative of chain tilting in these materials. This suggests in this size regime, the chain length compensates for the particle surface effects and the thermodynamics are entirely dominated by ch-ch enthalpic terms. For $<L>/r > 1.0$, for example a 30 Å CdSe particle passivated with HDA, the reduced dimensionality of the CdSe QD allows for greater rotational degrees of freedom of the surface groups, and onset of chain tilting as evidenced by the observation of the NH mode at 3331 cm^{-1}, and a loss of the methyl mode splitting. The change in tilting and chain freedom arises from an effective lower packing density for the passivants.

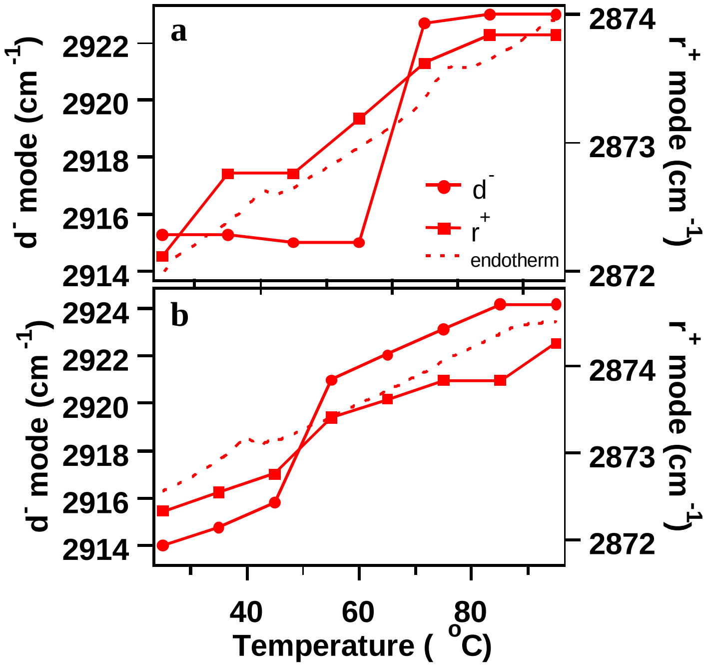

Figure 3.7 (a and b). Thermal behavior of the methylene (d$^-$) and methyl (r$^+$) modes and corresponding DSC traces for the (a) 70 and (b) 30 Å CdSe QD glassy films passivated with hexadecylamine. Note the correlation between the shifts of the d$^-$ and r$^+$ peaks with the endothermic transitions.

The thermal analysis data, obtained by DSC measurements, confirm these observations with a two-step melting behavior for 70 Å CdSe and a one-step curve for the 30 Å CdSe. In figure 3.7, a comparison of the thermal behavior of the methylene (d$^-$) and methyl (r$^+$) modes is shown for the 30 and 70 Å QD films passivated with hexadecylamine (HDA; <*L*> ~ 21 Å). The 2-step melting behavior arises from strong ch-ch interactions in the packing resulting in an initial end-gauche formation with heating, followed by complete chain collapse at elevated temperature. For the 70 Å CdSe materials, the onset of melting is observed initially for the methyl IR mode (ν_{CH3} ~ 2850 cm^{-1}), which is shifted to higher frequency upon heating, and a delayed frequency shift for the methylene IR mode (ν_{CH2} ~ 2916 cm^{-1}), implying the onset of end-gauche and internal gauche conformers are not thermodynamically equivalent (Fig 3.7a). Coupled to the onset of the intra-chain gauche defects is increased conformational disorder as evidenced by the loss of intensity from the T_x and W_x progression series modes as a function of temperature. [25] In contrast, the 30 Å CdSe QD with a C_{16} passivating layer exhibits a correlated melting event with loss of crystallinity occurring simultaneously with end-gauche formation, explaining the 1-step melt event. Above the melting phase transition temperature (> 50 ^{o}C), a quasi-linear hardening of the modes is observed consistent with collapse of the alkyl chains. As the 30 Å assembly is heated, ν_{NH2} begins to lose intensity at ~328 K (55 ^{O}C) indicating that the mechanism for chain collapse on small particles involves chain canting followed by chain collapse.

The magnitude of the frequency shift in the antisymmetric –CH_2 stretch (d^- mode) is 10.0 and 4.0 cm^{-1} for the 30 and 70 Å QD assemblies, respectively (Fig 3.7). The smaller $\Delta\nu$ value for the 70 Å assemblies leads to the assumption that packing is more constrained on these particles as seen in the two-phase melt behavior, with end methyl free rotation (~315 K) occurring in a thermodynamically separate event than the methylene chain collapse event

(~345 K). Evidence for a tightly packed state is also seen in the lack of $–NH_2$ absorption at ~3330 cm^{-1} implying an all-trans, densely packed motif. The differences in the magnitude of the shifts implies the 30 Å assembly is able to achieve a more liquid like disordered collapse state, in comparison to the 70 Å dot, most likely due to the increased effective curvature for the size restricted surface. These results can be interpreted in terms of dimensionality effects ($1 > \langle L \rangle / r > 1$) as predicted theoretically.

3.4.1. Experimental validity of dimensionality. A test for the validity of the dimensionality model can be determined by inspection of the thermal behavior for various chain lengths for a given QD size. The onset of dimensional effects is observable by inspection of the temperature dependent IR and analysis of the methyl and methylene modes. A system exhibiting dimensional stress will exhibit a one-step melting curve ($\langle L \rangle / r > 1$), while systems without dimensional stress ($\langle L \rangle / r < 1$) are expected to exhibit a two-step melting event in which the chain packing will be dominated entirely by the ch-ch interactions. Chain lengths of 27 carbon atoms would be needed to induce

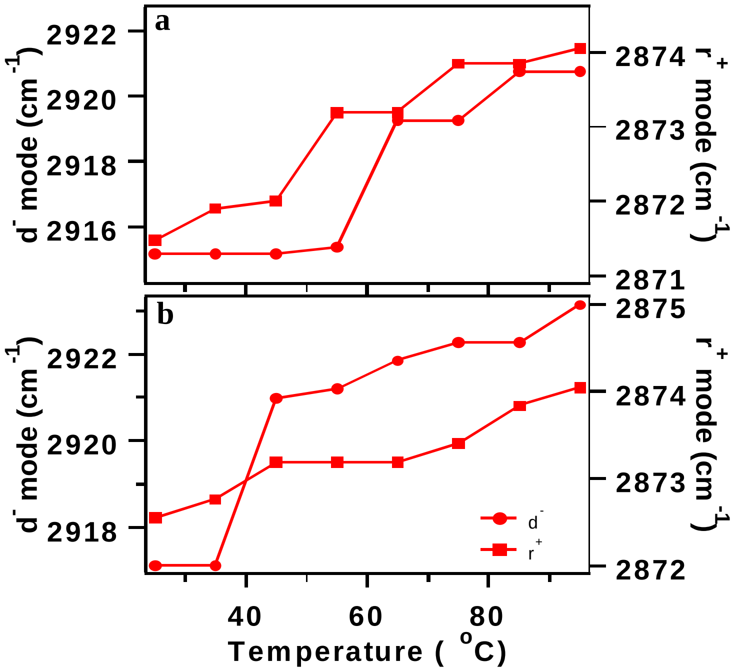

Figure 3.8 (a and b). Thermal behavior of the methylene (d^-) and methyl (r^+) modes for 70 Å CdSe QD glassy films passivated with (a) eicosamine and (b) dodecylamine.

dimensional effects to a 70 Å (r = 35 Å) particle. For a 30 Å (r = 15 Å) particle, however, chain lengths of 11 carbon atoms or more would be needed to induce dimensional effects ($<L>/r < 1$). This suggests for chain lengths shorter than C_{12}, dimensional effects will be absent in both of the systems, while for C_{16} passivation dimensional effects for the 30 Å dots are most crucial, predicting a change in the packing and thermotropic properties should be observable.

The influence of dimensionality on packing for a series of chain lengths on a 70 Å particle exhibits a two-step melting curve similar to C_{16} coated QDs for all chain lengths > C_8 (C_8, C_{12}, C_{16}, C_{20}). These chain lengths are within the $<L>/r < 1$ regime for chain packing, which means the packing of the chains will be dominated by strong ch-ch interactions and at room temperature the crystallinity will be largely influenced by the number of available ch-ch interactions (Fig. 3.8). Consistent with ch-ch interactions dominating the packing for systems in the $<L>/r < 1$, for chain lengths < C_5 on a 70 Å QD disordered packing is observed. The C_5 chain can be envisioned as in a melt state at room temperature on the surface, with a loss of structural regularity arising from the minimal available contribution of ch-ch interactions to stabilize the passivant layer on the surface. For the C_5 system, the lack of crystalline order is clearly seen in the frequency of the CH_2 modes, which is shifted to higher frequency indicative of an increase in gauche conformer concentrations along the chain. Consistent with the increased gauche conformations, the lack of shifts in the $d^{+/-}$ modes with temperature and the lack of peaks at 720 (P_1) and 1470 (δ) cm^{-1} which are signature packing modes, suggest the chains are randomly oriented on the QD surface. These studies indicate that at large quantum dot sizes (large r), dimensionality effects may be minimal due to $<L>/r$ typically being less than 1. In effect, adsorbed molecules experience a quasi-planar surface with respect to the chain length and mimic the observation of organic passiavting layers in self-assembled monolayers.

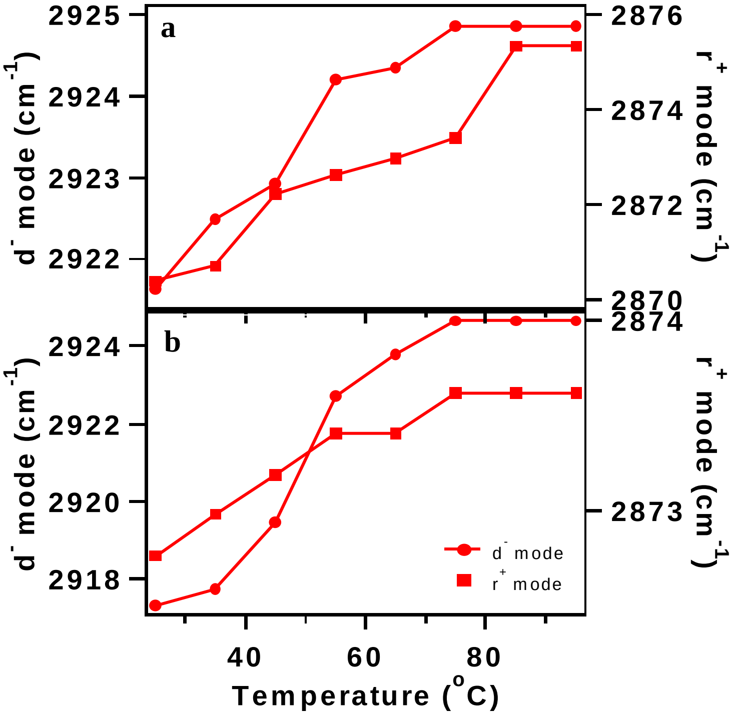

Figure 3.9 (a and b). Thermal behavior of the methylene (d^-) and methyl (r^+) modes for 30 Å CdSe QD glassy films passivated with (a) octylamine and (b) dodecylamine.

Dimensionality effects on the other hand for small QD sizes should be observed as <*L*>/*r* can be systematically tuned. Using the above dimensional model, a one-step melt transition at <*L*>/*r* ≥ 1.0 is predicted for a $C_n > C_{12}$ (<*L*> ~ 15.4 Å) chain length on a 30 Å QD and a two-step melting curve for chain lengths below C_{12}. Surprisingly, the observation of a one-step melt for 30 Å QDs passivated with HDA (<*L*> ~ 20 Å), dodecylamine (DDA, <*L*> ~ 15 Å) or octylamine (OA, <*L*> ~ 10 Å) indicates purely dimensional effects do not accurately describe the packing of the passivant molecules on a surface for these smaller QDs (Figure 3.9). Based on the 30 Å CdSe-DDA d^-

mode frequency of 2917 cm^{-1} compared to the value of 2914 cm^{-1} for 30 Å

CdSe-HDA and 2917 cm^{-1} for CdSe-OA, an insignificant loss of crystallinity in the packing arises as the chain length decreases, in contrast to the expected behavior for a purely dimensional model (Fig. 3.10). Furthermore, the HDA, DDA, and OA coated dots show ν_{NH2} ~3330 cm^{-1} with their peak positions differing by less than 1%. These materials all exhibit similar thermal behavior suggesting that packing on a 30 Å QD varies little with chain length in contrast to prediction of a purely dimensional model. The lack of a two-step melt event for the DDA and OA coated dots puts a purely dimensional model in jeopardy. This suggests that the small particle size may affect the chain packing by limiting the ability to form a stable crystalline domain on the QD facet. The

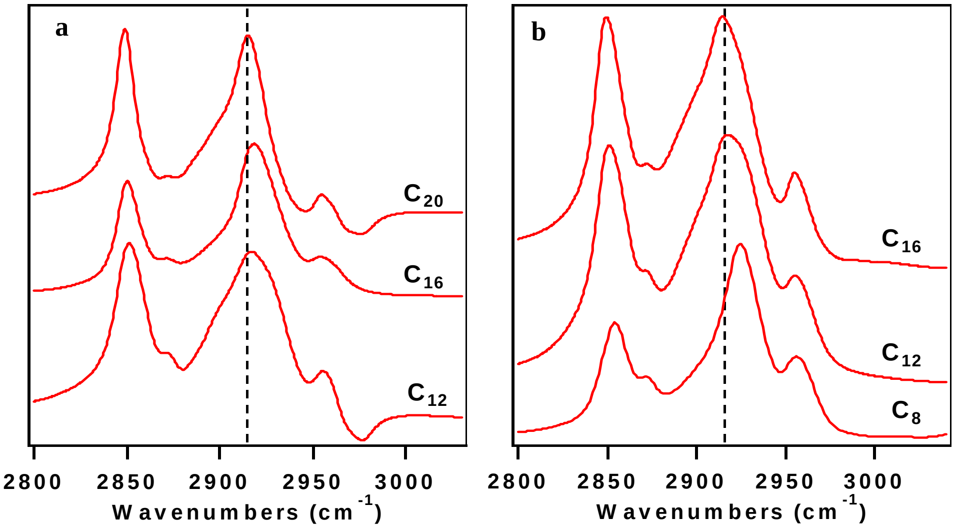

Figure 3.10 (a and b). Room temperature infrared absorption between 2800-3100 cm^{-1} of (a) 70 Å CdSe QDs coated with H_2NC_{20}, H_2NC_{16}, and H_2NC_{12} and (b) 30 Å CdSe QDs coated with H_2NC_{16}, H_2NC_{12}, and H_2NC_8.

evidence of no apparent two-step melt on small dots makes it necessary to describe the phase behavior of the alkyl chains in a different way, perhaps in terms of domain structures.

3.4.2. Domain Effects on QD Passivation. Domain induced packing stress in materials without a large facet may arise due to the limited number of Cd lattice points on a facet for a passivating layer to interact with. At a low packing density, the ch-ch interactions are not strong enough to overcome the limited crystalline domain available. In SAMs, the observed minimum domain size of organic passivants is on the order of 40-50 Å. In Au SAMs, chain domain sizes of 40-50 Å are equivalent to 14-17 Au unit cells. [26] The same observations on nanoscale surfaces have not been clearly identified, but have been indirectly observed. Korgel and Fitzmaurice have observed that chain stabilization on Ag nanocrystals is highly sensitive to the $<L>/r$ ratio, and the free energy minimum occurs at $<L>/r \sim 0.60$. [27] The obtained ratios are the same for C_{12} and C_8 coated nanocrystals and their ratios are similar to the values obtained by Whetten and co-workers. [28] Thermodynamic stabilization in light of domain size was never discussed, mainly from the fact that the smallest sized nanocrystal used in these studies were ~ 36 Å, which represent ~10 Ag unit cells ($d_{Ag-Ag} \sim 2.88$ Å)[29], more than enough unit cells for chain stabilization.

Table 3.1. Minimum observed domain and the correlating number of repeat unit cells of alkanethiols on Au(111) surfaces[a].

Chain Length	Average Domain Size (Å)	# of alkyl unit cells
C_{18}	35.2	7
C_{14}	43.9	9
C_{10}	36.4	7

[a] Ref. 25

An interesting observation by Lennox and co-workers was made on alkanethiolate coated Au nanocrystals. [30,31] They found that the local Au-S bonding was the same on the nanocrystal as seen on bulk Au SAMs. This only occurred, however, for particle sizes larger than 22 Å where the number of Au unit cells is ~7 (d_{Au-Au} ~ 2.88 Å)[29], just at the threshold for the minimum alkyl chain unit cells needed for stabilization. These results indicate that below 22 Å, Au nanocrystals may lack the effective domain size needed to reach a kinetically favorable chain unit cell dimension. This provides indirect evidence for the existence of domain effects in nanomaterial packing.

The influence of domain limitations for CdSe particles < 30 Å can be interpreted in terms of the number of required repeat unit cells to form a stable crystalline domain on a surface. The alkyl chain domain size is kinetically driven and has an average size of ~ 40 Å, which corresponds to approximately

8 repeat alkyl chain unit cells (Table 3.1).[16] In comparison, Table 3.2 shows the repeat Cd-Cd unit cells which vary from 6 (32 Å) to 14 (70 Å). These numbers can be compared against known domain sizes of alkanethiols on Au(111) surfaces[26] to compare the number of unit cells available in the CdSe(001) lattice for packing versus the kinetically favored number of alkanethiol unit cells required for stabilization (Tables 3.1 and 3.2). It is seen that approximately 7-9 alkyl unit cells are needed for stabilization. In contrast, only ~ 6 unit cells are available for packing in a 32 Å dot versus ~ 14 unit cells in a 70 Å dot. Not surprisingly, a 44 Å particle is needed to achieve 9 CdSe unit cells which is minimum size needed for thermodynamic stabilization of the chains and it occurs precisely where we witnessed a change in the melting behavior of HDA coated dots in Ref. 5. These results along with the previous experiments on Au nanocrystals provide evidence for the existence of domain

Table 3.2. Effective facet dimension and number of repeat unit cells on the wurtzite CdSe (0001) face.

Particle radius (Å)	Facet dimension (Å)	# of Cd-Cd unit cells
16	27.7	6.4
22	38.7	9.0
35	60.6	14.1

sizes in QDs, suggesting QD instability arising from loss of the passivating layer may arise for QDs having fewer available passivant binding sites per facet. This suggests that for CdSe, particle sizes of 45 Å or greater should be used for materials' applications, as these appear to be the most energetically stable sizes.

3.5. Conclusions

In conclusion, we find that amphiphilic passivant packing on a CdSe QD can be described in terms of both dimensional and domain models. The results indicate that at very small particle sizes ($r < 22$ Å) disordered packing of the organic passivant arises due to the lack of an available domain size for chain packing on the faceted QD surface. This results in increased chain splaying to maximize chain crystallinity and particle stabilization. At particle sizes above 45 Å, the chain packing thermodynamics is highly dependent on the ratio of the chain length ($<L>$) to the particle radius, r, with a thermodynamic minimum for chain packing at $<L>/r \sim 1.0$. These results indicate that ligand exchange kinetics on these particles should be highly size dependent and sensitive to dimensional and domain effects. Such studies are currently underway.

Acknowledgements. This work was supported by a NSF-CAREER Award (DMR-9875940) and a NSF Nanotechnology Grant (DMR-9871849).

References

(1) Katari, J. E. B.; Colvin, V. L.; Alivisatos, A. P. *Journal of Physical Chemistry* **1994**, *98*, 4109-4117.

(2) Prozorov, T.; Gedanken, A. *Advanced Materials* **1998**, *10*, 532-535.

(3) Cordero, S. R.; Carson, P. J.; Estabrook, R. A.; Strouse, G. F.; Buratto, S. K. *Journal of Physical Chemistry B* **2000**, *104*, 12137-12142.

(4) Kim, B. S.; Avila, L.; Brus, L. E.; Herman, I. P. *Applied Physics Letters* **2000**, *76*, 3715-3717.

(5) Meulenberg, R. W.; Strouse, G. F. *Journal of Physical Chemistry B* **2001**, *105*, 7438-7445.

(6) Murray, C. B.; Norris, D. J.; Bawendi, M. G. *Journal of the American Chemical Society* **1993**, *115*, 8706-8715.

(7) Alivisatos, A. P. *Journal of Physical Chemistry* **1996**, *100*, 13226-13239.

(8) Bawendi, M. G.; Carroll, P. J.; Wilson, W. L.; Brus, L. E. *Journal of Chemical Physics* **1992**, *96*, 946-954.

(9) Becerra, L. R.; Murray, C. B.; Griffin, R. G.; Bawendi, M. G. *Journal of Chemical Physics* **1994**, *100*, 3297-3300.

(10) Hostetler, M. J.; Wingate, J. E.; Zhong, C. J.; Harris, J. E.; Vachet, R. W.; Clark, M. R.; Londono, J. D.; Green, S. J.; Stokes, J. J.; Wignall, G. D.; Glish, G. L.; Porter, M. D.; Evans, N. D.; Murray, R. W. *Langmuir* **1998**, *14*, 17-30.

(11) Dubois, L. H.; Nuzzo, R. G. *Annual Review of Physical Chemistry* **1992**, *43*, 437-463.

(12) Cumberland, S. L.; Hanif, K. M.; Javier, A.; Khitrov, G. A.; Strouse, G. F.; Woessner, S. M.; Yun, C. S. *Chemistry of Materials* **2002**, *14*, 1576-1584.

(13) Gelbart, W.; Ben-Shaul, A.; Roux, D. *Micelles, membranes, microemulsions, and monolayers*; Springer-Verlag: New York, 1994.

(14) Steenhuizen, L.; Kramer, D.; Benshaul, A. *Journal of Physical Chemistry* **1991**, *95*, 7477-7483.

(15) Heath, J. R.; Knobler, C. M.; Leff, D. V. *Journal of Physical Chemistry B* **1997**, *101*, 189-197.

(16) McGann, M. R.; Lacks, D. J. *Journal of Physical Chemistry B* **1999**, *103*, 2796-2802.

(17) CRC Handbook of Chemistry and Physics, *ed.* D.R. Lide, vol. 74, CRC Press: Boca Raton, 1993.

(18) Luedtke, W. D.; Landman, U. *Journal of Physical Chemistry* **1996**, *100*, 13323-13329.

(19) Szleifer, I.; Ben-Shaul, A.; Gelbart, W. M. *Journal of Physical Chemistry* **1990**, *94*, 5081-5089.

(20) Badia, A.; Cuccia, L.; Demers, L.; Morin, F.; Lennox, R. B. *Journal of the American Chemical Society* **1997**, *119*, 2682-2692.

(21) Hostetler, M. J.; Stokes, J. J.; Murray, R. W. *Langmuir* **1996**, *12*, 3604-3612.

(22) Nielsen, J. R.; Hathaway, C. E. *Journal of Molecular Spectroscopy* **1963**, *10*, 366-377.

(23) MacPhail, R. A.; Strauss, H. L.; Snyder, R. G.; Elliger, C. A. *Journal of Physical Chemistry* **1982**, *86*, 5145-5150.

(24) Parikh, A. N.; Gillmor, S. D.; Beers, J. D.; Beardmore, K. M.; Cutts, R. W.; Swanson, B. I. *Journal of Physical Chemistry B* **1999**, *103*, 2850-2861.

(25) Bardeau, J. F.; Parikh, A. N.; Beers, J. D.; Swanson, B. I. *Journal of Physical Chemistry B* **2000**, *104*, 627-635.

(26) Camillone, N.; Chidsey, C. E. D.; Liu, G. Y.; Putvinski, T. M.; Scoles, G. *Journal of Chemical Physics* **1991**, *94*, 8493-8502.

(27) Korgel, B. A.; Fitzmaurice, D. *Physical Review B-Condensed Matter* **1999**, *59*, 14191-14201.

(28) Whetten, R. L.; Shafigullin, M. N.; Khoury, J. T.; Schaaff, T. G.; Vezmar, I.; Alvarez, M. M.; Wilkinson, A. *Accounts of Chemical Research* **1999**, *32*, 397-406.

(29) Laibinis, P. E.; Whitesides, G. M.; Allara, D. L.; Tao, Y. T.; Parikh, A. N.; Nuzzo, R. G. *Journal of the American Chemical Society* **1991**, *113*, 7152-7167.

(30) Badia, A.; Lennox, R. B.; Reven, L. *Accounts of Chemical Research* **2000**, *33*, 475-481.

(31) Bourg, M. C.; Badia, A.; Lennox, R. B. *Journal of Physical Chemistry B* **2000**, *104*, 6562-6567.

PART II: Effect of Defects on the Optical and Vibrational Properties of Semiconductor Quantum Dots

Chapter 4: Polaronic Defects and Electron-Phonon Coupling in CdSe Quantum Dots under Hydrostatic Pressure

Most of this chapter has appeared in print:
Meulenberg, R.W. and Strouse, G.F. *Phys. Rev. B* **66**, 035317 (2002).

4.1. Introduction

In semiconductor nanocrystals, or quantum dots (QDs), the size dependent nature of the physical properties can give rise to systematic changes in the electron-phonon (*el-ph*) coupling and lattice covalency, particularly for materials in the strongly confined limit. Pressure tuning of electronic levels which are highly sensitive to the covalency and the magnitude of *el-ph* coupling in materials can be probed a combination of photoluminescence (PL) and vibrational analysis. Although theoretical studies of donor/acceptor (D/A) states in CdSe QDs predict changes in polaronic coupling between donor electronic levels and interior core electronic levels following a $1/r^2$ scaling law, [1-4] these scaling laws have not been previously observed on CdSe. [5-10] The observation of pressure coefficients for CdSe QDs in this manuscript can be classified in accord with two size regimes, strong ($r < a_o$) and moderate ($r \sim a_o$) confinement, and suggest donor state contributions to the photophysics of CdSe QDs may be important. In fact, as the radius of the crystallite approaches the Bohr radius (moderate confinement), the values of the pressure coefficients approach the bulk values as expected for materials in the quantum confined limit and are reflected experimentally in the photoluminescence (PL) and resonance Raman spectroscopy. This allows a scaling law to be generated for the pressure coefficients if the donor states are accounted for in these materials.

QDs are an ideal system to observe how pressure induced changes in electronic levels can be influenced by changes in *el-ph*, lattice covalency, and donor levels. Since the PL properties of CdSe are dominated by the $1S_{3/2}1S_e$ excitonic level (i.e. bright and dark excitons) delocalized over the entire particle, the pressure dependent properties of the materials should approach the bulk value as r approaches a_o. Pressure induced perturbation of the exchange coupling in these materials, as well as the excited state energies and the core lattice parameters allows pressure dependent optical and vibrational spectroscopy to be used as a convenient probe of changes in the lattice ionicity with pressure and the underlying size-dependent coupling to donor levels for these materials. [11, 12] Based on theoretical predictions, little to no pressure dependence ($dE^*/dp \sim 0$) is expected for the strongly confined limit (regime *1*,

$r < a_o$; ~ 30-40 % surface) and bulk like behavior should be observed as r approaches a_o, where $a_o = 56$ Å in CdSe. [13] The lack of pressure dependence in the strongly confined regime arises from the strong coupling of defect levels in the QD to the core levels due to the strong confinement of the exciton wave function. This results in the exitonic levels being primarily perturbed by the particle size, and not the electron-hole (*el-h*) interactions. Extrapolating the model, QDs in the moderate to weakly confined limit ($r \geq a_o$) (regime *2*: $r \geq a_o$; 20 % and below surface) are expected to exhibit pressure dependent behavior modulated by the size dependent contribution of polaron coupling to core levels which will be influenced by the magnitude of *el-ph* interactions in the QD lattice. In fact, optical studies on QDs under pressure have shown enhanced pressure response in InP, while in Si and CdSe no anomalous pressure dependence is observed. [5, 6, 10, 12] The lack of enhanced pressure dependencies in these studies suggest the high pressure behavior is dominated by structural modulations or pressure induced lattice stress that lead to interband crossing rather than defect state coupling to the core electronic levels. [14]

In this manuscript, we observe pressure dependence in the weakly confined regime approaching the reported bulk band edge pressure coefficient consistent with the lack of significant defect levels in the QD. Assuming donor state contributions to the delocalized excited state, a scaling law can be generated for the QDs in the moderate to weakly confined regime. We further observe that by correlating the small vibrational changes in the CdSe QD lattice, $d\omega/dp$, and the changes in the excited state optical properties, dE^*/dp, the density of state contributions from sub-gap D/A states to the core electronic levels induce polaronic defects which change with lattice covalency.

4. 2. Experimental

CdSe QDs were prepared by standard lyothermal methods using a single source precursor route. [15] Crystallinity and size dispersity (5-6 %) of the materials are monitored by absorption, powder x-ray diffraction (pXRD), and transmission electron microscopy (TEM) analysis. Typical absorption and photoluminescence (298 K; 1 atm) are presented in Fig. 4. 1.

The QDs were dispersed in *n*-hexane and put into a cylindrical optical-pressure cell (~ 110 μL). The optical pressure ceel was then inserted in to the high pressure unit in one of the four insersion point located on the cell (see Fig. 4.2a). High pressures were generated using a hydraulic pump coupled to a pressure-intensifying ram. Use of *n*-hexane as the pressure transmitting medium in a liquid pressure optical cell [16] allows hydrostatic pressures up to 0.30 GPa (3.0 kbar) to be generated with minimal contributions from pressure induced solvent effects based on the small degree of fractional compression of

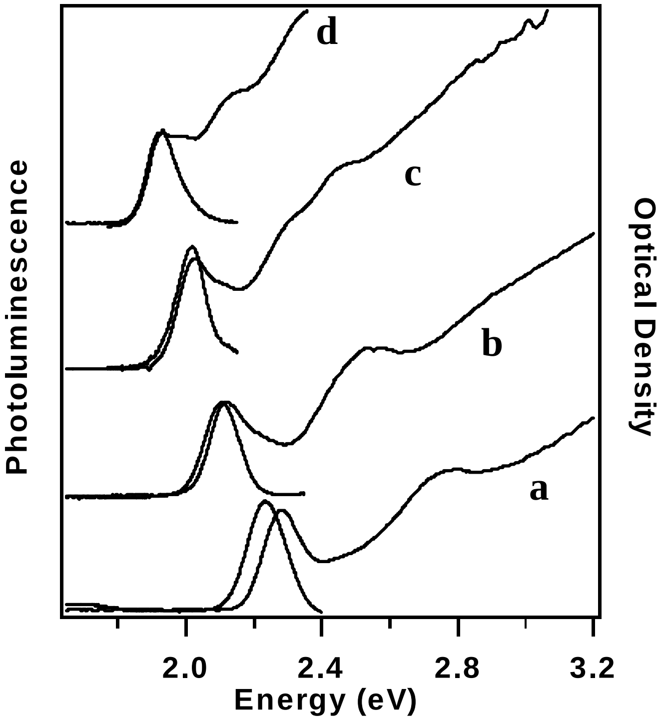

Figure 4.1. Absorption and photoluminescence (p = 1 atm; T = 298 K) as a function of CdSe QD radius: (a) 19 Å, (b) 23 Å, (c) 30 Å, and (d) 43 Å. The PL spectra were obtained with 2.54 eV laser light; 80 mW power.

the solvent and the small change in dielectric constant in this pressure range for *n*-hexane. [17] Pressures were recorded within 50 bar using a digital transducer.

The luminescence and resonance Raman spectra (resonant with a high energy $1P_h1P_e$ transition) were collected in backscattering configuration using the 2.54 eV line of an 10W Spectra-Physics 2200 Ar-ion laser (488.0 nm, 80 mW power) as a pump source and collection of the spectra on a 0.5M ARC single spectrograph (1800 lines mm^{-1}, blaze = 500 nm) system coupled to a Princeton Instruments 512X512 liquid nitrogen cooled charge coupled device (CCD) array. A Holographic Notch filter (Kaiser optical) was used to reject the incident laser line. A schematic for the PL and Raman experiments is seen in Figure 4.2b.

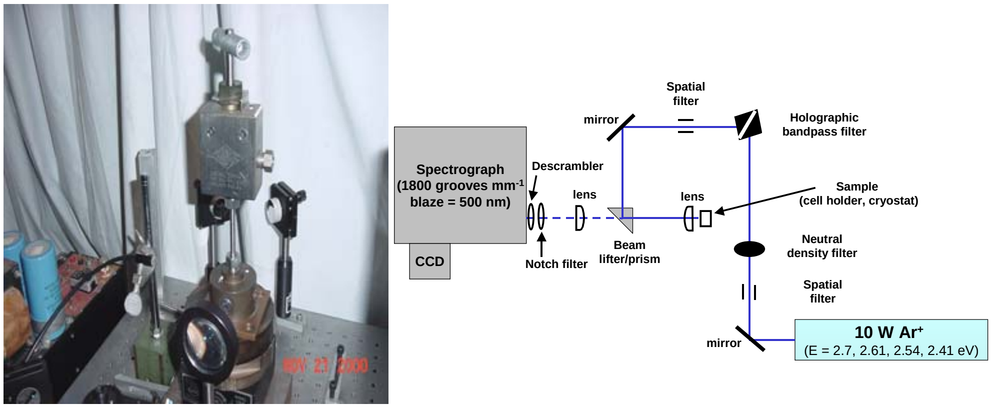

Figure 4.2. Liquid pressure optical cell (left) used for moderate pressure (0 - 1 GPa) measurements and layout of Raman and photoluminescence experiments (right)..

4.3. Polaronic Effects On Pressure Induced Optical Properties

In nanoscale condensed phase QDs, defect levels may arise from surface states and can play a significant role in the electronic nature of these materials. In fact, the influence of surface state perturbation on core electronic levels for QDs has been observed to influence the *el-h* trapping rates with a decrease in trapping rates at defect centers as the particle size increases. [18] In analogy to bulk materials, polarons at the surface of a QD can be treated as defect levels in the electronic band structure. Based on the size-dependence of the surface-to-volume (S:V) ratio in QDs, the degree of coupling of polarons and core levels should track the density of states of these sub gap levels. [1, 19] This allows the total energy of a quantum dot to be expressed as a core electronic term with a perturbation term for the polaron state as suggested by Efros et al,

$$E_{total} = \frac{\hbar^2 \pi^2}{2m_e r^2} - \frac{e^2}{\varepsilon r} f\left(\frac{d}{r}\right) \qquad (4\text{-}1)$$

where m_e is the electron mass, ε is the crystal dielectric constant, r is the particle radius, d is the donor position in the crystal, and $f(x) = 1 - \sin(2\pi x)/(2\pi x) + Cin(2\pi) - Cin(2\pi x)$ ($Cin(x)$ is a cosine integral and varies from $f(0) \sim 2.4$ to $f(1) \sim 1$). [1] This equation predicts the magnitude of the perturbation term should increase as the polaron states are localized on the interior of the dot. The perturbation term should also scale with the density of defects and the level of *el-ph* interactions in the QD material. In a QD, the *el-ph* terms scale with the dot size. [20]

Small changes in the bulk modulus $(B_o^{'} = 11)$ in the low pressure range (< 1 GPa) for wurtizte CdSe indicate that structural effects on the PL should be minimial. [6] The magnitude of the pressure induced shifts in the PL are expected to track the contribution of the core-polaron interaction, modulated

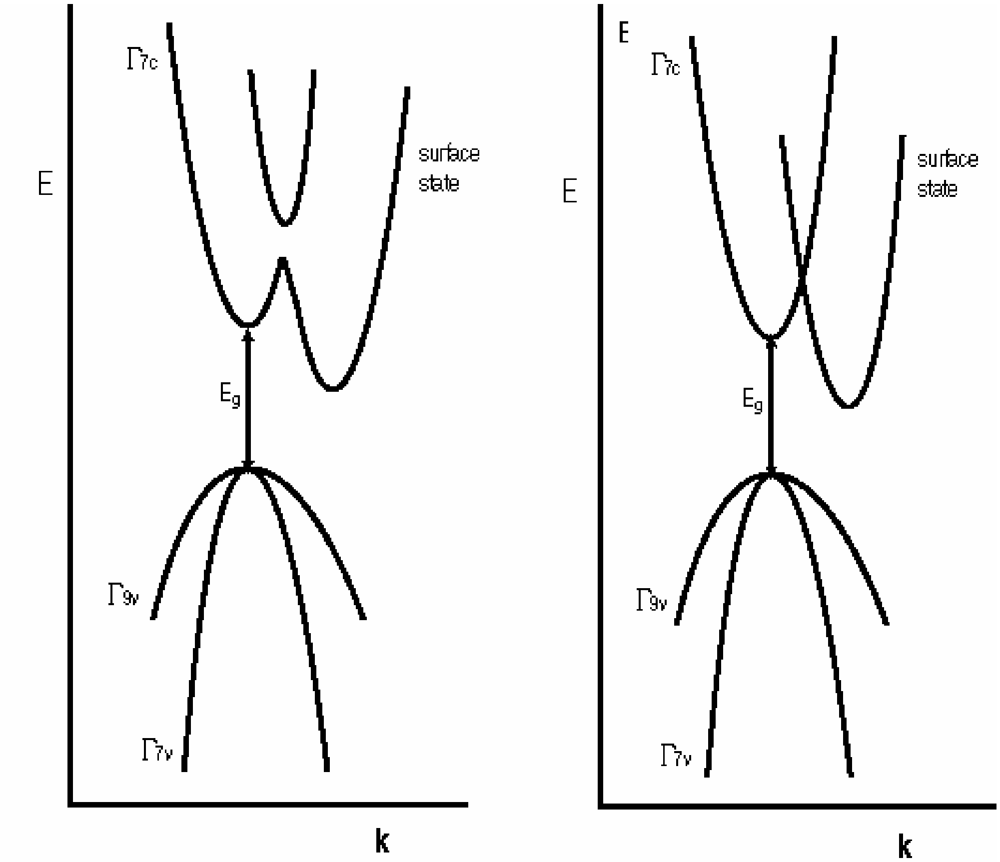

Figure 4.3. Schematic band diagrams illustrating the extreme limits of polaron-core coupling seen in QDs. (A) illustrates the strongly confined limit, where polaronic coupling is largest, and induces a perturbation to the total QD energy. (B) illustrates the bulk limit, where polaronic coupling is minimal.

by subtle changes in the lattice covalency with confinement, size, and pressure. For strongly confined systems (regime *1*), the electronic wave function is delocalized over the whole crystal volume, indicating complete coupling of the interior crystal states to the exterior polaronic defect states (Fig. 4.3a) and can be represented in terms of a non-adiabatic surface in which the tunneling barrier for coupling is small. [1] We expect little to no pressure dependence in this regime due to the magnitude of the *el-h* confinement in this size regime and the small barrier for core-polaron interactions. Similar models have been used to explain pressure dependent donor states contributions in bulk semiconductors and inorganic materials. [21, 22] In the moderately to weakly confined regime (regime *2*), the electronic wave function decreases rapidly at the crystal surface, which gives rise to a classical electronic barrier between the two states (Fig. 4.3b). This results in weakly coupled interactions between the D/A states and the core levels. Deviations from bulk-like behavior in this regime can arise from perturbation of the *el-ph* coupling in these dimensionally restricted materials.

Selected pressure dependent optical spectra for a 22.5 Å radius particle are shown in Fig. 4.4a. The most striking feature of the pressure dependent PL data (Fig. 4.4b) is the lack of pressure response below 22.5 Å radius ($dE^*/dp =$

0

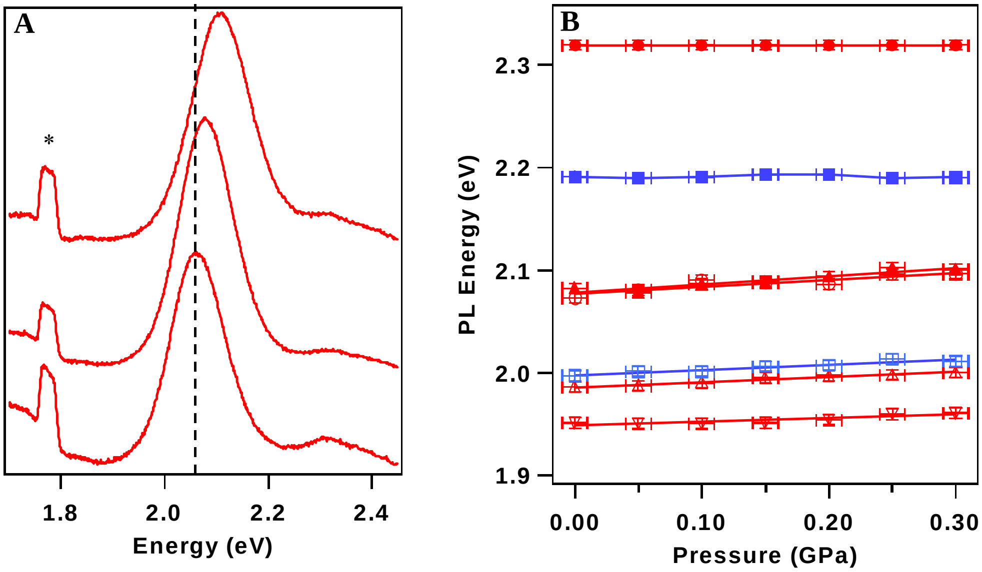

Figure 4.4. Pressure dependent photoluminescence spectra as a function of (A) pressure (for a 22.5 Å radius particle) and (B) CdSe QD radius: (a) 14 Å, (b) 20 Å, (c) 22.5 Å, (d) 27.5 Å, (e) 30 Å, (f) 35 Å, and (g) 40 Å. The spectra were obtained with 2.54 eV laser light; 10 mW power; 298 ± 2 K. The asterisk in Fig. 4.3 represents luminescence from the sapphire windows (in the form of $Cr:Al_2O_3$) in the liquid pressure cell.

meV GPa^{-1}), in agreement with regime *2* behavior for the 14 and 20 Å radius QD. At 22.5 Å radius and above, the PL pressure coefficients exhibit strong pressure dependence as seen in Table 4.1, which follows the expected behavior for systems in regime *1*. Interestingly, the excited state pressure coefficients in regime *1* when $2r > a_o$ approach the reported absorption pressure coefficients (37 meV GPa^{-1}) rather than the reported PL pressure coefficients (58 meV GPa^{-1}).[23, 24] This observation suggests either STE or defect levels in bulk CdSe may contribute to the larger observed PL pressure coefficient in comparison to that of the absorption value. Coupled to the shift of the PL, the full width at half maximum (FWHM) for the PL band increases approximately 30% (~ 125 meV to ~ 185 meV). This is similar to high-pressure studies on InP QDs [14] and is most likely due to population distribution effects rather than size dispersity effects as it occurs in all samples studied. The pressure induced changes in the PL of the CdSe QDs may arise from either a core structural reconstruction or from coupling to localized lattice defects, as has been observed previously in metal nanoparticles. [20] Based on the small shifts in the bulk modulus for CdSe with pressure and the observation of little participation of structural perturbations in high-pressure optical studies of CdSe, structural reconstruction is most likely a minimal contributor to the observed pressure

Table 4.1. Excited state pressure coefficients of CdSe QDs at room temperature (298 ± 2 K)

QD radius (Å)	dE^*/dp (meV^{-1} GPa^{-1})
14	0
20	0
22.5	82
27.5	69
30	51
35	50
40	40
bulk	37[a] 58[b]

dependent PL behavior in this study. [6, 9] This suggests that the observed PL properties may arise from D/A state coupling as theoretically predicted. [1]

Using the models developed for metal nanoparticles [18, 25], a semi-quantitative understanding of the observed pressure dependent tuning of the PL in CdSe QDs can be gained. In Figure 4.5, a plot of dE^*/dp vs. QD radius (r) fits to a phenomenological equation (Eq 4-2), which scales with the particle size

$$\frac{\partial E_{obs}}{\partial p} = ar + \frac{b}{r} \qquad (4\text{-}2)$$

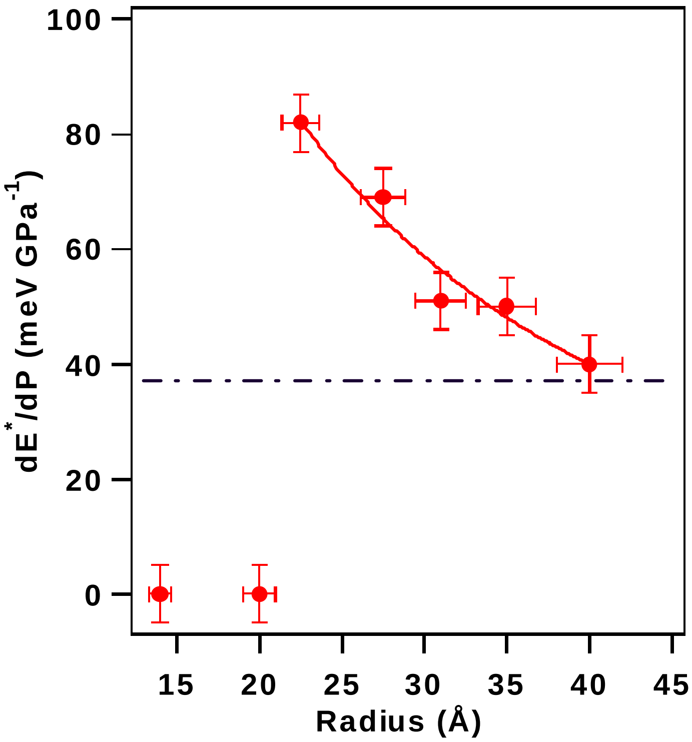

Figure 4.5. Size dependent excited state pressure coefficients as a function of CdSe QD radius. Note the break between 20 and 22.5 Å explained by strong confinement properties of the QD (see text). The dashed line refers to the bulk CdSe pressure coefficient of 37 meV GPa^{-1} (Ref. 23).

r is the particle radius, a is a scalar which is proportional to $[(dE/dp)_{core}][1/a_o]$, $1/b$ can be regarded as an effective electron scattering term that occurs from a highly localized polaronic type defect on the nanoparticle surface, [20] and $(dE/dp)_{core}$ is the bulk pressure coefficient. The scattering term, $1/b$, may be inversely related to the effective polaron length in these materials. [18] The expression in eq. 4-2 indicates that the pressure coefficient will deviate from bulk values at small particle sizes due to contribution from b and deviations from bulk values will be minimized at larger particle sizes as $r \rightarrow a_o$. This is consistent with the observation of the PL properties of the QD being modulated by a localized polaronic defect, which tend to decouple from the core levels at higher pressure for systems at the limit of $r < a_o$. Evidence for a highly delocalized polaron can be gained by inspection of the pressure dependent resonance Raman spectra.

QD radius (Å)	ω_{LO} (cm^{-1})	α (cm^{-1} GPa^{-1})	γ_{LO}
20	212.8	3.51	0.61
22.5	212.4	3.43	0.60
27.5	212.4	6.12	1.00
30	211.7	5.65	0.99
35	212.0	5.37	0.94

4.4. Size Dependent Electron-Phonon Coupling In CdSe QDs

The magnitude of the perturbation to the core excitonic properties will depend both on the defect type and depth, and the contribution from the materials' core *el-ph* coupling. The degree of *el-ph* interactions in the condensed phase is reflected in the ionicity of the material and can be analyzed by calculation of the mode Grüneisen parameters (γ_i). The γ_i parameter can be analyzed by probing the pressure dependent shifts in the vibrational parameters, *i*, of the core levels. [26] As lattice covalency increases, the magnitude of *el-ph* interactions leads to an increase in the contribution of defect perturbations of the excitonic levels.

Table 4.2. Pressure dependence of the CdSe LO phonon at room temperature (298 ± 2 K).

The values of the mode frequency ω_{LO}, α, and LO mode Grüneisen parameter γ_{LO} were extrapolated at ambient conditions. Resonance Raman experiments allow the direct analysis of *el-ph* interactions in materials by probing the cross section for coupling between the vibrational and electronic levels of a system. [27-29] In the resonance condition, excitation of a $1P_h1P_e$ transition at 2.54 eV in CdSe allows the longitudinal optical (LO) phonon modes coupled to the excited state to be probed.

Pressure dependent resonance Raman experiments below the structural phase transition in CdSe QDs exhibit a pressure dependent shift in the core LO phonon and an apparent loss of intensity of the defect (polaron) localized vibration for CdSe (Fig. 4.6a). The fundamental LO mode for CdSe is observed at ~ 210 cm^{-1} with a shoulder to lower frequency. Although band asymmetry is best described as a result of phonon confinement, recent analysis of the asymmetry of the $\mathbf{k} = 0$ LO phonon mode in CdSe QDs has assigned as arising from a localized defect LO mode which couples to the excited state properties of the QD. [20] As reported previously, this allows the observed phonon to be deconvoluted as a contribution of core (~ 210 cm^{-1}) and defect (polaron) (~ 190 cm^{-1}) modes. [20] Overtone modes in this experiment are obscured by photoluminescence from the sample and pressure cell interference. Size dependent hardening of the LO phonon with pressure is observed for CdSe as seen in Fig. 4.6b. The observed vibrational pressure coefficients ($d\omega_{LO}/dp$) are plotted in Table 4.2 and calculated from Fig. 4.6b using a least squares fit to the data (Eq 4-3),

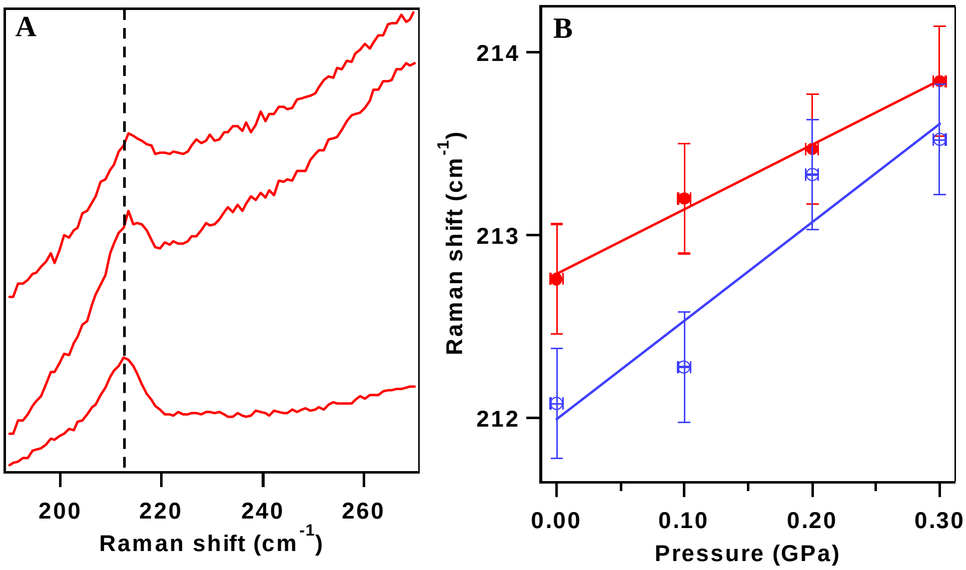

Figure 4.6. Pressure dependent resonance Raman as a function of (A) pressure (for a 30 Å radius particle) and (B) CdSe QD radius: (a) 20 Å and (b) 35 Å. The spectra were obtained with 2.54 eV laser light; 80 mW power; 298 ± 2 K.

$$\omega = \omega_{LO} + \alpha p \qquad \text{(4-3)}$$

where ω_{LO} is the ambient pressure LO phonon frequency, α is the vibrational pressure coefficient, and p is pressure in GPa.

Based on the calculated vibrational pressure coefficients, the LO mode Grüneisen parameters [30] exhibit two specific size regimes for CdSe ($r \leq 22.5$ Å and $r \geq 28$ Å), which correlate with calculations for *el-ph* coupling strengths in CdSe QDs by Melnikov and Fowler (Fig. 4.7). [4] These calculations were performed by considering an electron that is confined in a sphere of radius, *r*, and is interacting with LO phonons of the system. The total Hamiltonian, *H*, of this interaction can be written as,

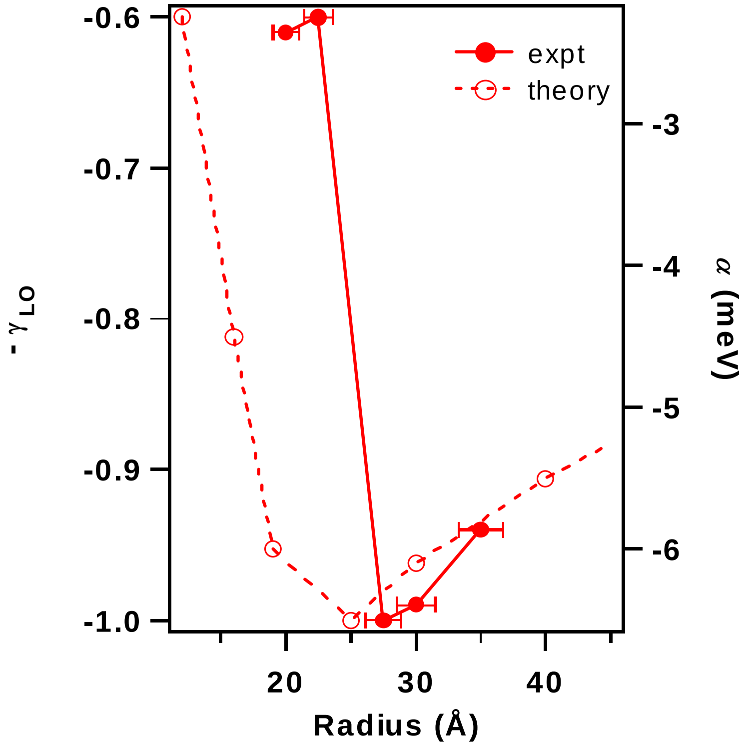

Figure 4.7. Correlation of LO mode Grüneisen parameters (γ_{LO}) and values of the electron-phonon coupling strength, α, (in units of meV) calculated in Ref. 4 as a function of CdSe QD radius. The values for γ_{LO} are plotted as $-\gamma_{LO}$ to emphasize the correlation of γ_{LO} with α. The lines are guide to the eyes.

$$H = H_e + H_{ep} \tag{4-4}$$

where H_e is the electronic Hamiltonian and H_{ep} is the *el-ph* Hamiltonian. The electronic Hamiltonian is given by,

$$H_e = \frac{p^2}{2m} + V_{QD}(r_e) \tag{4-5}$$

where p, m, and r_e are the momentum, effective mass, and coordinate of the electron, respectively. The QD wave function can be written as,

$$\left|\Psi\right\rangle = \left|\psi(r_e)\right\rangle U_1 U_2 \left|0\right\rangle \tag{4-6}$$

where $\left|\psi(r_e)\right\rangle$ is the electronic wave function and $U_1 U_2 \left|0\right\rangle$ is the surface and LO phonon wave function. Using Eq. 4-6, the Hamiltonian in Eq. 4-4 can be solved to obtain the expectation value, E_{ep}. Using variational methods to obtain the correct QD wave function, the *el-ph* energy can be written as,

$$\begin{aligned} E_{ep} &= \frac{[4erN^2]^2}{r}\left(\frac{1}{\varepsilon_\infty} - \frac{1}{\varepsilon_0}\right) \\ &\times \sum_{n=1}^{\infty} \frac{1}{n^2} \left[\int_o^{\pi} dx \frac{\sin(nx)}{x} \sin^2\left(\frac{\zeta r x}{\pi}\right) \exp\left(\frac{-2\gamma r x}{\pi}\right) \right]^2 \end{aligned} \tag{4-7}$$

where N is the wave function normalization constant, ε_o and ε_∞ are the static and high frequency dielectric constants, $\zeta = \sqrt{2mE_o / \hbar^2}$, and γ is a variational parameter which indicates the strength of the *el-ph* interaction. Note that Eq. 4-7 is similar to the expected *el-ph* coupling constant for the Fröhlich interaction in bulk polar crystals. [31]

In Fig. 4.7, the correlation between theoretical and experimental *el-ph* strengths is striking, however, the observation of size dependent Grüneisen parameters show that there is a distinct increase in lattice covalency (and therefore decrease in *el-ph* coupling strength) in the strongly confined regime. This provides further evidence that deviations in *el-ph* interactions exist in this regime, which may give rise to polaronic-type defects, and therefore the observed anomalies seen in the PL experiments.

A more direct method to analyze *el-ph* interactions is to evaluate the pressure dependencies of the LO mode integrated intensities. Although pressure induced changes in the optical cross sections may perturb the resonance enhancement of the Raman experiment, evaluation of the mode intensity ratios of the core LO and polaron defect LO are useful. In our experiments, coupled to the changes in the LO mode with pressure, the localized polaron LO mode exhibits significant loss in the integrated intensity at pressures exceeding 0.1-

0.15 GPa (Fig. 4.8). The observed sharp drop in intensity of this mode is consistent with a first order "electronic phase transition" arising from a change in the *el-ph* coupling between the core and defect states, due to a decrease in resonance between the polaron and core levels resulting in state decoupling. The loss of polaron coupling to core levels may explain the observation of break in linearity at higher pressures arising from complete defect de-coupling and bulk-like behavior, as observed in previous high-pressure studies. [6, 12, 14] The lack of mode hardening of the polaron mode with applied pressure implies an effective mode Grüneisen parameter of zero and is consistent with a strongly localized polaronic state in these materials where *el-el* interactions are dominated by *el-ph* interactions, as predicted in the PL pressure dependent optical properties.

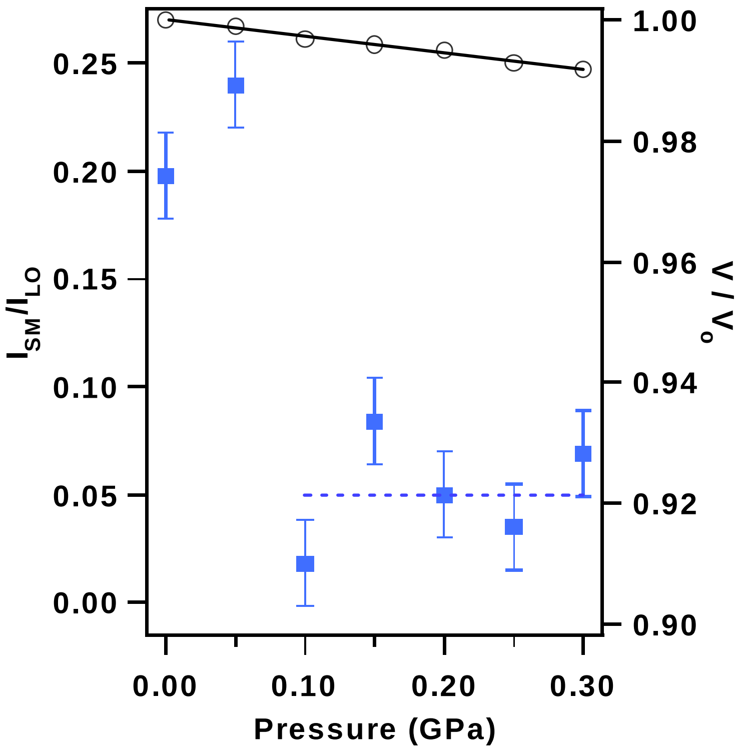

Figure 4.7. Plot of the ratio of the integrated intensities of the surface phonon mode with respect to the LO phonon mode. Note the small change in lattice volume with the large change in $\frac{I_{SM}}{I_{LO}}$. The plot of $\frac{V}{V_o}$ is calculated using the equation, $\frac{V}{V_o} = (1 + \frac{B_o^{'}}{B_o} p)^{1/B_o^{'}}$. The values of $B_o^{'}$ and B_o for bulk CdSe are used and obtained from Ref 11.

4.5. Discussion

4.5.1. Comparison of Theoretical and Experimental Photoluminescence Pressure Results

Using the models developed in Chapter 1 (Section 1.3.2.2), a theoretical prediction on the PL pressure behavior of CdSe QDs can be achieved. As described in Chapter 1, only the bulk and confinement energy terms will be considered here as the Coulomic terms (and other corrections) only contribute at very high pressures. Figure 4.9 shows the calculated and experimental PL energy shift for a 27.5 and 35 Å CdSe QD. Evident from these plots is that in both spectra, the theoretical prediction underestimates the energy shift. The data for the 35 Å QD, however, follows much closer to theory than the data fro the 27.5 Å QD. Therefore, another mechanism must account for the deviation between theory and experiment. The deviation between experiment and theory is listed in Table 4.3. We propose that this deviation is related to an effective stress on the particle, which changes the nature of *el-ph* coupling in the QD, and causes the disparity between experiment and theory. The nature of this effective stress will be described in Chapter 5; for now, the rest of the discussion will focus on the changes in *el-ph* coupling and its effect on the photophysics of CdSe QDs.

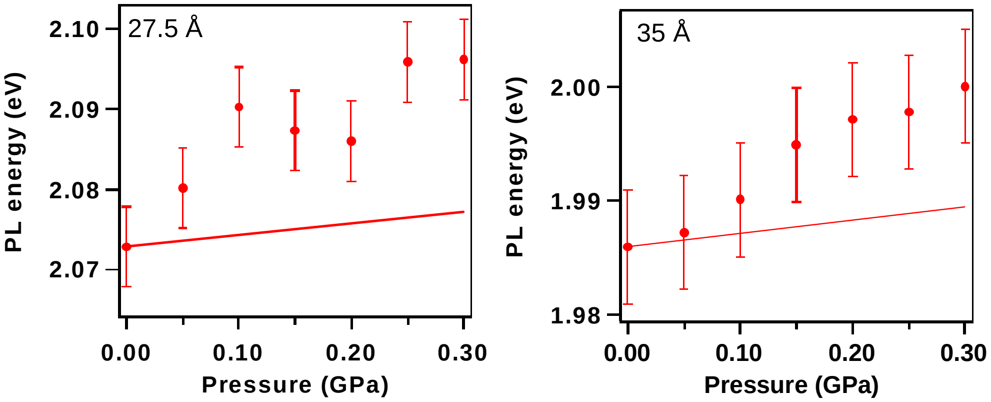

Figure 4.9. Comparison of the theoretical and experimental PL energy shift. The solid line represents the PL energy shift from models described in Chapter 1.

Table 4.3. Theoretical and experimental PL energy shifts at 0.3 GPa. The effective stress is calculated using the observed PL pressure coefficients.

	exp	**theory**		
Radius (Å)	E $_{(P=0.3\ GPa)}$	E $_{(P=0.3\ GPa)}$	$\Delta E_{(exp-theory)}$	P_{eff} (kbar)
14	0	21.2	-21.2	-5.7
20	0	15.6	-15.6	-4.2
22.5	24.6	14.7	9.9	2.7
27.5	20.7	13.5	7.2	1.9
30	15.3	13.1	2.2	0.6
35	15.0	12.6	2.4	0.6
40	11.1	12.2	1.1	0.3
bulk	11.1	11.1	0	0

4.5.2. Characterization of the donor state

In Sec 4.3, the observation of size dependent PL pressure coefficients was attributed to the existence of a donor state that induces polaronic defects in the QD lattice and perturbs the optical properties. To understand the full impact this observation will have on QD physics, the nature of the state must identified. There are a few plausible explanations for this donor state. The first explanation is that it is truly a surface state of the QD system, and thus is a function of only the S:V ratio. For this to hold true, the observed pressure coefficients in *all* QDs should always show a $1/r$ dependence, and may show organic coating dependencies, as the electronic potential of the coating can alter the energy of the surface state. A second explanation is that the observed behavior is dependent on quantum confinement effects (i.e. the extent of the Bohr radius) and should therefore show varying behavior depending on the QD system. A final explanation is that the observed behavior is merely a by-product of the chemical syntheses of the dot. Therefore, there may be defects in some QDs in different colloidal preparations and this could account for the observed behavior. To begin to identify this, the pressure dependence of the PL as a function of coating along with the temperature dependence of the PL has been performed.

In Figure 4.10, the PL as a function of pressure for ~40 Å CdSe is shown. As seen in the plot (and described above), no pressure dependence for

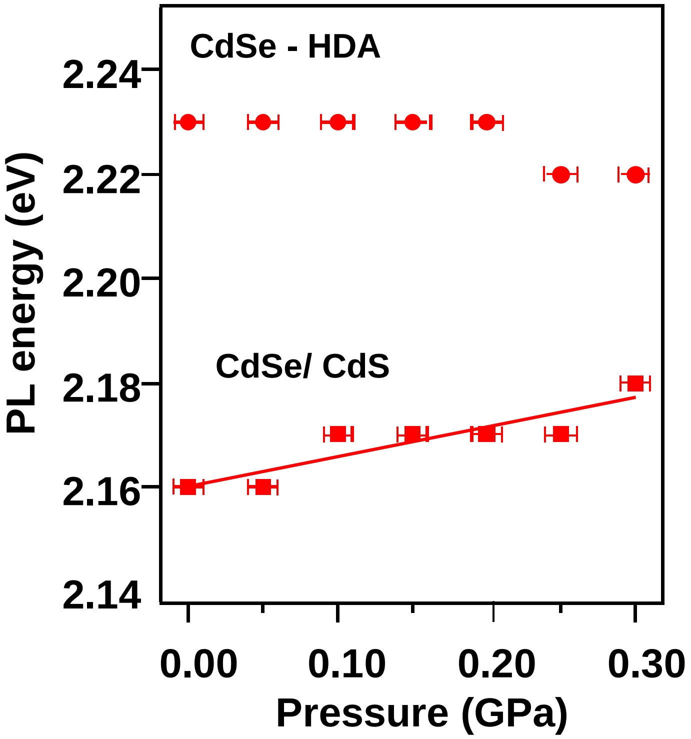

Figure 4.10. Pressure dependent photoluminescence spectra of 22 Å radius CdSe QDs as a function of surface coating. The spectra were obtained with 2.54 eV laser light; 10 mW power; 298 ± 2 K.

the HDA coated materials is seen, however, pressure dependence for the CdS coated dots is observed. The pressure coefficient for the CdSe/CdS QD is 57 meV GPa^{-1}, which is nearly the value obtained from bulk CdSe PL pressure coefficients. In Figure 4.11, the temperature dependence of the PL is plotted for a 55 and 95 Å CdSe QD coated with HDA. The observed temperature coefficients are -0.48 meV K^{-1} and -0.30 meV K^{-1} for the 55 and 95 Å QDs, respectively. Although this data cannot sufficiently assign the nature of this donor state, a few ideas can be generated. First, because the temperature coefficients do show a small, but distinguishable, difference, it can be stated that the state being tuned by temperature in the 55 Å QD is more “mobile” than the state in the 95 Å QD. If the state were simply an internal defect that is present due to an imperfection from the synthesis, then this observation would not occur. It is therefore more likely that dimensional and confinement effects compete in determining the pressure dependent optical properties of QDs. Due to the observation of pressure coefficients in the inorganic capped QD, a confinement or strain effect may be the necessary argument to describe these effects, however, more experiments are needed to verify this.

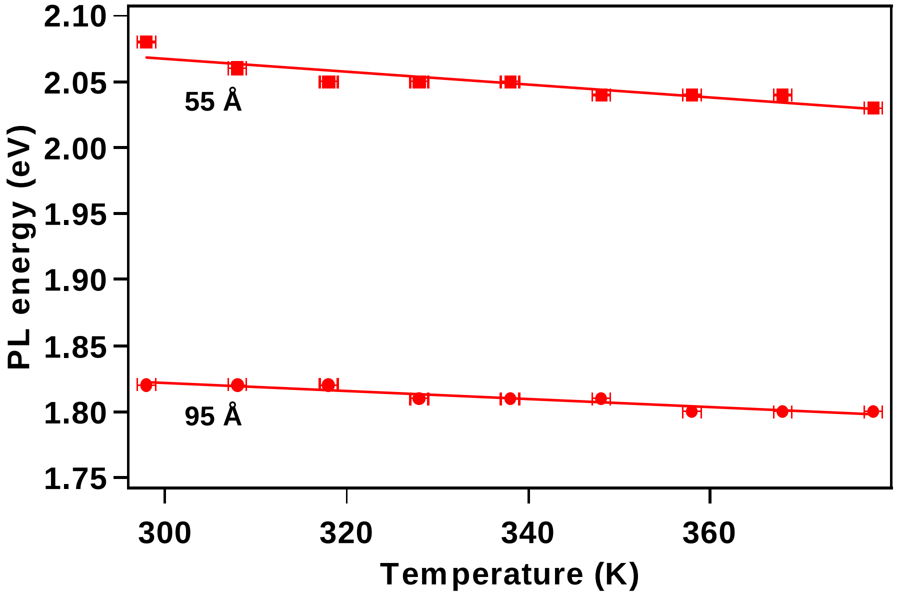

Figure 4.11. Temperature dependent ($p = 1$ atm) photoluminescence spectra of CdSe QDs as a function of size. The spectra were obtained with 2.54 eV laser light; 10 mW power.

4.5.2. Correlation of the PL and Raman data

Analysis of the CdSe size-dependent Grüneisen parameters calculated from the pressure dependent vibrational properties in Figure 4.7 and Table 4.2 suggests a significant level of perturbation exists in the lattice for QDs in the strongly confined limit ($r \leq a_o$). We note that these observed anomalies leading to the observed perturbations are not a function of pressure induced melting events (eg, the organic surfactant), as only ~ 0.5 meV (~ 0.05 kJ mol^{-1}) of energy is generated from the application of these modest pressures. As seen in Fig. 4.6, above 56 Å ($r = 28$ Å), as the particles go from the strongly to the moderately confined limit, the QDs begin to approach the bulk value for γ_{LO}. As the particle size is decreased, the value for γ_{LO} reaches a maximum, which indicates a fairly ionic lattice. This increase in ioniciy should lead to an increase in *el-ph* coupling, and this assessment is verified by calculations on

CdSe QDs by Melnikov and Fowler who show the *el-ph* interaction energy minimizes at $r \sim 25$ Å.[4] As the particle size is decreased ($r < 25$ Å), Melnikov and Fowler find that the *el-ph* energy again begins to rise, indicating destabilization of the coupling strength. This correlates with the observed size dependence in γ_{LO}. At small particle sizes, we observe a large decrease in γ_{LO} which indicates an increase in lattice covalecy and a corresponding decrease in the *el-ph* coupling strength. The shift in the magnitude of γ_{LO} correlates with the size dependence observed in the PL spectroscopy, suggesting the perturbation most likely arises from a modulation of the level of *el-ph* coupling in these materials as a function of size, which correlates with the degree of defect-core level coupling in the PL spectroscopy. The enhanced coupling in regime *1* materials may arise from the strong mixing of the core and defect atoms due to a large ratio of surface to volume (~40%) atoms in the nanocrystal. The lack of pressure behavior in this regime may also be attributed to quantum mechanical effects, as the *el-h* exchange interaction in this size range is comparable to *kT* (25 meV) therefore causing the emitting state to consist primarily from the ±2 exciton state, which may show a different pressure response than the thermally averaged $\pm1^L$, 0^L, and ±2 emitting states. Interestingly, this breakpoint in γ_{LO} and in the observed dE^*/dp arises at the breakpoint for the contribution of the kinetic energy term in the particle-in-the-box model for the size dependent absorption[32], as well as the size-regime for thermodynamic stabilization of these materials arising from chain interactions that govern the QD surface. [33, 34] More importantly, the size dependence of the pressure coefficients tend to extrapolate to the bulk absorption pressure coefficient which implies that our large QDs are highly crystalline with little defects and the excited state of these materials favor a delocalized model, as proposed by Efros and co-workers. [1]

4.6. Conclusions

As predicted, QDs exhibit two pressure dependent regimes for polaron coupling to core levels. As witnessed in previous high pressure experiments, the application of extreme pressures tend to de-couple the polaron, and the materials exhibit pressure dependencies analogous to their bulk counterparts. The interpretation of our results suggests that low pressures are needed to probe these polaronic interactions and to observe size dependent scaling laws related the optical properties of the QD. The adiabaticity of a quantum dot band structure can be thought of in terms of a strongly crossing and avoiding model and scales as a phenomenological expression related linearly with the bulk pressure properties and inversely with the surface properties, as expected for a system with a S:V ratio that scales as $1/r$ (Fig. 4.3). The pressure coefficient trends for the PL and vibrational terms indicate the largest tuning of the electronic levels at low pressure arise for QDs approaching the size of the

Bohr exciton radius. The increase of lattice covalency, measured from the size dependent Grüneisen parameters, provides evidence that the polaron arises from increased *el-ph* interactions in these materials. Further studies into the pressure tuning other II-VI and III-V materials are underway to test the models proposed in this chapter.

4.7. References

1 A. L. Efros and M. Rosen, Annual Review of Materials Science **30**, 475 (2000).

2 D. V. Melnikov and W. B. Fowler, Physical Review B **6316**, 5302 (2001).

3 D. V. Melnikov and W. B. Fowler, Physical Review B **64**, 195335 (2001).

4 D. V. Melnikov and W. B. Fowler, Physical Review B **6424**, 5320 (2001).

5 S. H. Tolbert, A. B. Herhold, C. S. Johnson, *et al.*, Physical Review Letters **73**, 3266 (1994).

6 S. H. Tolbert and A. P. Alivisatos, Journal of Chemical Physics **102**, 4642 (1995).

7 S. H. Tolbert, A. B. Herhold, L. E. Brus, *et al.*, Physical Review Letters **76**, 4384 (1996).

8 C. J. Lee, A. Mizel, U. Banin, *et al*., Journal of Chemical Physics **113**, 2016 (2000).

9 J. B. Li, G. H. Li, J. B. Xia, *et al*., Journal of Physics-Condensed Matter **13**, 2033 (2001).

10 B. S. Kim, M. A. Islam, L. E. Brus, *et al*., Journal of Applied Physics **89**, 8127 (2001).

11 H. X. Fu, L. W. Wang, and A. Zunger, Physical Review B-Condensed Matter **59**, 5568 (1999).

12 J. Schroeder and P. D. Persans, Journal of Luminescence **70**, 69 (1996).

13 M. Nirmal, D. J. Norris, M. Kuno, *et al*., Physical Review Letters **75**, 3728 (1995).

14 C. S. Menoni, L. Miao, D. Patel, *et al*., Physical Review Letters **84**, 4168 (2000).

15 S. L. Cumberland, K. M. Hanif, A. Javier, *et al*., Chemistry of Materials **14**, 1576 (2002).

16 D. R. Dawson and H. W. Offen, Review of Scientific Instruments **51**, 1349 (1980).

17 B. Y. Okamoto and H. G. Drickamer, Journal of Chemical Physics **61**, 2870 (1974).

18 J. Z. Zhang, Accounts of Chemical Research **30**, 423 (1997).

19 M. Nirmal and L. Brus, Accounts of Chemical Research **32**, 407 (1999).

20 Y. N. Hwang, S. H. Park, and D. Kim, Physical Review B-Condensed Matter **59**, 7285 (1999).

21 W. S. Hammack, M. D. Lowery, D. N. Hendrickson, *et al.*, Journal of Physical Chemistry **92**, 1771 (1988).

22 G. L. House and H. G. Drickamer, Journal of Chemical Physics **67**, 3230 (1977).

23 A. L. Edwards and H. G. Drickamer, Physical Review **122**, 1149 (1961).

24 J. R. Mei and V. Lemos, Solid State Communications **52**, 785 (1984).

25 B. A. Smith, J. Z. Zhang, U. Giebel, *et al.*, Chemical Physics Letters **270**, 139 (1997).

26 M. Cardona and G. Güntherodt, *Light scattering in solids IV : electronic scattering, spin effects, SERS, and morphic effects* (Springer-Verlag, Berlin ; New York, 1984).

27 G. F. Strouse, B. Scott, B. I. Swanson, *et al.*, Chemical Physics Letters **289**, 559 (1998).

28 D. N. Argyriou, H. N. Bordallo, B. J. Campbell, *et al.*, Physical Review B **61**, 15269 (2000).

29 H. N. Bordallo, R. W. Henning, L. P. Sosman, *et al*., Journal of Chemical Physics **115**, 4300 (2001).

30 LO mode Grüneisen parameters are calculated using the equation $\gamma_{LO} = \frac{B_o}{\omega_o} \frac{\partial \omega_{LO}}{\partial p}$.

31 A. M. Stoneham, *Theory of Defects in Solids* (Clarendon Press, Oxford, 1975).

32 L. E. Brus, Journal of Chemical Physics **80**, 4403 (1984).

33 R. W. Meulenberg and G. F. Strouse, Journal of Physical Chemistry B **105**, 7438 (2001).

34 R. W. Meulenberg, S. Chaney, C. S. Yun, *et al*., Journal of Physical Chemistry B **106**, 7774 (2002).

Chapter 5: Compressive and Tensile Stress in Colloidal CdSe Semiconductor Quantum Dots

5.1. Introduction

Semiconductor nanocrystals, or quantum dots (QDs), are a class of solid-state materials whose physical properties are strongly dependent on the spatial dimensions of the particle. [1] These QDs can be prepared via molecular beam epitaxial methods [2] or by using wet colloidal chemical techniques. [3] For particle radii close to the Bohr exciton of the material, quantum confinement effects dominate the optical and electronic properties of these materials. [4] In addition to confinement effects, dimensional size effects can drastically alter the surface atom bonding [5] and passivant crystallinity [6] leading to surface reconstruction and lattice contraction, which can be related to the surface energy changing as a function of particle size. [7] What is not fully understood, however, is the change in the surface energy and lattice strain as the QD chemical synthesis is altered. An ideal experimental method to observe lattice strain is Raman spectroscopy. [8] For a dimensionally confined crystal, the competition between strain and confinement can have a drastic impact on the absolute energy of the optical phonons. [8] When the crystal experiences tensile stress or phonon confinement effects, the optical phonon energies shift to the red, while a crystal under compressive stress is expected to show a blue shift of the optical phonon. In this letter, shifts in the LO phonon mode in CdSe QDs, measured by resonance Raman spectroscopy, is interpreted as arising from size dependent surface strain differences in chemical preparations in CdSe and CdSe/ZnS core-shell QDs. Interestingly, the strain, reported in terms of tensile and compressive stress, changes as a function of chemical preparative routes.

5.2. Experimental

CdSe and CdSe/ZnS core-shell QDs were synthesized by known literature methods using either a single source precursor route based on a $Cd_{10}Se_4(C_6H_5)_{16}^{4-}$ cluster with *n*-hexadecylamine (HDA) or Me_2Cd routes with trioctylphosphine oxide (TOPO) as the growth solvent. [3, 9] Crystallinity and size dispersity of the produced materials are ~6% and can be monitored by UV-Vis absorption, x-ray diffraction, and transmission electron microscopy analysis. For the optical experiments, the samples were either pressed as a solid pellet, cast as a thin film, or dispersed in organic solvents. In the case of small particle sizes, pyridine was added to minimize background luminescence from the sample by inducing quenching of the luminescence. No differences were seen in the vibrational frequencies with the QDs measured either as a solid versus or in polar organic solvents, and is consistent with a previous study. [10] The resonance Raman experimental set-up has been described elsewhere. [11] Laser powers of less than 60 mW were used to minimize sample degradation. Wave number calibration was obtained by using elemental sulfur. A polarization descrambler was inserted prior to the entrance slit of the monochromater to avoid spectrometer polarization dependencies.

5.3. Results and Discussion

Figure 5.1 shows the size dependent resonance Raman spectra between 200-600 cm^{-1} of HDA (Fig. 5.1a), TOPO (Fig. 5.1b), and CdSe/ZnS (Fig. 5.1c) grown CdSe QDs. The spectra consists of a strong mode centered at ~210 cm^{-1} arising from the longitudinal optical (LO) phonon with a weaker mode arising from the second order LO (2LO) appearing at ~415 cm^{-1}. [12] No evidence for the third order LO is seen, although a previous study has observed it. [10] The general trend of the data shows a softening of the LO phonon as particle size is decreased which can be attributed to phonon confinement (PC) effects and it consistent with previous Raman studies on CdSe QDs. [10, 12, 13] Intriguingly, a plot of the size dependent LO for different samples produces a different magnitude of shift (Fig. 5.2), suggesting a variance in the nature of confinement.

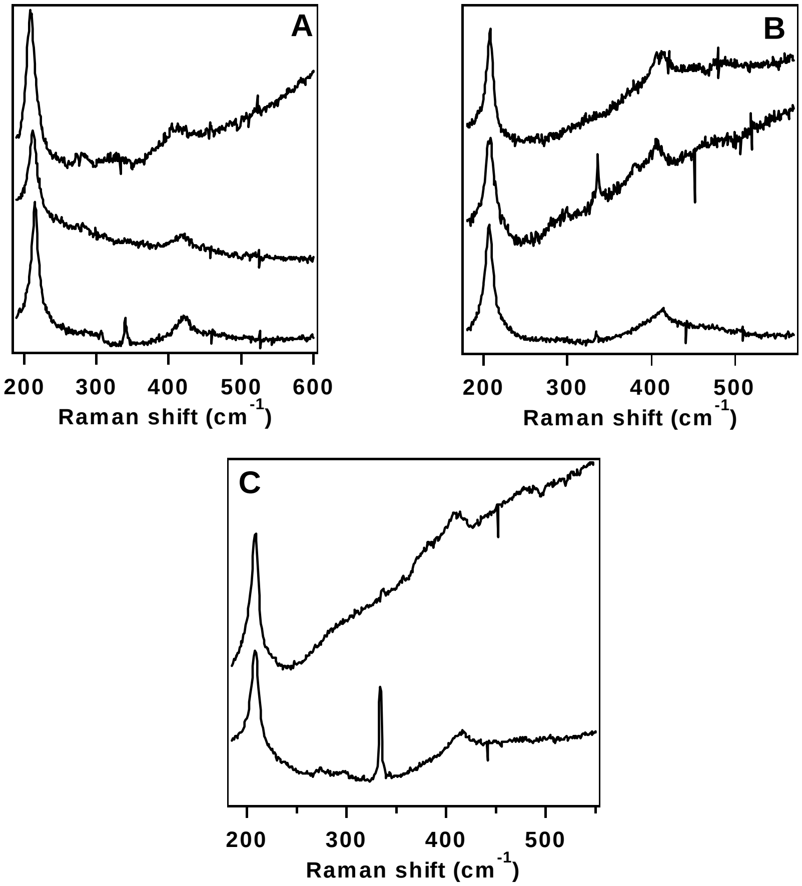

Figure 5.1. Resonance Raman spectra (2.54 eV excitation) between 200-600 cm^{-1} of (A) HDA coated, (B) TOPO coated, and (C) ZnS overcoated CdSe QDs.

As a result of PC, the phonon wave function becomes finite and therefore the $\mathbf{q} = 0$ selection rule relaxes. This allows phonon modes from wider range in the Brillouin zone to contribute to the Raman spectrum. If the phonon wave function is described by $\Phi(\mathbf{q}_o,\mathbf{r}) = u(\mathbf{q}_o,\mathbf{r})e^{i\mathbf{qr}}$, where $u(\mathbf{q}_o,\mathbf{r})$ has the periodicity of the lattice, then PC will modify the phonon wave function to, $\Psi(\mathbf{q_o},\mathbf{r}) = W(\mathbf{r},L)\Phi(\mathbf{q_o},\mathbf{r}) = \Psi'(\mathbf{q_o},\mathbf{r})u(\mathbf{q_o},\mathbf{r})$, where $W(\mathbf{r}, L)$

Table 5.1. Theoretical and experimental LO phonon shift from the bulk LO value. Here the CdSe radius in measured in Å, $\Delta\omega_{\mathrm{PC}}$ is the difference between the calculated LO mode frequency based on the phonon confinement model and the bulk value in cm^{-1}, $\Delta\omega_{\mathrm{exp}}$ is the difference between the experimental LO mode frequency and the bulk value in cm^{-1}, $\Delta\omega_{\mathrm{diff}}$ is $\Delta\omega_{\mathrm{PC}}$ - $\Delta\omega_{\mathrm{dexp}}$ in cm^{-1}, and P_{eff} is the effective pressure in GPa.

CdSe radius	$\Delta\omega_{\mathrm{PC}}$	$\Delta\omega_{\mathrm{exp}}$	$\Delta\omega_{\mathrm{diff}}$	P_{eff}
30[a]	3.1	2.97	0.13	0.02
27.5[a]	4.1	3.81	0.29	0.03
20[a]	7.1	5.59	1.51	0.40
17[a]	10.6	7.70	2.9	0.80
35[b]	2.6	3.17	-0.57	-0.16
25[b]	4.6	7.00	-2.4	-0.39
21.5[b]	6.6	8.97	-2.37	-0.69

[a] HDA coated CdSe
[b] TOPO coated CdSe

is a weighting function. If the perturbed wave function, Ψ', is expanded into a Fourier series, and if a Gaussian weighting function centered at $\mathbf{q_o}$ is considered, the Fourier coefficient becomes $|C(0,\mathbf{q})|^2 \sim \exp(-L^2 q^2/2\alpha)$, where α is dependent on the crystal type. The one-phonon Raman spectra can then be calculated by, [14]

$$I(\omega, L) = \frac{L^3}{2\pi^{3/2}} \int_0^1 \frac{|C(\mathbf{0},\mathbf{q})|^2}{[\omega - \omega(\mathbf{q})]^2 + \left(\Gamma/2\right)^2} dq \qquad (5\text{-}1)$$

where $\omega(\mathbf{q})$ is the bulk phonon dispersion relation and Γ is the natural linewidth. For CdSe, the bulk LO phonon dispersion relation is $\omega(\mathbf{q}) = 213.1$ (cm^{-1}) – $125.3\mathbf{q}^2$ and $\Gamma = 2$ cm^{-1}. [15] This allows phonon confinement effects to be estimated quantitatively in terms of the phonon correlation length, L, which corresponds to the size of phonon confinement within the nanocrystal.

The differences in the theoretical and experimental values are listed in Table 5.1, where the theoretically predicted LO phonon shifts from the phonon confinement model are tabulated along with the observed experimental LO phonon shifts. The strain effects are reported as an effective compressive (positive) or tensile (negative) stress term. Although stress is a tensorial quantity, [17] the value for the stress listed in Table 5.1 represent spatially

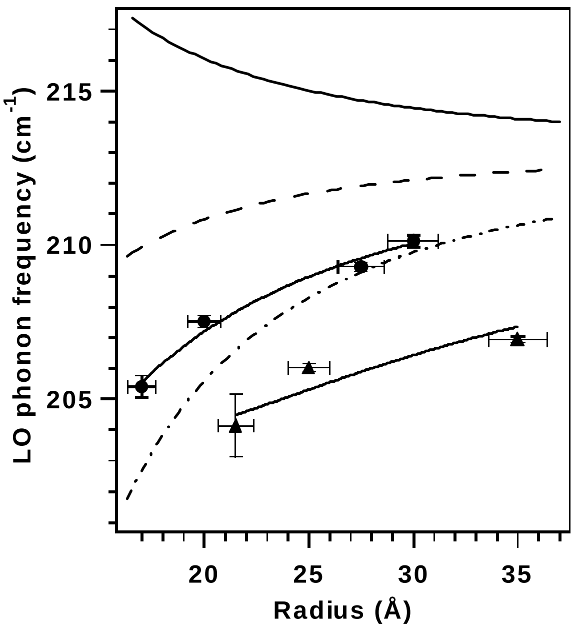

Figure 5.2. Size dependent LO phonon for HDA (■) and TOPO (▲) coated CdSe QDs. The solid line represent the theoretical LO dispersion based only on surface tension (strain), the dashed-dot line represents the theoretical LO dispersion based only on phonon confinements, and the dotted line in the theoretical LO dispersion based upon contribution from surface tension and phonon confinement. The solid lines through the experimental points represent least squares fits of the points to Eq. 5-4.

averaged stress due to the isotropic nature of the ordering of QDs in solution and films. Figure 5.2 plots the size dependent LO as a function of CdSe particle radius passivated with HDA and TOPO. As seen from the plot, the dispersion of the LO mode for the CdSe-HDA nearly tracks the calculated LO mode dispersion with a deviation at small particle sizes. The scaling law obtained from a power law fit of the data of the LO mode for the CdSe-HDA is proportional to R^{-2}. This is the same as the observed R^{-2} scaling law for CdSe QDs embedded in borosilicate glass. [13] The LO mode dispersion for the CdSe-TOPO deviates much more from the theoretical values than the CdSe-HDA samples, and follows a scaling law proportional to R^{-1}.

Deviations between experimental and theoretical shifts in the PC are proposed to arise from strain in the QD lattice. This interpretation has previously been used to describe the Raman spectra of CdSe QDs embedded in glass as well as free standing CdSe QDs formed by high temperature pyrolysis of CdO. [16] To gain a quantitative understanding on why the two chemical preparations would exhibit such different physics, the effect of stress must be included in the PC model by introducing a stress dependent LO frequency term. Strain can be modeled as an internal pressure, allowing the application of an experimentally derived pressure dependent LO phonon, $\omega = \omega_{\mathrm{LO}} + \alpha P$, where ω_{LO} is the LO frequency at ambient pressure, α is the LO phonon pressure coefficient, and P is the strain induced pressure. If the observed stress is assumed to arise from surface tension, the internal stress, P, can be described by,

$$P = \frac{2\gamma(R)}{R} \tag{5-2}$$

where $\gamma(R) = A + B\,R^{-2}$ and represents the size dependent surface tension [7] and R is the particle radius. Using the pressure dependent LO frequency term and eq. 5-2, the size dependent surface tension can be related to the LO frequency by,

$$\omega = \omega_{LO} + \frac{2\alpha}{R}\left(A + \frac{B}{R^2}\right) \tag{5-3}$$

with *A* and *B* related to the surface tensions of flat and "curved" faces of the QD, respectively. Incorporating the effect of phonon confinement, eq. 5-3 can be written as,

$$\omega = \omega_{LO} + \frac{2\alpha}{R}\left(A + \frac{B}{R^2}\right) - \frac{C}{R^2} \tag{5-4}$$

where *C* is a constant related to the strength of phonon confinement. In the fitting procedure described next, the values for ω_{LO}, α, and *C* were held constant and were 213.1 $\mathrm{cm^{-1}}$, 4.26 $\mathrm{cm^{-1}\ GPa^{-1}}$, [18] and 3008.6 $\mathrm{cm^{-1}}$ $\mathrm{Å^{2}}$. [19]

The solid lines in Fig. 5.2a for both the HDA and TOPO samples represent a least squares fits of the data to Eq. 5-4. From the fits in Fig. 5.2a, the constants *A* and *B* can be obtained, which are representative of the surface tension of the QD. The values obtained for CdSe-HDA and CdSe-TOPO are $A = 0.12\ \mathrm{Nm^{-1}}$, 1.8 $\mathrm{Nm^{-1}}$ and $B = 198\ \mathrm{Nm^{-1}Å^{-2}}$, 610 $\mathrm{Nm^{-1}Å^{-2}}$, respectively. The value of $A = 0.12\ \mathrm{Nm^{-1}}$ for the CdSe-HDA QDs has been previously reported as a reasonable value for a low-indexed face of the wurtzite QD. [7] The observation of $A = 1.8\ \mathrm{Nm^{-1}}$ for the CdSe-TOPO samples is a surprising result, as it is slightly higher than the value obtained in Ref. 7. This may be an indication of glide plane or vacancy defects in the QDs grown in high temperature conditions, since it has been suggested that there exists stacking faults in the low-pressure phase of CdSe-TOPO QDs. [20] The values of B are nearly a factor of three higher for the CdSe-TOPO samples indicating that the energy required to curve the surfaces of the CdSe-TOPO QDs is much higher than the CdSe-HDA samples. Possible reasons for this behavior are described below.

Figure 5.3 shows the compressive stress values obtained for the CdSe-HDA QDs as a function of particle radius. The compressive stress varies from nearly 8 kbar (0.8 GPa) at small particle sizes down to 0.3 kbar (0.03 GPa) at larger particle sizes. Fig. 5.3 also plots the effective compressive stress obtained from Ref. 11 and the values show good agreement with the derived values from the Raman spectra in this letter. The solid line in Fig. 5.3 represents the calculated surface stress obtained from Eq. 5-6 using the size dependent surface tension, $\gamma(R)$. The agreement between the theoretical surface stress and the experimentally derived surface stress indicates that the compressive stress in the CdSe-HDA QDs is solely due to a surface effect. The CdSe-TOPO samples do not follow a smooth relationship, implying that the size dependent tensile stress is not purely due to the surface. We propose that the tensile stress arises from vacancies and vacancy clusters that are trapped kinetically in the growth process. We note that the mechanism is valid only for the CdSe-TOPO samples, as the CdSe-HDA growth is

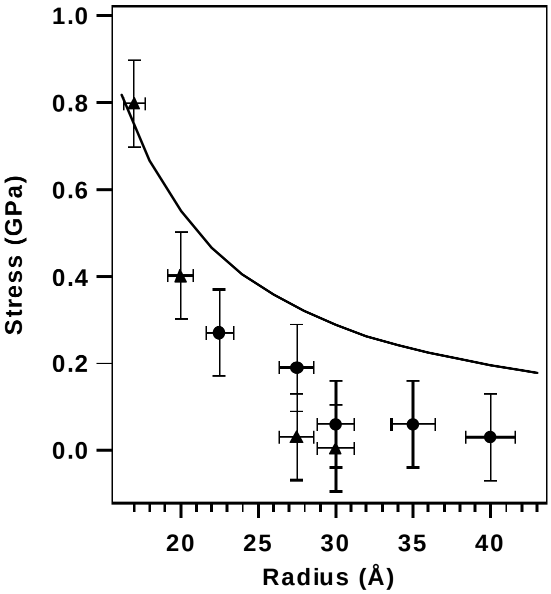

Figure 5.3. Compressive stress as a function of particle size for CdSe-HDA QDs.

thermodynamically controlled and most likely arises from the molecular clusters adding in a stepwise fashion, with very little possibility for defects. [3] This mechanism is supported in the Raman data in Fig. 5.2, where the LO dispersion for the CdSe-HDA samples follow very closely to the PC model indicating that these samples represent nearly defect free, strongly confined materials. To understand the tensile stress in the CdSe-TOPO samples, the particles were passivated with an inorganic shell (ZnS). The lattice mismatch between CdSe and ZnS is ~11%, therefore we expect a large distortion will occur for the surface and near surface of the QD. Figure 5.1c shows the difference between ~25 Å radius QDs passivated with TOPO and ZnS. The observed shift in the data in Fig. 5.1c is ~+2 cm^{-1}. This corresponds to a compressive stress of 3.1 kbar (0.31 GPa). The observed compressive stress due to the ZnS shell for the 21.5 Å CdSe sample is 5.4 (0.54 GPa), which is significantly larger than the 25 Å QD. The larger value of compressive stress in the 21.5 Å QD indicates that the relative lattice mismatch between the core and shell is greater in the smaller QD. This could be due to the presence of internal defects that distort the lattice. As the particle size increase, the number of defects decrease, and the relative lattice mismatch decreases.

5.4. Conclusions

In summary, compressive and tensile stress in CdSe QDs was studied by resonance Raman spectroscopy. The experiments prove that there exist distinct differences in the physics of QDs prepared by different chemical methods. These studies suggest that the differences in chemical preparation of QDs will greatly impact the future advance of device technology based on nanomaterials.

5.5. References

1 N. F. Johnson, Journal of Physics-Condensed Matter **7**, 965 (1995).

2 J. C. Kim, H. Rho, L. M. Smith, H. E. Jackson, S. Lee, M. Dobrowolska, J. L. Merz, and J. K. Furdyna, Applied Physics Letters **73**, 3399 (1998).

3 S. L. Cumberland, K. M. Hanif, A. Javier, G. A. Khitrov, G. F. Strouse, S. M. Woessner, and C. S. Yun, Chemistry of Materials **14**, 1576 (2002).

4 A. P. Alivisatos, Journal of Physical Chemistry **100**, 13226 (1996).

5 K. S. Hamad, R. Roth, J. Rockenberger, T. van Buuren, and A. P. Alivisatos, Physical Review Letters **83**, 3474 (1999).

6 R. W. Meulenberg, S. Bryan, C. S. Yun, and G. F. Strouse, Journal of Physical Chemistry B **106**, 7774 (2002).

7 S. H. Tolbert and A. P. Alivisatos, Journal of Chemical Physics **102**, 4642 (1995).

8 H. Rho, H. E. Jackson, S. Lee, M. Dobrowolska, and J. K. Furdyna, Physical Review B **61**, 15641 (2000).

9 C. B. Murray, D. J. Norris, and M. G. Bawendi, Journal of the American Chemical Society **115**, 8706 (1993).

10 A. P. Alivisatos, T. D. Harris, P. J. Carroll, M. L. Steigerwald, and L. E. Brus, Journal of Chemical Physics **90**, 3463 (1989).

11 R. W. Meulenberg and G. F. Strouse, Physical Review B **6603**, U480 (2002).

12 A. P. Alivisatos, T. D. Harris, L. E. Brus, and A. Jayaraman, Journal of Chemical Physics **89**, 5979 (1998).

13 Y. N. Hwang, S. H. Park, and D. Kim, Physical Review B-Condensed Matter **59**, 7285 (1999).

14 H. Kohno, T. Iwasaki, Y. Mita, and S. Takeda, Journal of Applied Physics **91**, 3232 (2002).

15 C. TralleroGiner, A. Debernardi, M. Cardona, E. MenendezProupin, and A. I. Ekimov, Physical Review B-Condensed Matter **57**, 4664 (1998).

16 J. Y. Zhang, X. Y. Wang, M. Xiao, L. Qu, and X. Peng, Applied Physics Letters **81**, 2076 (2002).

17 F. Cerdeira, C. J. Buchenauer, F. H. Pollak, and M. Cardona, Physical Review B **5**, 580 (1972).

18 The bulk LO phonon pressure coefficient was obtained using a bulk modulus value of 55 GPa, LO phonon frequency of 213.1 cm^{-1}, and a mode Gruneisen parameter of 1.1.

19 The phonon confinement term, CR^{-2}, was obtained from the calculated LO phonon dispersion with size in Fig. 2 (dashed line).

20 J. N. Wickham, A. B. Herhold, and A. P. Alivisatos, Physical Review Letters **84**, 923 (2000).

Chapter 6: Electron Momentum Distributions in Nanocrystal Quantum Dots Using Positrons

6.1. Introduction

Semiconductor nanocrystals, or quantum dots (QDs), are materials that experience electronic confinement in all three spatial dimensions. [1] As a result of this confinement, changes in the optical properties are seen as a function of particle size that are manifested in the observed scaling laws for QDs. Continued understanding of these scaling laws are needed for advances in QD physics, as well as advances in the fabrication of novel materials based on QD nanostructures.

Many experiments have been used to probe the electronic density in QDs in order to better understand the electronic properties of these materials as a function of particle size. Positron spectroscopy will be used to accomplish this task as it utilizes the properties of matter-antimatter annihilation to provide information on the electron momentum distribution in a sample. By tracking the Doppler broadening of the annihilated gamma ray photons, changes in the electronic structure of a quantum dot as a function of size can be explored. In this chapter, I detail some of the first work ever performed using positron spectroscopy to analyze the electronic properties of QD solids. It will be shown that positron spectroscopy is a useful tool to elucidate the mechanism of positron annihilation in solids. I will also show that the annihilation mechanism in a QD is highly dependent on the synthetic strategy employed to fabricate the QDs; this result was unexpected. Possible reasons for this behavior are discussed. Finally, novel experiments employing spin polarized positron spectroscopy is described for the first time. Possible results of anomalous magnetic effects at the nanoscale are observed. These results represent preliminary investigations into the application of positron spectroscopy to nanoscale materials and further studies are in order.

6.2. Background

In the study of elemental particles, all particles are primarily grouped into four families. These families are the leptons, mesons, baryons, and field quanta. These names originally are based on the Greek words for light, middle, and heavy, as the fundamental particle were originally classified into families based upon their mass: leptons for the light particles, mesons for the middle group, and baryons for the heavier particles. The positron (e^+) is the antiparticle of the electron (e^-), both of which are leptons. Leptons participate in gravitational, weak, and electromagnetic interactions. Unlike baryons, which include neutrons, leptons do not participate in the strong, or nuclear, force. The positron has the same mass (511 keV/c^2) and spin as the electron, but the opposite charge and magnetic moment (Fig. 6.1). The positron was first introduced in 1930 by P.A.M. Dirac to account for the occurrence of negative energy solutions to his relativistic quantum theory. [2] Dirac's postulate was experimentally verified in 1932 by C. Anderson in a cloud chamber. [3] Due to the fact that the positron is anti-matter, it possesses the ability to annihilate with an electron and give off radiation in the form of gamma rays,

$$\begin{array}{rcl} \mathrm{e^- + e^+ + M} & \rightarrow & \mathrm{n}\gamma + \mathrm{M} \\ L = (+1) + (-1) & \rightarrow & (0) \end{array} \qquad (6\text{-}1)$$

where *L* is the lepton number. High-energy physicists use lepton numbers to deduce why certain collisions create specific particles. If lepton number is not conserved, than the process cannot occur. The number of photons produced in the collision depends on the number of bodies involved in the collision. In most of our cases, we will deal with two-body collisions (i.e. a positron colliding with an electron), which satisfy all the energy conservation laws by themselves, including conservation of lepton number (eq 6-1), which is required for any process, therefore producing two γ photons per collision event.

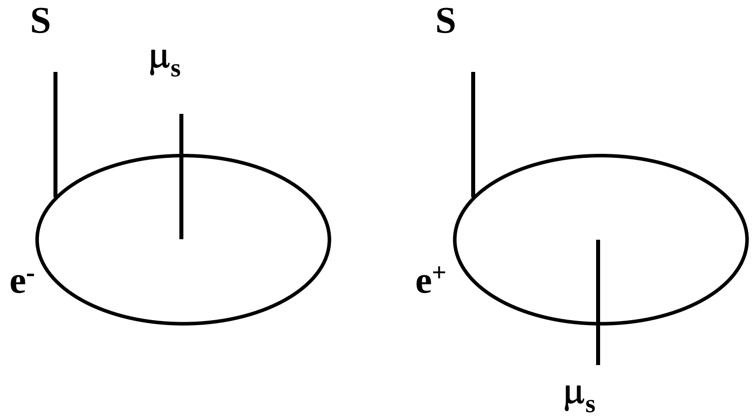

Figure 6.1. Relation between spin, *S*, and magnetic moment, μ_S, for an electron, e^-, and positron, e^+.

The use of the annihilation radiation generated from the collision process in eq. 6-1 as a quantitative tool for identifying the nature of atomic defects in materials is known as positron annihilation spectroscopy (PAS). Several observables in the PAS experiment include the positron lifetime, [4] two-dimensional angular correlation of annihilation radiation (2D-ACAR), [5] positronium (Ps) formation, [6] and Doppler broadening of annihilation radiation. [7] Each technique has its inherent benefits and detractions. Positron lifetime experiments are able to provide information as to the type of vacancy in a material, as well as defect concentrations; but are highly insensitive to the chemical nature of the defect. 2D-ACAR allows for the analysis of momentum distributions in a material, but intense theoretical descriptions are needed to analyze and interpret the data. Ps formation is a valuable tool to fully analyze the defective nature of surfaces, but is not sensitive to point defects. The

Doppler broadening experiment provides information on the momentum distribution in a material, but unlike 2D-ACAR, Doppler experiments are highly sensitive to the high momentum core electrons, which allows for a thorough analysis of the chemical nature of internal core defects. A more thorough explanation of the Doppler broadening experiment is provided in section 6.4.

6.3. Positron Interactions with Materials

6.3.1. Positron Trapping

As a positron enters a solid, it rapidly loses energy via many inelastic processes, e.g. ionization, plasmon excitations, electron-hole pair formation, phonon scattering, and relaxes to thermal (25 meV) energies. [8] This process is known as thermalization and occurs between 1-3 ps at 300 K. Even at cryogenic temperatures, positron thermalization kinetics are much faster than the positron lifetime, and therefore its contributions to the total lifetime negligible.

Transport of thermalized positrons is described by diffusion theory and can be written using the Nernst-Einstein relation and the relaxation-time approximation,

$$D_+ = \frac{\mu_+}{e} kT = \frac{kT}{m^*} \tau_{rel} \tag{6-2}$$

where D_+ is the positron diffusion coefficient, μ_+ is the mobility, k is the Boltzmann constant, T the temperature, e the fundamental unit of charge, m^* the positron effective mass, and τ_{rel} the relaxation time. The diffusion coefficient can be related to the diffusion length,

$$L_+ = (6D_+\tau)^{1/2} = \left(\frac{6kT\tau_{rel}}{m^*}\tau\right)^{1/2} \tag{6-3}$$

where τ is the positron lifetime. Typical diffusion lengths are 500 nm at 300 K. This means that the thermalized positron will travel ~500 nm in a solid before it annihilates. If the positron becomes trapped at a lattice point for a finite period of time, the effective diffusion length will be accordingly lowered. Therefore, the positron lifetime is very sensitive to the density of defects in a materials arising from vacancies, interstitial atoms, or lattice defects in materials.

As a result of the trapping, the positron lifetime will increase. The positron lifetime (τ) is given by the equation,

$$\tau = \pi\, r_o^2 c \int d\mathbf{r} \left|\Psi_+(\mathbf{r})\right|^2 n(\mathbf{r})\gamma\ [n(\mathbf{r})] \tag{6-4}$$

where r_o is the classical radius of the electron, c is the speed of light, $n(\mathbf{r})$ is the electron density, and $\gamma[n]$ is a correction factors that account for the change of electron density at the positron. [4] The positron wave function can be calculated from the one-particle Schrödinger equation and varies from a delocalized Bloch state in the "perfect" lattice, to a localized state at defect centers. The localized state can be a deep or shallow trap center, depending on the type of defect present. For a deep trap, e.g. a vacancy defect which has missing electron density, the positron ground state binding energy is on the order of 1 eV, therefore eliminating the chances for a thermally stimulated detrapping process. A shallow trap can be a negative ion where Coulombic forces trap the positron into a Rydberg-like state with binding energies between 10-100 meV. Detrapping from this state follows an exponential relation,

$$\delta = \mu_{Ry}\left(\frac{2\pi\, m^{*} kT}{h^{2}}\right)^{3/2} \exp\left(-\frac{E_{b,Ry}}{kT}\right) \tag{6-5}$$

and is extremely sensitive to the negative ion concentration in the material.

6.3.2. Positronium formation

A possible "reaction" that can occur upon the implantation of a positron into a material is the formation of positronium (Ps),

$$e^{-} + e^{+} \rightarrow \mathrm{Ps} \tag{6-6}$$

which represents the bound state of an electron and positron (e^{-}/e^{+}). Ps exhibits two spin states (Figure 6.2) called “para” (*p*-Ps) and “ortho” (*o*-Ps) for singlet and triplet, respectively.[6] Typical lifetimes for para-Ps (*p*-Ps; antiparallel spins) and ortho-Ps (*o*-Ps; parallel spins) are 125 ps and 0.5-5 ns,

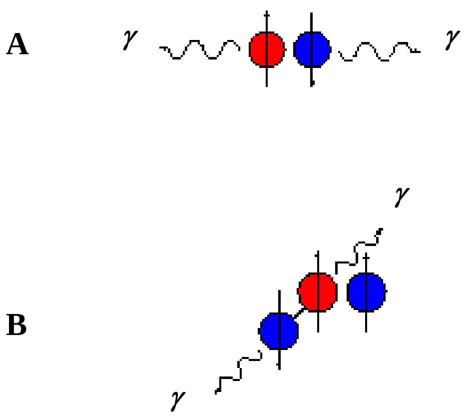

Figure 6.2. Illustration of (A) para and (B) ortho Positronium.

respectively. It has been shown that o-Ps lifetimes can decrease due to chemical interactions.

The selection rules for self-annihilation relates the orbital angular momentum *l* of the Ps state, the spin angular momentum *s* (0 for *p*-Ps, 1 for *o*-Ps), and the number of photons *i*,

$$(-1)^{l+s} = (-1)^{i} \tag{6-7}$$

According to this selection rule, in vacuum for $l = 0$ (ground state), *p*-Ps annihilates into an even number (two) of photons and *o*-Ps annihilates into an odd number (three) of photons. When *o*-Ps forms in matter, however, the annihilation selection rules can be violated in exchange for spin-conservation. The positron wave function can overlap with electrons outside the Ps bound state. Annihilations can occur with these electrons as long as they have antiparallel spin. This is known as “pick-off” annihilation and it can decrease the *o*-Ps lifetime by about two orders of magnitude. [4]

6.4. Experimental Technique

The experiments performed in this dissertation were done on a two-detector coincidence Doppler broadening positron annihilation spectrometer (DOBS) at the Lawrence Livermore National Laboratory under Dr. P. Asoka-Kumar. [7] DOBS is a momentum distribution technique. Due to mass-energy conservation laws, the two-photon annihilation event (which is most probable) produces two gamma rays each with rest energy of m_oc^2 (511 keV). An additional energy term arises from the kinetic energy of the particles themselves, [9]

$$(m_o c^2 + K^+) + (m_o c^2 + K^-) = E_1 \tag{6-8}$$

where K^+ and K^- are the kinetic energies of the positron and electron, respectively. If K^+ and K^- are negligible then, [9] due to conservation laws, E_1 must equal $2m_oc^2$ (1022 keV). If K^+ and K^- are not negligible, the electron-positron pair transfers its momentum to the γ-rays, which in turn have photon energy spreads different in the laboratory frame, when compared to their center of mass frame (Fig. 6.3) given by eq. 6-5,

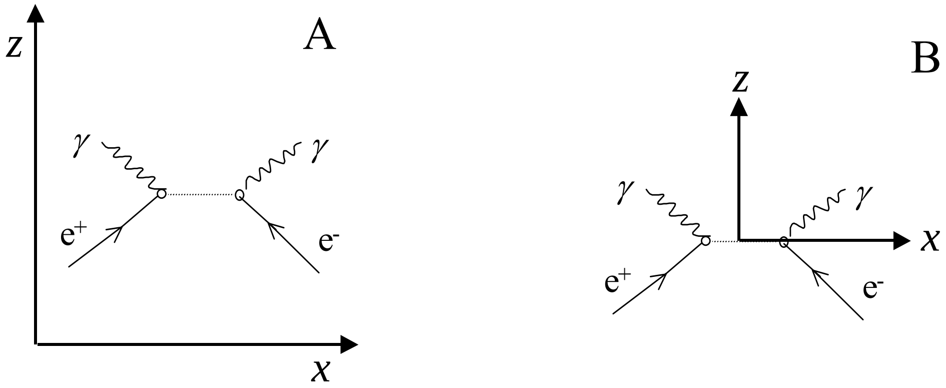

Figure 6.3. Fenyman diagrams for two-photon positron-electron annihilation in the laboratory and center of mass frames.

$$\Delta \mathrm{E} = \frac{-\,\mathrm{E_b}}{2} \pm \frac{pc}{2} \qquad (6\text{-}9)$$

where $\mathrm{E_b}$ is the effective electronic binding energy to the solid and p is the pair momentum. If we multiply by c and use the relation $p = \mathrm{mv}$, then

$$\Delta \mathrm{E} = \frac{-\,\mathrm{E_b}}{2} \pm \mathrm{m_o}c^2 \times \frac{\mathrm{v}}{2c} \qquad (6\text{-}10)$$

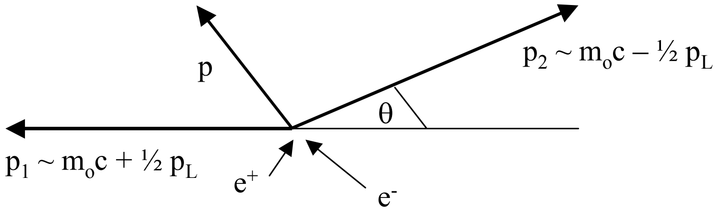

Figure 6.4. Angular correlation coordinates for e^+/e^- annihilation. The momentum vectors shown are projections onto the plane of the paper.

In other words, the energy broadening term is dominated by the resultant velocity transferred to the photons from the electron-positron pair momentum. For instance, a low energy electron (1 eV), i.e. an electron with a large de Broglie wavelength, has a velocity of ~588 m s^{-1} and a resultant Doppler shift of ~0.5 keV (~0.27 a.u; Table 6.1), which is a noticeable shift (see Appendix 6.1 for more detail). In general, only the positron momentum, K^+, is considered negligible, so the observed energy broadening is a direct function of the kinetic energy of the electrons. In other words, the energy broadening will be a function of the momentum distribution of the e^-. The energy broadening is usually minimal, so momentum conservation laws require that photons with equal energies (m_oc^2) must move in exactly opposite directions (Figure 6.4). [8] Deviation from this co-linearity can be measured with the high precision position technique, 2D-ACAR, described above. This technique complements the DOBS measurement extremely well.

The experimental setup of two-detector coincidence DOBS is illustrated in Figure 6.5a with a picture of the actual set-up housed in the

Table 6.1. Conversion units between energy and momentum

	keV	a.u.	**mc**
1 keV	1	0.54	3.91×10^{-3}
1 a.u.	1.85	1	7.20×10^{-3}
***1* mc**	255.75	138.89	1

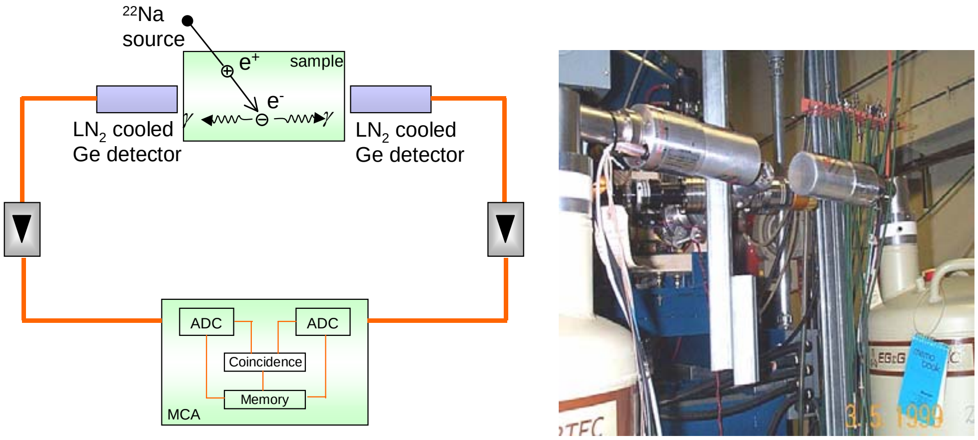

Figure 6.5. Schematic illustration (left) and picture (right) of the coincidence two detector DOBS experiment at LLNL.

Department of Physics at the Lawrence Livermore National Laboratory shown in Figure 6.5b. [7] Polyenergetic positrons are produced from a Pb-shielded

^{22}Na source. The positron energies span nearly five orders of magnitude and it

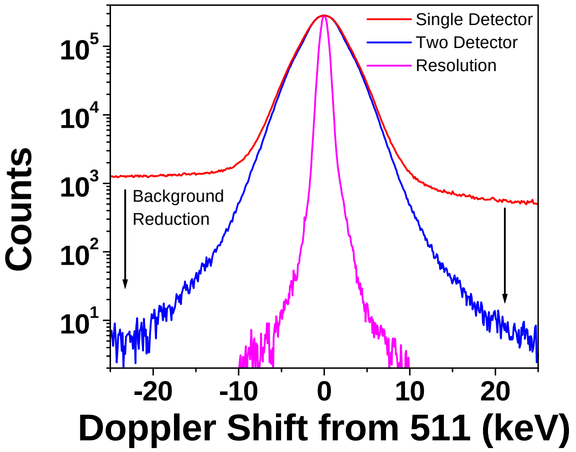

Figure 6.6. Increase in signal to noise ratio with addition of two detectors in coincidence.

is therefore necessary to use thick samples when performing the experiment. The positron implantation depth, *x*, into a sample is given by eq. 6-11,

$$x\,(\mathrm{nm}) = (40/\rho)E^{1.6}\ (\mathrm{keV}) \qquad (6\text{-}11)$$

where E is the energy of the positron beam and ρ is the density of the sample. [11] Using $\rho_{\mathrm{CdSe}} = 7.0$ g cm^{-2} and $E \sim 200$ keV, we see that $x \sim 27454$ nm (~27.5 μm). This means that a sample must be tens of microns thick in order to insure the positron will annihilate in the sample, instead of somewhere else. The energies of both of the annihilation photons are collected by a cross correlation technique where the annihilation photons are simultaneously detected by two high efficiency liquid-nitrogen cooled pure Ge detectors. The use of two detectors rather than one raises the signal-to-noise ratio from about 1000 to 10^6

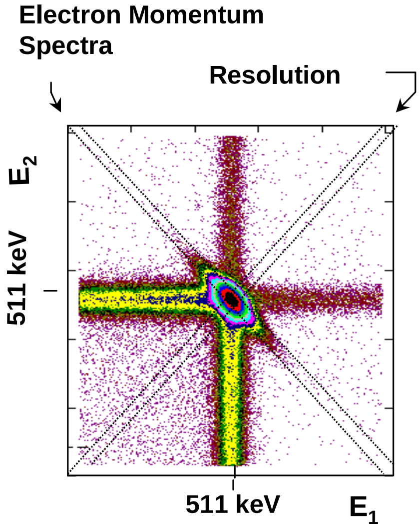

Figure 6.7. Two-dimensional array of γ -ray photon spectra.

(Figure 6.6). The annihilation photons are subjected to a large potential (several kV) and converted into an electrical pulse by a preamplifier. The amplitude of the pulse is a function of the photon energy. A multi-channel analyzer along with a peak-stabilizing system allows the long-term collection of several million counts.

With the Ge detectors set in coincidence, the resultant γ-ray spectra are a two-dimensional array of the detector counting rates (Figure 6.7). With the coincidence arrangement, the intensity profile of the diagonal from the upper left to lower right of the 2-d array is the coincidence Doppler spectra. The increase of the annihilation γ-ray energy in one detector leads to the reduction of the γ-ray energy in the second detector, in accordance with momentum conservation laws ($\Sigma E = 2m_ec^2 \sim 1022$ keV).

Coincidence DOBS measurements were done on either thin films or pellets of CdSe, Au, and Co nanocrystals. The CdSe QDs were synthesized using known high temperature colloidal methods [10] and are coated with the organic ligands of trioctylphosphine oxide (TOPO) and/or phosphonic acid. The samples were dissolved in hexanes and allowed to slowly evaporate on a bulk Si wafer. Results were obtained on QD sizes of 60, 55, and 45 Å diameter and a size dispersity of ~5%. Unfortunately, sample sizes smaller than 45 Å showed background annihilation contamination from the Si substrate, indicating that the samples were too thin to be probed with an unmoderated position beam. With our smallest sized samples, the films were too thin to allow for efficient annihilation in the CdSe and this resulted in annihilation in the Si substrate.

For the Au and Co metal nanocrystals, samples were prepared using known literature methods. [12, 13] The samples were prepared by pressing pure pellets of the materials. Some care was taken to minimize the exposure of the Co NPs to the atmosphere, as they are very oxygen sensitive. The pellets were mounted directly in the cryostat in the positron spectrometer to minimize the chances of background annihilation contamination. The experimental details of the positron experiments involving these nanoparticles are exactly as described above, except for the introduction of an applied magnetic field. The applied field was oriented “up” or “down” with respect to the laboratory *z*-axis, and was ~1 T (10 kOe).

6.5. Results and Discussion

6.5.1. CdSe Quantum Dots

For QDs, the size dependent optical band gap, which is observed to have a blue shift as the particle size is reduced, is a direct function of the “widening” of the lowest energy electronic transition. In CdSe, this is formally a spin allowed $1S_{1/2}$ (hole levels) → $1S_e$ (electron levels) transition. Many techniques have been used to probe this effect including optical absorption, [14] x-ray, [15] and electrochemical methods. [16] Positron spectroscopy is a useful technique to probe the size depndent shift in the optical band gap for QDs as is it an electron momentum distribution technique; therefore, electron energy can be derived from the observed momentum. It is also advantageous as it simplifies the interaction physics by excluding electron-electron correlation effects.

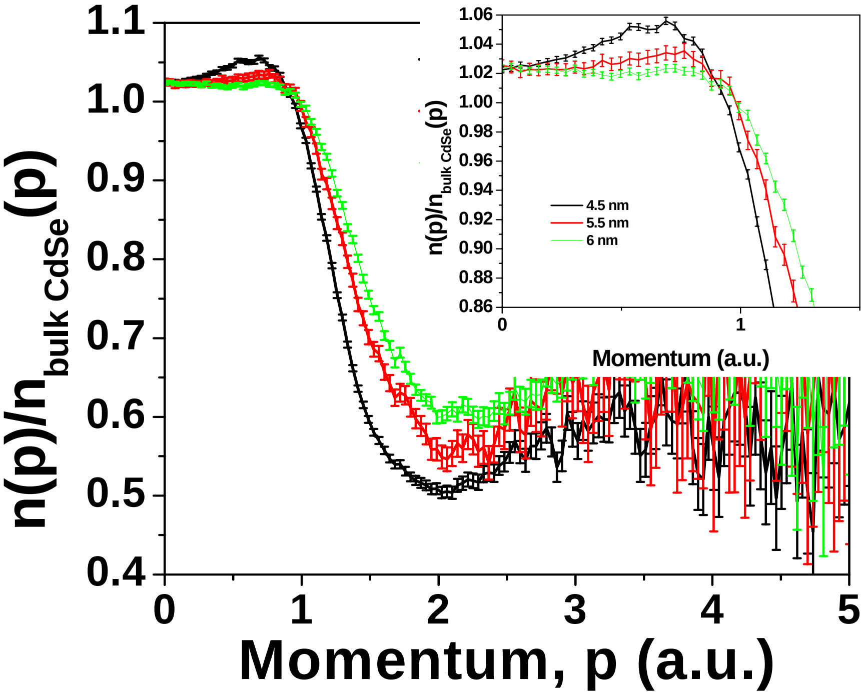

Figure 6.8. OEMS spectra of 45, 55 and 60 Å diameter CdSe QDs.

Figure 6.8 shows the orbital electron momentum spectra (OEMS) for a series of CdSe QDs. The sizes range from 45-60 Å in diameter. As stated above, background contamination was seen for samples sizes smaller than 45 Å. In Fig. 6.8, the OEMS show only a small change with particle size, which is in contradiction of quantum confinement (QC) effects. Due to QC, we would expect a size dependent OEMS due to an opening up of states at the Fermi momentum. To verify whether this was indicative of the physics of the system or simply an experimental artifact, we had independent OEMS measurements done on these samples by K.G. Lynn's group at Washington

State University. Prof. Lynn's positron beam is moderated (i.e. energy selective), therefore positron implantation profiles were enabled to allow 100% annihilation in the QD layer. From the results at WSU and our results from LLNL, we can conclude that no significant change in the OEMS is seen with size. This is in contradiction with recent positron annihilation results on lyothermally grown colloidal CdSe QDs collected at WSU [17] and verified at LLNL

To begin to understand the difference in positron physics between the two colloidal preparations, the OEMS was examined on lyothermally grown CdSe. Figure 6.9 shows the OEMS for ~55 Å CdSe prepared via the CdO precursor method [10] versus ~40 Å CdSe prepared via the high temperature organometallic injection method. [18] As can be seen from Fig. 6.9, there are obvious differences between the OEMS of the two QDs. Furthermore, the magnitude of the shifts is probably not due to size differences as the difference in momentum of the two sizes according to Ref. 17 should be ~0.02-0.04 a.u., while the shift seen in Fig. 6.9 is nearly 0.3-0.4 a.u. In the following, I will briefly describe some of the physics involved that could contribute to this differing behavior. Further studies, however, are needed to fully understand the observations.

There are essentially three annihilation models for positron-QD interactions. I will refer to these three models as core, surface, and passivant

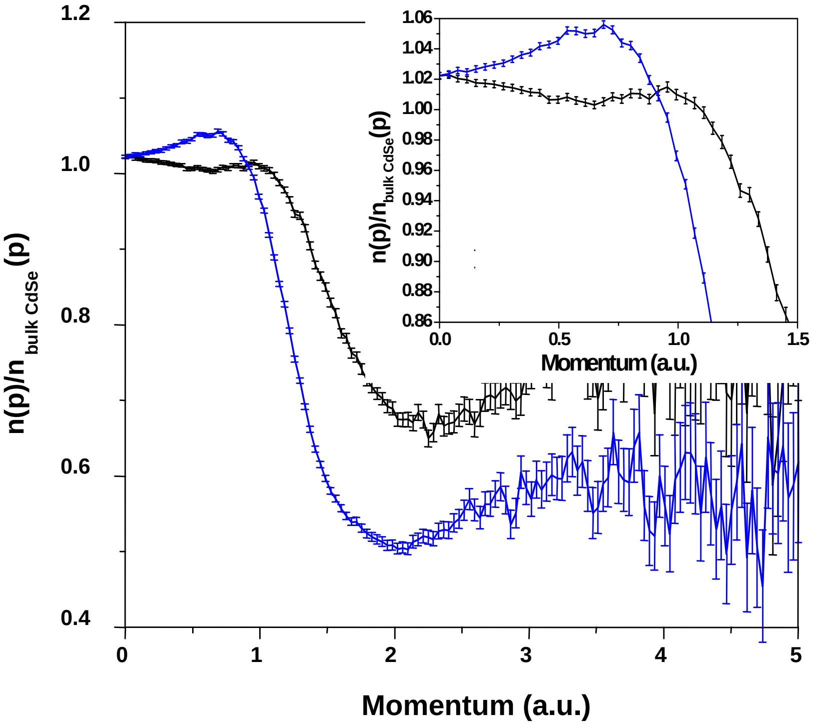

Figure 6.9. Comparison OEMS spectra of CdSe QDs prepared by Ref 10 (blue) and Ref. 18 (black).

annihilation (Figure 6.10). I will explain the differences between the three models, and offer suggestions as to the annihilation model of a positron in a CdSe QD. The first model (Fig. 6.10a), core annihilation, represents positron annihilation with the valence electrons of the QD (i.e. the electrons that contribute to the QC effects). The term "core" is used to be consistent with literature nomenclature as "core properties" are typically related to properties of the QD not associated with the surface atoms. The second model (Fig. 6.10b), passivant annihilation, represents positron annihilation with the organic ligands that coat the surface of the quantum dot. The third model (Fig. 6.10c), surface annihilation, represents positron annihilation with a surface (or defect) atom of the system.

From the data presented in Fig. 6.8, it can be stated that the annihilation model does not fit within the core annihilation model, as the OEMS does not change significantly with dot size. This implies that the physics involved in the QD-positron interaction do not entail effects from quantum confinement. The other annihilation models involve passivant and surface annihilation. As of this time, the current data analysis cannot sufficiently describe which of the two models are responsible for the experimental results. What can be said is that positron localization on CdSe QDs prepared via Ref. 10 changes very little as a function of dot size and implies that annihilation could be occurring at a defect site. Whether the defect site is a surface atom or a passivant molecule is still under investigation.

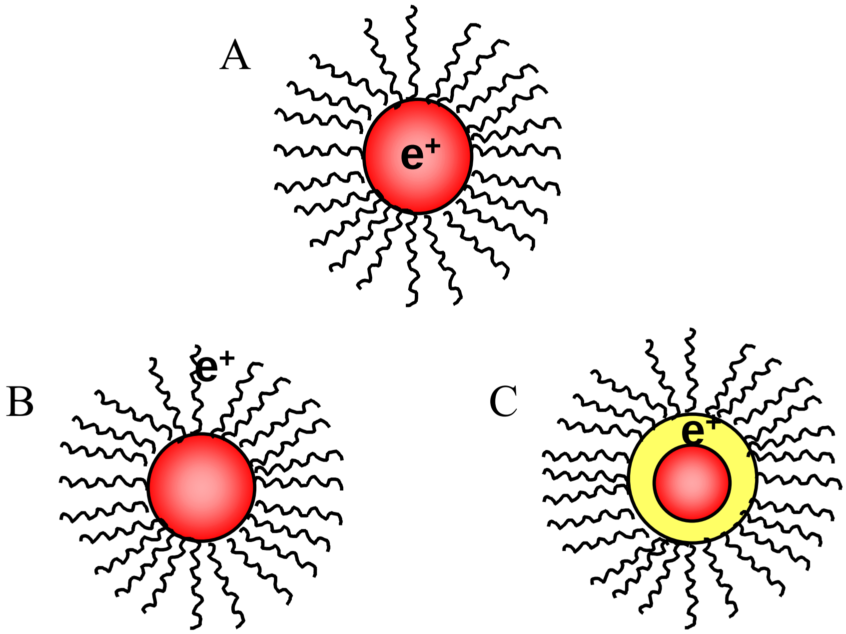

Figure 6.10. Illustration of (A) core, (B) passivant, and (C) surface annihilation.

Positron annihilation in the CdSe QDs prepared via Ref. 18 is more straightforward to analyze. As seen in Figure 6.9 and Ref. 17, size dependent shifts in the peak centroid of the OEMS is seen for the CdSe QDs, indicative of opening of the band gap at the Fermi momentum and can be assigned to core annihilation. The authors in Ref. 17 have supported this model with theoretical calculations. According to their calculations, core annihilation almost exclusively expected due to the lack of positron wave function leakage. Because nearly 80% of the positron wave function is confined to the interior of the sphere, the probability for positron localization on the exterior (i.e. surface or coating) of the QD is minimal. Also, their calculations show that the positron work function, ϕ^+, for CdSe is –9.0 eV, implying that the positron cannot escape to the vacuum after implantation into CdSe, lowering the probability for exterior annihilation. Finally, the authors noted that the peak arising in the OEMS spectra assigned to the widening of the band gap cannot be due to passivant annihilation, as annihilation with a phosphorous atoms would occur at ~1.32 a.u., which is not experimentally observed. The problem with this argument, however, is that the OEMS is highly dependent on the normalization of the data set. [19] Therefore, the observed peaks can vary in momentum space depending on the spectra it is normalized to. In addition to the QEMS spectra, the authors ran positron lifetime measurements on a 60 Å CdSe QD. Due to the similar values between bulk CdSe lifetimes (275 ps) and 60 Å CdSe QD lifetime (251 ps), the authors concluded the QD samples were essentially defect free. However, the two values differ by nearly 10%, indicating that the positron trapping mechanisms may differ in nanoscale CdSe. To quantify this data, temporal traces should be shown, along with fitting parameters, and χ^2 merit values. This data, along with a thorough size dependent analysis can identify the how the positron lifetime changes as a function of the QD size.

6.5.2. Au and Co Nanoparticles

Due to parity non-conservation in beta decay, positrons emitted from the radioactive ^{22}Na source have their spin-aligned parallel to momentum. Assuming only two-body processes, the electron-positron annihilation occurs only when the two particle spins are aligned anti-parallel, therefore polarization dependencies on the annihilation process can be observed by changing the polarization of the electrons in the sample. For instance, studies on Fe-Cu alloys have shown that annihilation occurs in the Cu nano-precipitates, due to the non-magnetic character of elemental Cu which correlated to the lack of magnetic behavior in the orbital electron momentum spectra. [20] The magnetic dependent positron measurements are governed by the polarization ratio (PR) given by,

$$\mathrm{PR} = \frac{n_{\uparrow} - n_{\downarrow}}{n_{\uparrow} + n_{\downarrow}} \tag{6-12}$$

where $n_{\uparrow}$ and $n_{\downarrow}$ refer to the annihilation fraction with positron polarization parallel and anti-parallel to the applied external magnetic field, respectively. [20] As the magnetic field is applied, electrons in the sample may be polarized (i.e. change their orientation) and these electrons will undergo preferential annihilation with the polarized positron beam (Figure 6.11). It is obvious from Fig. 6.11, that if a sample is diamagnetic or antiferromagnetic, the PR should be zero, as there is no preferential polarization of the sample electrons. However, a ferromagnetic sample should show a non-zero PR, because the electrons are strongly polarized in the applied field. The PR for the Co and Au nanoparticles are seen in Figures 6.12 and 6.13, respectively. The observed spectra show anomalous dependencies. The PR for 130 Å Co NCs in Fig 6.12 show no observable polarization dependence. Because Co NCs have been shown to be ferromagnets [12] this behavior was unexpected. Recent experiments in our lab, however, have suggested that the actual particles formed in the synthesis were in fact CoO, and not Co, due to solvent impurities and are consistent with annihilation with AFM CoO. Because CoO is antiferromagnetic, we would expect to seen no polarization dependence on the orbital electron momentum spectra (vide supra).

In Figure 6.13, a slight dependence in the PR is seen for diamagnetic 15 Å Au nanoparticles, which is a surprising result. The small dependence of the

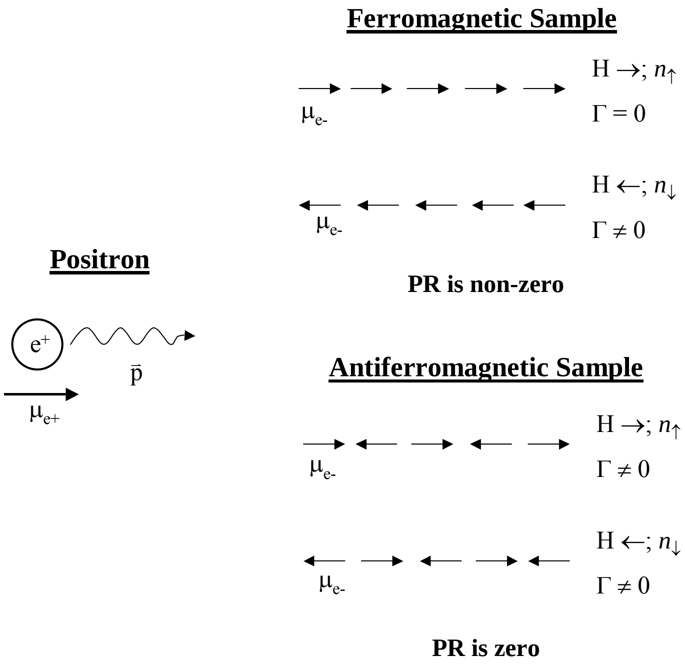

Figure 6.11. Illustration of annihilation of a polarized positron with ferro- and antiferromagnetic samples.

Au NCs is more perplexing, but maybe a result of the surface electrons. As the size of Au gets close to the mean free electron path, the surface electrons can be photoexcited in what is called the surface plasmon resonance, which undergoes damping with decreasing size. These surface electrons are polarizable, so it may be possible to polarize these electrons and see a PR due to this effect. More experiments are needed, however, to quantify the nature of these results.

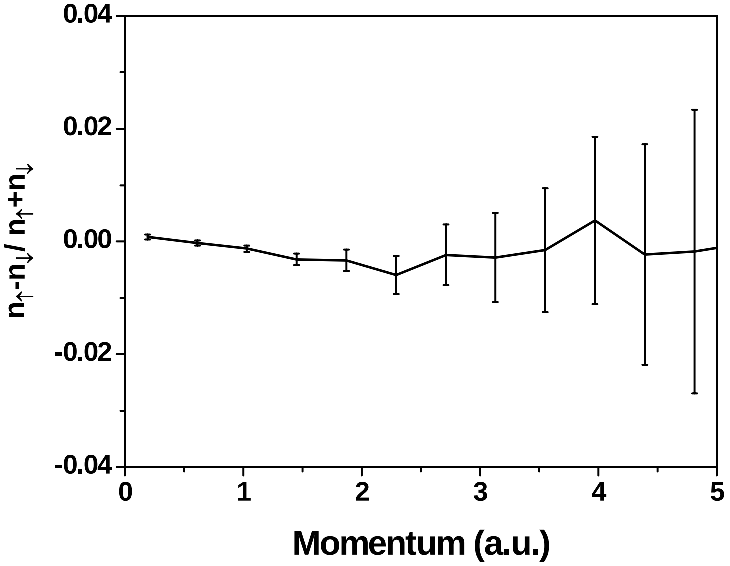

Figure 6.12. PR for 130 Å Co nanoparticle.

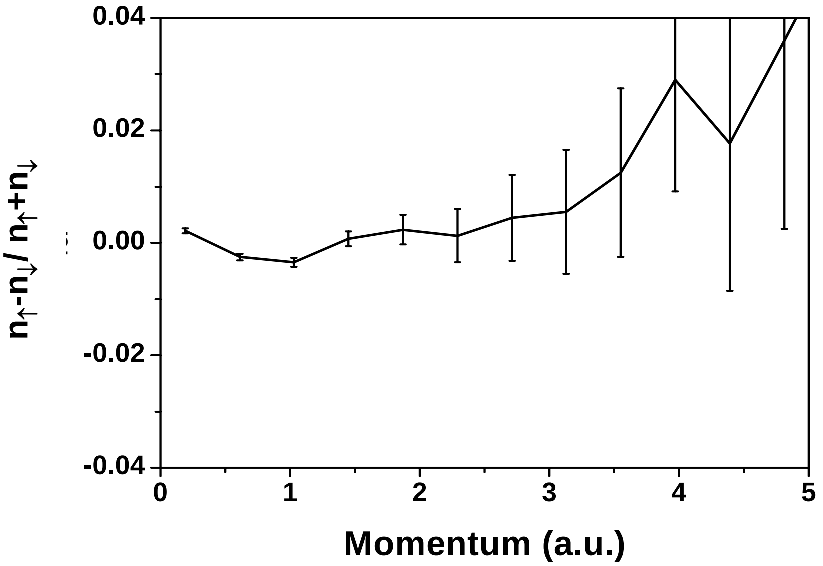

Figure 6.13. PR for 15 Å Au nanoparticle.

APPENDIX 6.1. *Derivation of the relation between energy and momentum.*

Consider an electron with energy of 1 keV (1000 eV). Using the de Broglie relation,

$$\lambda = \frac{h}{p} \tag{A6-1}$$

and multiplying by *c* and using the relationship *p* = *mv*, eq. A6-1 becomes,

$$\lambda = \frac{hc}{mvc} \qquad \text{(A6-2).}$$

Solving for *v* and multiplying by *c* gives the relation,

$$v = \frac{hc}{mc^2} * \frac{c}{\lambda} \qquad \text{(A6-3).}$$

Using the values hc = 1240 eV nm and mc^2 = 511 × 10^3 eV, eq. A6-3 reduces to

$$v = \frac{2.43 \times 10^{-3}\,(\text{nm})}{\lambda\,(\text{nm})} * c \qquad \text{(A6-4).}$$

Therefore, using eq. A6-4, the velocity of a 1 keV electron is $1.96 \times 10^{-3} c$ or 5.9×10^5 m s^{-1}. The momentum of this electron is calculated from the equation,

$$pc = \frac{mcv}{\sqrt{1-\frac{v^2}{c^2}}} = mc^2 * \frac{(\frac{v}{c})}{\sqrt{1-\frac{v^2}{c^2}}} \qquad \text{(A6-5).}$$

The momentum calculated from Eq. A6-5 can be expressed in units of eV c^{-1} or mc. The momentum values for a 1 keV electron are 1 keV/c or 1.96×10^{-3} mc. Because the Doppler broadening relationship between energy and momentum is, $pc = 2\Delta E$, the momentum of a 1 keV electron is actually 3.91×10^{-3} mc. The units used by most positron physicists, however, are atomic momentum units (a.u.) with the conversion factor being 1 a.u. ~ 7.20×10^{-3} mc. Therefore, a 1 keV electron would have a resultant Doppler shift of ~0.54 a.u.

6.6. References

1 A. P. Alivisatos, Journal of Physical Chemistry 100, 13226 (1996).

2 P. A. M. Dirac, *The Principles of Quantum Mechanics* (Oxford University Press, Oxford, 1935).

3 C. D. Anderson, Physical Review 43, 491 (1933).

4 R. Krause-Rehberg and H. S. Leipner, *Positron annihilation in semiconductors : defect studies* (Springer, Berlin ; New York, 1999).

5 J. P. Peng, K. G. Lynn, P. Asokakumar, D. P. Becker, and D. R. Harshman, Physical Review Letters 76, 2157 (1996).

6 D. M. Schrader and Y. C. Jean, *Positron and positronium chemistry* (Elsevier, Amsterdam The Netherlands ; New York, 1988).

7 P. Asokakumar, M. Alatalo, V. J. Ghosh, A. C. Kruseman, B. Nielsen, and K. G. Lynn, Physical Review Letters 77, 2097 (1996).

8 P. Hautojärvi and A. Vehanen, *Positrons in Solids* (Springer-Verlag, Berlin, 1979).

9 K. S. Krane, *Modern physics* (Wiley, New York, 1996).

10 Z. A. Peng and X. G. Peng, Journal of the American Chemical Society 123, 183 (2001).

11 M. P. Petkov, K. G. Lynn, and A. van Veen, Physical Review B 6604, U531 (2002).

12 S. H. Sun and C. B. Murray, Journal of Applied Physics 85, 4325 (1999).

13 S. L. Cumberland and G. F. Strouse, Langmuir 18, 269 (2002).

14 D. J. Norris and M. G. Bawendi, Physical Review B-Condensed Matter 53, 16338 (1996).

15 T. vanBuuren, L. N. Dinh, L. L. Chase, W. J. Siekhaus, and L. J. Terminello, Physical Review Letters 80, 3803 (1998).

16 S. K. Haram, B. M. Quinn, and A. J. Bard, Journal of the American Chemical Society 123, 8860 (2001).

17 M. H. Weber, K. G. Lynn, B. Barbiellini, P. A. Sterne, and A. B. Denison, Physical Review B 6604, U50 (2002).

18 C. B. Murray, D. J. Norris, and M. G. Bawendi, Journal of the American Chemical Society 115, 8706 (1993).

19 P. Asoka-Kumar, private communication .

20 P. Askoa-Kumar, B. D. Wirth, P. A. Sterne, G. R. Odette, and R. H. Howell, submitted (2001).